Investigation of Particle Deposition in Internal Cooling Cavities of a Nozzle Guide Vane

DISSERTATION

Presented in Partial Fulfillment of the Requirements for the Degree Doctor of Philosophy
In the Graduate School of The Ohio State University

By

Brian Patrick Casaday

Graduate Program in Aeronautical and Astronautical Engineering

The Ohio State University

2013

Dissertation Committee:

Dr. Jeffrey P. Bons, Advisor

Dr. Ali Ameri

Dr. Michael Dunn

Dr. Datta Gaitonde

Dr. Sandip Mazumder

Abstract

Experimental and computational studies were conducted regarding particle deposition in the internal film cooling cavities of nozzle guide vanes. An experimental facility was fabricated to simulate particle deposition on an impingement liner and upstream surface of a nozzle guide vane wall. The facility supplied particle-laden flow at temperatures up to 1000°F (540°C) to a simplified impingement cooling test section. The heated flow passed through a perforated impingement plate and impacted on a heated flat wall. The particle-laden impingement jets resulted in the buildup of deposit cones associated with individual impingement jets. The deposit growth rate increased with increasing temperature and decreasing impinging velocities. For some low flow rates or high flow temperatures, the deposit cones heights spanned the entire gap between the impingement plate and wall, and grew through the impingement holes. For high flow rates, deposit structures were removed by shear forces from the flow. At low temperatures, deposit formed not only as individual cones, but as ridges located at the mid-planes between impinging jets.

A computational model was developed to predict the deposit buildup seen in the experiments. The test section geometry and fluid flow from the experiment were replicated computationally and an Eulerian-Lagrangian particle tracking technique was employed. Several particle sticking models were employed and tested for

adequacy. Sticking models that accurately predicted locations and rates in external deposition experiments failed to predict certain structures or rates seen in internal applications. A geometry adaptation technique was employed and the effect on deposition prediction was discussed.

A new computational sticking model was developed that predicts deposition rates based on the local wall shear. The growth patterns were compared to experiments under different operating conditions. Of all the sticking models employed, the model based on wall shear, in conjunction with geometry adaptation, proved to be the most accurate in predicting the forms of deposit growth. It was the only model that predicted the changing deposition trends based on flow temperature or Reynolds number, and is recommended for further investigation and application in the modeling of deposition in internal cooling cavities.

Dedicated to my lovely wife Amy and beautiful daughter Elise

Acknowledgements

I'd like to personally thank and acknowledge my advisor Dr. Jeffrey Bons, who has been enormously helpful throughout my graduate experience, both professionally and as a personal example. His instruction and experience have been invaluable. I'd like to thank my advisor Dr. Ali Ameri as well for his tireless efforts and advice.

I'd also like to thank the several individuals that have been part of the deposition research lab, as academic accomplishments are rarely achieved alone. I'd also like to acknowledge the Department of Energy and General Electric for funding contributions during the course of this research.

Ultimately, I thank my Father in Heaven and my family for their continued love and support.

Vita

2008……B.S. Mechanical Engineering, Brigham Young University
2010……M.S. Mechanical Engineering, Brigham Young University

Publications

Webb, J., Casaday, B., Barker, B., Bons, J.P., Gledhill, A., Padture, N., "Coal Ash Deposition on Nozzle Guide Vanes: Part I—Experimental Characteristics of Four Coal Ash Types" *J. Turbomachinery,* 135, 021033 (2013)

Barker, B., Casaday, B., Shankara, P., Ameri, A., Bons, J.P., "Coal Ash Deposition on Nozzle Guide Vanes: Part II—Computational Modeling" *J. Turbomachinery,* 135, 011015 (2013)

Bonilla, C., Webb, J., Clum, C., Casaday, B., Brewer, E., and Bons, J.P., "The Effect of Particle Size and Film Cooling on Nozzle Guide Vane Deposition," *J. Eng. Gas Turbine Power*, 134, 101901 (2012)

Casaday, B., Ameri, A., Bons, J.P., "Numerical Investigation of Ash Deposition on Nozzle Guide Vane Endwalls" *J. Eng. Gas Turbine Power*, 135, 032001, (2013)

Casaday, B., and Vanderhoff, J.C. "Investigation of High-Frequency Internal Wave Interactions with an Enveloped Inertia Wave" *International Journal of Geophysics* 2012, 863792 (2012)

Fields of Study

Major Field: Aeronautical and Astronautical Engineering
Specialization: Computational Fluid Dynamics and Heat Transfer

Table of Contents

List of Tables

List of Figures

Nomenclature

a	=	Acceleration
A	=	Area
A_{cv}	=	Constant value in critical viscosity sticking model
B_{cv}	=	Constant value in critical viscosity sticking model
C_1	=	Uniformly distributed random number
C_C	=	Cunningham correction coefficient
C_D	=	Drag coefficient
C_J	=	Particle flux constant
$C\tau$	=	Shear-based sticking model slope constant
d	=	Diameter
e	=	Coefficient of restitution
E	=	Young's modulus
F_D	=	Force on particle due to drag
F_{Dc}	=	Modified drag force accounting for Cunningham correction
F_{SL}	=	Force on particle due to Saffman lift
F_{Therm}	=	Force on particle due to Thermophoresis
J	=	Particle flux
k	=	Thermal conductivity
k_e	=	Turbulent kinetic energy
k_1	=	Critical velocity model constant
k_2	=	Critical velocity model constant
KE	=	Kinetic energy
Kn	=	Knudsen number
k_L	=	Loss coefficient
l_c	=	Characteristic length scale
m	=	Mass
$\dot{m}$	=	Mass flow rate
P	=	Pressure
P_{amb}	=	Ambient pressure
P_{stick}	=	Sticking probability
Pr	=	Prandtl number
r	=	Radial position
Re	=	Reynolds number
s	=	Impingement hole spacing
St_k	=	Stokes number
T	=	Temperature
T_c	=	Coolant Temperature
V	=	Velocity

V_{rel}	=	Relative velocity between particle and fluid
t	=	Time
x	=	position in x-direction
y	=	position in y-direction
z	=	position in z-direction
α	=	Particle impact angle
β	=	Sticking probability
ε	=	Turbulent dissipation
σ	=	Standard deviation
σ_e	=	Standard deviation of coefficient of restitution
μ	=	Dynamic viscosity
λ	=	Mean free path of gas
ρ	=	Density
τ	=	Wall shear stress
τ_{min}	=	Lower wall shear limit for particle sticking
τ_{maz}	=	Upper wall shear limit for particle sticking
τ_{ε}	=	Time scale for discrete random walk
ν	=	Poisson ratio

Subscripts

$crit$	=	Critical value
f	=	Relating to fluid
h	=	Relating to impingement hole
N	=	Relating to normal direction
p	=	Relating to particle
T	=	Relating to tangential direction
W	=	Relating to wall

Chapter 1. Background

Particle ingestion can degrade and shorten the life of gas turbine engine components both in aircraft and land-based engines. It is, however, becoming increasingly necessary to operate turbine engines in environments in which they are more susceptible to the ingestion of foreign particles. Examples include aircraft operating in the vicinity of dust or volcanic ash clouds, taking off or landing on dirty runways (see Figure 1.1), and the operation of coal power plants which may introduce fly ash into the hot sections of the turbine. Particle ingestion has occasionally caused significant erosion damage to compressor components and deposition to the hot sections of turbine engines [1] (see Figure 1.1).

Figure 1.1 – (left) Dust ingestion into C-17 aircraft and (right) volcanic ash deposition on turbine vanes [2]

Dunn [1] described several instances of aircraft encounters with volcanic ash clouds, and the consequential damage to the turbine engine. An aircraft in an ash cloud

for only three or four minutes from Mt. St. Helens in 1980 lost power to two of its four engines. In 1982, a Boeing 747 lost power to all four engines after flying through the ash cloud from Mt. Galgunggung for seven minutes. In this case, the flight crew was not even aware that the volcano had erupted or that they were flying within the cloud. The volcanic ash caused severe damage to engine components, including large amounts of molten ash deposition on the first stage of the turbine (Figure 1.1). Several similar encounters occurred with other volcanic eruptions, but fortunately in all cases, partial power was able to be restored to the engines allowing for emergency landings without any loss of life. More recently, the eruption of the Icelandic volcano Eyjafjallajokull closed large regions of airspace for weeks. One result of this event was renewed interest in deposition research to determine the causes of deposition and how it affects turbine engines.

1.1 Experimental Deposition Research

Volcanic ash ingestion was recreated in a laboratory environment to investigate the mechanisms of damage and factors that lead to deposition in the hot sections of the turbine, as described by Kim et al. [3]. Full-scale engines were operated while particulate-laden flow was ingested at the inlet. The particulate-laden flow passed through the compressor, combustor, turbine, and bypass sections of the engines and performance was monitored. Tests were conducted with various particulate compositions, similar to those associated with the volcanic ash cloud encounters. The internal components of the engines were inspected after each test. Dunn and Kim et al. showed that three damage mechanisms to turbine engines with ingested volcanic ash are, in order of general importance, deposition of particulate matter on the hot sections of the turbine

engine, irreversible erosion of compressor components, and carbon deposits on the fuel nozzles. It was found that deposition rates were dependent on factors such as particle concentration, chemical composition, and temperature of both the flow and vane surfaces. The ingested particulate matter was analyzed for size distributions prior to testing, and samples were collected from the ECS (Environmental Control System) ducts at the latter compressor stages. It was determined that particles passing through the compressor are broken up into smaller particles, exiting the compressor with diameters typically below 10 μm.

There have been many studies looking into the causes and effects of deposition on turbine hardware, as discussed in a review of modern research by Hamed et al. [4]. This summarizes several studies focused on predicting particle trajectories, impact and rebound characteristics, and erosion or deposition patterns within turbomachinery. Both experiments and computations show that deposition or erosion is more common when particle inertia leads to more concentrated impacts on solid surfaces. Likewise, several researchers have investigated the aerodynamic and heat transfer consequences of deposition or foreign particle ingestion. Bons [5] discusses several studies about how the surface roughness in turbomachinery is increased due to deposition. This increase in surface roughness enhances heat transfer and total pressure losses. Large-scale deposit buildup near film cooling holes interferes with film cooling and can decrease cooling effectiveness. Abuaf et al. [6] described the sensitivity of surface roughness in turbine components on performance and efficiency, so even small traces of deposition are expected to have an effect. Sundaram and Thole [7] investigated the effects of surface deposition, hole blockage, and spallation in a scaled-up, low-speed wind tunnel, matching

the relevant non-dimensional parameters. Data for deposit geometries were acquired from studies by Bons et al. [8]. They showed that partially blocked film holes have the greatest detrimental effect on heat transfer due to restricted or redirected coolant flow. In some cases, surface deposition actually improved cooling effectiveness by assisting in surface insulation and film cooling attachment or mixing.

Jensen et al. [9] and Crosby et al. [10] constructed a high temperature wind tunnel to study the effects of particle deposition at engine relevant conditions. Experiments in this accelerated deposition facility allow for particulate-laden flow to impact on test coupons without the expense of larger engine tests. The facility operated at temperatures of 2100°F [1150°C] with engine relevant Mach numbers. Results from these studies confirmed that deposition rates were highly dependent on flow temperature, with a threshold temperature for coal fly ash between 900°C and 1100°C, above which deposition is highly accelerated. Deposition structures on and around film cooling holes were investigated, showing that deposition can adversely interfere with film cooling patterns in turbine components. More recently [11], this facility has been upgraded to increase the flow temperatures up to 2350°F [1288°C]. Tests were run to investigate the transient nature of deposit buildup on test coupons. Results showed that the particle capture efficiency of deposit increased over time, as the presence of deposit increased the likelihood of other particles to stick upon impact. The capture efficiency is a measure of the rate of deposition relative to the amount of particulate fed into the system, related to the other measurements of impact and sticking efficiency defined by equations 1.1-3.

$$\textbf{Impact Efficiency} = \frac{\textbf{Particle Impacts}}{\textbf{Particles Injected}} \qquad \textbf{[1.1]}$$

$$\textbf{Sticking Efficiency} = \frac{\textbf{Particle Sticks}}{\textbf{Particle Impacts}} \qquad \textbf{[1.2]}$$

$$\textbf{Capture Efficiency} = \frac{\textbf{Particle Sticks}}{\textbf{Particles Injected}} = \textbf{Impact Efficiency} \times \textbf{Sticking Efficiency} \quad [\ 1.3\ ]$$

Murphy et al. also constructed a facility capable of flow temperatures up to 2350°F [1288°C] with particle-laden flow impinging on an angled, film-cooled, TBC (thermal barrier coating) coupon [12][13]. Experiments were run investigating the influence of blowing ratio, TBC coating, free stream temperature, and impingement angle on deposition. Unlike previous experiments, very little deposition occurred at temperatures below about 2200°F [1200°C]. The coupon was cooled, suggesting that the surface temperature or thermal boundary layer has a large influence on preventing deposit buildup.

A similar facility was constructed by Smith et al. [14], allowing for testing on actual turbine hardware. The test section allows for deposition to be simulated on an annular sector of four nozzle guide vanes, capable of engine-relevant temperatures and Mach numbers. The facility allowed for film cooling of the turbine vanes, with particulate-laden flow supplied to either the main hot gas path or the coolant flow. The facility is referenced in this paper as the TuRFR (Turbine Reaction Flow Rig).

Because of the restrictions and expense of high temperature experiments, other researchers have studied deposition using lower temperature facilities. Lawson and Thole [15] utilized a low-speed, low-temperature wind tunnel with dispersed wax particles to simulate coal fly ash deposition. By matching the inertial Stokes numbers of the wax particles, as well as the non-dimensional flow temperature relative to the particle melting temperature, the same characteristics of deposition were simulated compared to high

temperature experiments. The Stokes number is a non-dimensional parameter comparing the particle drag forces to inertial forces, and is defined as

$$\boldsymbol{St_k = \frac{\rho_p d_p^2 V_0}{18 \mu_f l_c}} \qquad \textbf{[1.4]}$$

where ρ_p is the particle density, d_p is the particle diameter, V_0 is the characteristic velocity, μ_f is the fluid viscosity, and l_c is a characteristic length scale. Wax was injected into the flow upstream of the test section through spray nozzles in a molten or semi-molten state. Tests were run investigating deposition near film cooling holes and the effect of deposition on film cooling effectiveness. It was shown that higher rates of film cooling decreased rates of deposit buildup both due to decreased surface temperature and the deflection of small particles by the film cooling gas. Another study investigated deposition buildup near film cooling holes on both flat and contoured endwalls [16]. For the contoured endwall case, it was shown that the leeward sides of the endwall contours were more susceptible to deposition due to increased inertial impacts. Albert and Bogard [17] utilized the same technique in their low-speed wind tunnel and investigated wax deposit buildup through a vane passage near various film cooling configurations. They likewise confirmed that deposition rates were inversely proportional to the vane surface temperature. In a study involving a trench film cooling geometry, it was found the wax deposit accumulates on the downstream side of the trench. Wood [18] performed similar experiments involving deposition near film cooling holes, using semi-molten particles of Teflon or PVC (polyvinyl chloride) instead of ash or wax. He showed that particle deposition followed a nearly logarithmic trend with temperature, where higher temperatures result in increasingly higher deposition rates.

1.2 Computational Modeling of Deposition

Research regarding the computational modeling in internal cooling passages of nozzle guide vanes requires a thorough understanding of prior experimental and computational deposition research, particle tracking and impact characteristics, and validated practices of computational fluid dynamics.

Numerical models of deposition have been the focus of much exploration due to the freedoms that computational fluid dynamic research affords. The general strategy for most computational models involves the Eulerian-Lagrangian particle tracking technique [4]. The fluid flow field is computed independent of particulate matter (Eulerian) and particles are individually tracked by integrating the forces on the particle (drag, gravity, etc.) through a Lagrangian reference frame. Elghobashi [19] showed that one-way coupling can be employed when the volumetric flow rate of the particulate is separated from the volumetric flow rate of the fluid by six orders of magnitude (see Figure 1.2, Φ_P is volumetric ratio of particulate flow to fluid flow). One-way coupling implies that while the fluid certainly imposes forces on the tracked particles, such as viscous drag, the particles impose no significant influence on the fluid. For volumetric fractions above 10^{-6} and below 10^{-3}, particles may exchange momentum or heat to the fluid, and enhance or dissipate the fluid turbulence, depending principally on the particle size. For these conditions particle-particle interactions may still be neglected (two-way coupling). For volumetric flow rate fractions above 10^{-3}, particles interact with other particles, requiring a four-way coupling approach.

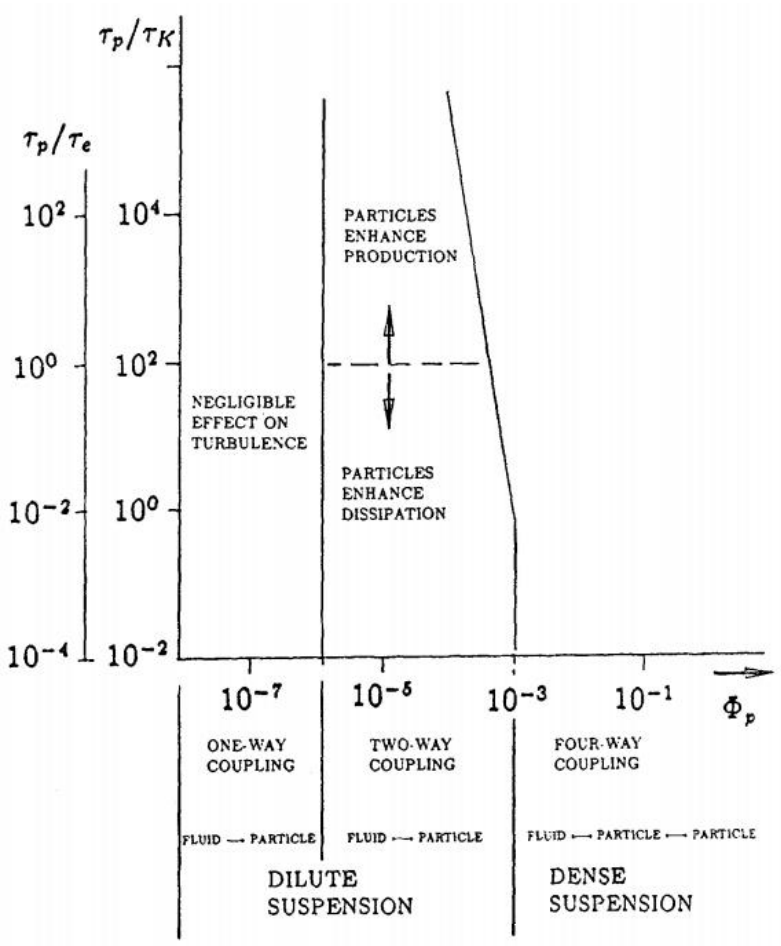

Figure 1.2 – Regimes showing interaction effects for particle-laden flows, from [19]

Hossain and Naser [20] utilized this approach to track particles around pipe bends and found that small diameter particles were less likely to deposit on the walls because they had a higher tendency to follow the flow. Larger particles, corresponding to larger Stokes numbers, were more likely to deviate from the flow and deposit on the walls. Tabakoff et al. [21] numerically and experimentally tracked particle trajectories through an axial turbine to predict erosion patterns and determine locations susceptible to higher

erosion rates. This particle tracking technique has been utilized for validation of several other erosion and deposition studies [4].

While particle tracking is necessary to determine locations of particle impacts, it is necessary in computational models to understand how particles behave upon impact. Brach et al. [22] performed multiple experiments investigating the impact qualities of microparticles. Several experiments were conducted with impacting small particles against flat surfaces, varying factors such as particle size, impact velocity, etc. The coefficients of restitution for microspheres were shown to decrease quickly below a certain impact velocity, with a coefficient of zero below a critical impact velocity. The coefficient of zero indicates that the particle doesn't rebound but rather sticks to the surface. This occurs because the particle does not retain enough kinetic energy to overcome the dissipative adhesion forces between the particle and wall. It was shown that the critical impact velocity was inversely proportional to the size of the particles, as the adhesion forces, of which the van der Waals force is the most dominant, has the largest effect on small particles. This model was applied to predict particle sticking in a nozzle guide vane passage by El-Batsh and Haselbacher [23]. They modeled a 2D turbine vane cascade to study the locations where deposition was most likely. Particles were tracked, and criteria were determined for particle sticking or detachment upon impacts with solid surfaces. Ai [24] modified the sticking model developed by El-Batsh and Haselbacher and calibrated it to match experimental results.

Tafti and Sreedharan [25] developed an alternate sticking model using the coal ash composition to determine a sticking probability based on the viscosity-temperature relationship. At high temperatures, particles are more likely to deposit because they

impact in a molten or semi-molten state. Senior and Srinivasachar [26] developed a correlation to predict the viscosity of coal ash based on its chemical composition and temperature. This was used by Tafti and Sreedharan, in conjunction with a critical sticking temperature for the ash. Above this critical temperature, particles were assumed to always stick upon impact. Below this temperature, particles were given a probability of sticking equal to the ratio of the particle viscosity at the temperature of impact, and the particle viscosity at the critical sticking temperature.

Most computational deposition studies do not account for large-scale buildup of deposit or adaptations of the computational mesh. Rather, the computational models generally account only for the rate of deposition growth on an unchanging surface. Wenglarz [27] constructed a one-dimensional model to predict thickness of deposit and resulting flow restriction through a turbine stator. El-Batsh [28] attempted grid adaptation using three separate techniques in his deposition study on a two-dimensional turbine vane. The first involved changing individual fluid cells to solid wall cells when the accumulated local deposit growth exceeded the volume of the fluid cell. This proved too problematic in that the flow solution would often not converge as the wall boundary became very irregular. The second method involved the relocation of grid nodes through mesh stretching as a result of deposit growth. This too proved problematic as several nodes required relocation due to movement of a single cell at the wall. Even with the movement of multiple cells, the grid had a tendency to fold or overlap on itself with greater deposit growth, preventing accurate flow solutions from being acquired. The third solution involved completely recreating the grid outside of the flow software. This method was certainly the most time consuming, in that not only did the mesh have to be

completely remade, but the flow solution had to be rebuilt and converged. However, this method did allow for flow solutions that converged and the deposition model was executed using this method. Because of the computational and time expense, only a few growth iterations were run. Several have employed similar techniques to model ice accretion on airfoils, but these were either two-dimensional or pseudo-two dimensional [29]-[32]. While most employed first order time stepping techniques, Mingione and Brandi [29] employ a two-step, predictor-corrector method to model each step-change in geometry, analogous to the modified Euler method [33] for approximating differential equations.

Despite the damage that is caused by deposition on the external surfaces of turbine components, such as reducing the vane throat area or clogging film holes, the deposition may actually be beneficial to the component by reducing the material temperature. As the deposit material has a low thermal conductivity, large-scale deposit acts to insulate the underlying parts, protecting them from the hot free stream gases [7]. However, when particles deposit on the internal surfaces, the effect is reversed and any deposition further exposes the part to higher temperatures and greater damage. Previously noted studies have focused on deposition almost exclusively on deposition on the external surfaces of turbine walls, with little consideration to deposition on internal surfaces.

1.3 Impingement Film Cooling with Deposition

One common internal cooling method for nozzle guide vanes involves a combination of impingement cooling and film cooling, also referred to as a double wall. Coolant flow is supplied to internal passages and passes through a perforated impingement plate as jets which impinge on the internal surface of the outer wall. The

coolant then exhausts through film holes into the external hot flow, as illustrated in Figure 1.3.

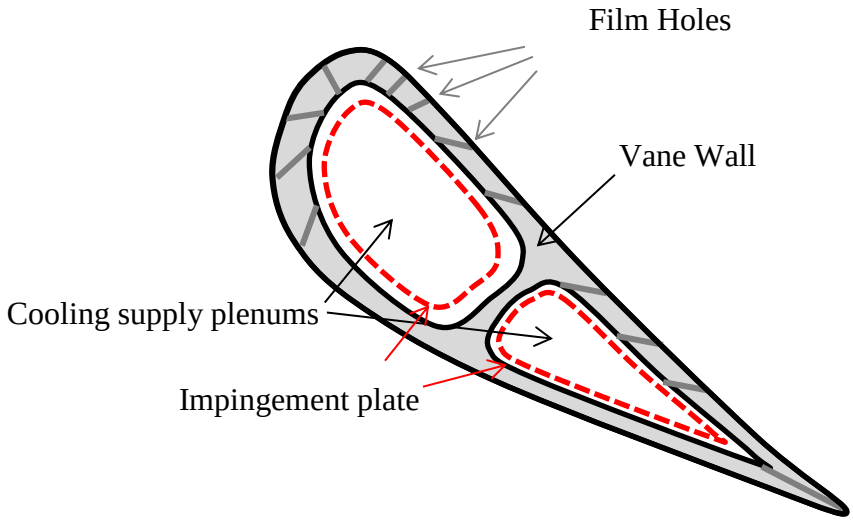

Figure 1.3 – Schematic of nozzle guide vane with impingement and film cooling

Several experiments and computations of impingement cooling, without deposition, have been discussed by Zuckerman and Lior [34]. Figure 1.4 shows a schematic of jet impingement. The flow field of the impingement jet involves multiple distinct features. The free jet exits the orifice hole with nearly uniform velocity, and depending on the gap distance, the edges of the fluid jet interact with surrounding fluid through shear. Near the wall, the jet is rapidly decelerated, and radial flow develops and accelerates in what is referred to as wall jets. In the case of impingement jet arrays, the wall jets interact with those from adjacent impinging jets, creating “fountain” regions where the wall jets separate from the wall and move fluid in the normal direction. These flow structures are efficient in exchanging heat between the wall and coolant fluid.

The rate of heat transfer is dependent on several variables; among which is the ratio between gap spacing and hole diameter. The spacing in the turbine vanes has a gap to diameter ratio of about 1–2. The moderately small gap distance is advantageous due to space considerations. It also performs well without the large pressure losses associated with even smaller gap spacing [35].

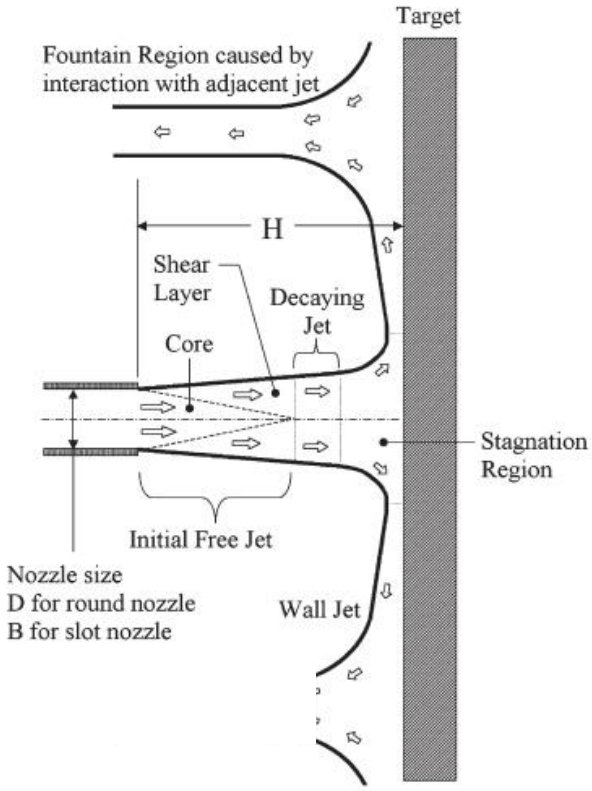

Figure 1.4 – Schematic of impinging fluid jets, from [33].

For computational modeling of impingement cooling without deposition, Zuckerman and Lior discuss various turbulence models for jet impingement applications. They concluded that many of the RANS (Reynolds Averaged Navier Stokes) models performed poorly in predicting heat transfer from the impinging jets, including the

popular k-ω and k-ε turbulence models and the more computationally expensive RSM (Reynolds Stress Model). Transient models such as LES (Large Eddy Simulation) were the best performing, though this came at high computational expense. The k-ω SST and v^2f turbulence model did perform well, with the v^2f turbulence model performing somewhat better than the k-ω SST relative to heat transfer rates. Unfortunately, this model was not available for use in the commercial code used for this study.

Two relevant experimental studies involving deposition in turbine cooling passages were performed by Cardwell et al. [36] and Land et al. [37]. A double-wall test section was designed to represent the impingement liner and film cooled vane wall. Heated flow was supplied to a plenum at constant pressure, which then passed through an impingement liner and film cooling plate coupon, separated by a spacer plate to maintain a constant impingement cavity gap. The test section was located within an electric kiln, allowing for the heating of the test section walls to temperatures up to 982 °C. Sand was injected upstream of the impingement liner allowing for the simulation of deposition within the impingement cavity or other parts of the test section. Cardwell et al. investigated the blockage that occurred due to the injected sand and its relationship to different impingement configurations, temperatures, and pressure ratios. It was found that for lower temperatures, flow blockage was inversely proportional to impingement liner flow area. Deposition increased with increased temperature, but no significant deposit was observed at ambient temperatures. When deposit did form, it did so predominantly on the upstream surface of the film cooling plate, either as individual mounds associated with the individual impingement jets, or lightly coating the area between adjacent impingement jets (Figure 1.5).

Land et al. also used this facility to investigate flow blockage based on other parameters. It was found that blockage levels decreased with increasing pressure ratios from 1.02 to 1.1, and decreased with increasing pressure ratios above 1.1. Blockage also increased with increased cavity spacing and alignment between the impingement holes and film holes. It was determined that particles impinging on the upstream surface of the film hole plate were broken up into smaller particles, which reduced the propensity for accumulation or flow blockage. Land et al. also observed the same deposition patterns on the upstream side of the film cooling plate. These deposition patterns are dominated by the configurations of the impingement jets, with little dependence on the configuration of the film cooling holes. The deposition patterns presented two distinct formats, as individual deposition mounds associated with the individual impingement jets, or as a coating of deposit on the wall except for the region where the jets impinge on the wall (see Figure 1.5). For Figure 1.5, "S/D" refers to the ratio of the distance between the wall and impingement plate to the diameter of the impingement holes.

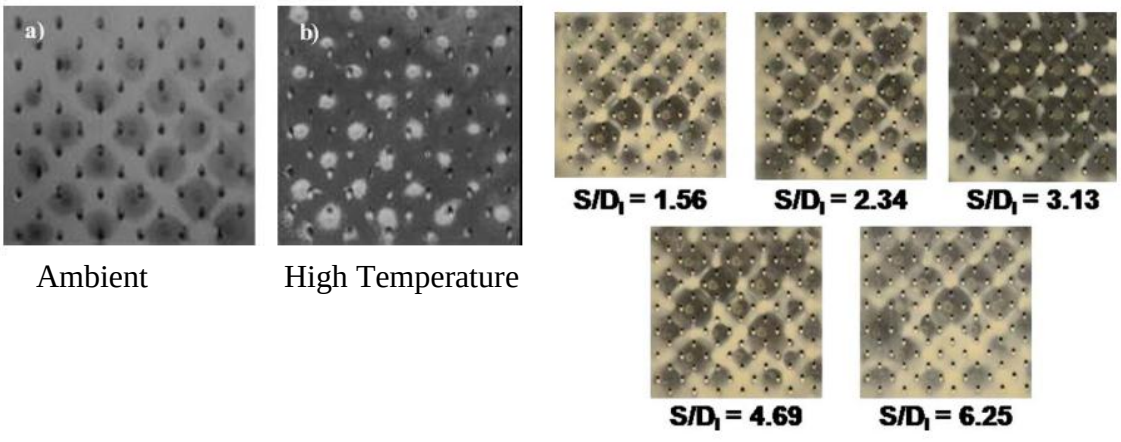

Figure 1.5 – Deposition patterns on upstream film cooling plates from (left) Cardwell et al. [36] and (right) Land et al. [37]

In both of these studies, it was found that the impingement liner served as a filter for particles larger in diameter than the impingement holes, and that individual particles led to blockage by restricting flow through impingement or film holes. The impingement holes were nominally 600 µm in diameter, and approximately 7% of the mass of the particles exceeded this size. Over half of the mass of the particles was measured to have particle diameters over 50 µm. Dunn [1] found that particles ingested into a turbine engine were pulverized by the compressor and that those particles entering the combustor or turbine sections had average diameters less than 8 µm. The flow that feeds the film cooling sections of the turbine is supplied by the last stages of the compressor section, meaning that any large particles in these cooling lines would have already been broken down. The sizes used in [36] and [37] are therefore much larger than what is expected in actual turbomachinery applications.

Chapter 2. Motivation and Experimental Methods

The objective of this research was to increase the accuracy and fidelity of computational models of particle deposition applicable to internal cavities of turbine components. This was done by conducting experiments and computational simulations to determine which factors are dominant in facilitating deposit accumulation. To date, computational models fail to predict critical features of deposition, and both computational and experimental research in this area is very limited.

Deposition in internal cavities poses an added thermal risk compared to external deposition. While deposition on the external surfaces of turbine vanes is problematic due to increased surface roughness, restricted flow, and other aerodynamic losses, the presence of the particulate can be thermally beneficial to the surface in that it insulates the material with its lower thermal conductivity. Deposition in internal cavities has the opposite effect, insulating the vane wall from the coolant flow, thus leaving the vane unprotected from the hot flow. This is illustrated in a simplified schematic in Figure 2.1 with the accompanying 1-D heat transfer analysis. In this case, fluid convection coefficients and thermal properties of the wall and deposit are assumed using values typical of turbomachinery applications. If the temperature difference between the hot external flow and internal flow is 500 °C, a deposit layer only 10% as thick as the wall can decrease the wall temperature by over 75 °C in the case of external deposition, or increase it by 75 °C in the case of internal deposition.

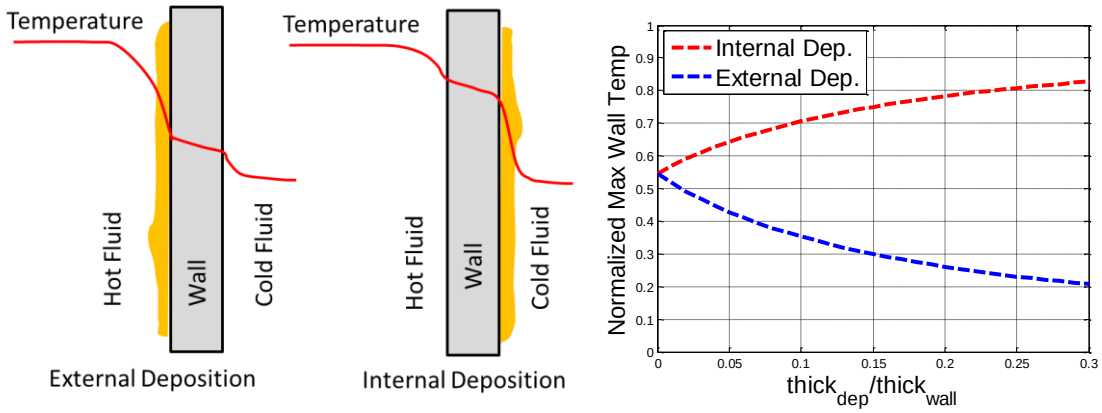

Figure 2.1 – (left) Schematic showing how internal deposition results in higher metal temperature and (right) analysis showing change in vane surface temperature due to deposit thickness

Deposition in internal passages potentially has an adverse influence on critical cooling strategies. As the length scales of internal cooling passages of NGVs are small, even on the same order as the deposit thickness, deposition can severely alter both the aerodynamics and heat transfer to vane or engine component. There are numerous cooling techniques and configurations in turbomachinery, so an accurate and robust deposition model would be beneficial for the prediction or prevention of the harmful effects.

The research was a combination of both experiments and computations studying the effects of internal deposition in simulated impingement cooling cavities. This involved the fabrication and utilization of an experimental test facility to calibrate the computational model. A computational simulation was developed and run to model the growth of deposit through the simplified cooling passage. This section describes the methods and strategies to accomplish these objectives.

2.1 Internal Deposition TuRFR Tests

Experimental tests were conducted on nozzle guide vanes acquired from the commercial aviation industry with particulate-laden flow supplied to the internal cooling cavities. The experiments were conducted in Ohio State University's TuRFR, which simulates flow through an annular section of a nozzle guide vane row. External flow temperatures and Mach numbers were similar to actual engine conditions, with supply flow at 2000 °F and vane exit Mach numbers near unity. Coolant flow was supplied so that the internal cavity pressure was higher than any part of the vane surface, ensuring that no hot external flow was ingested. Coolant fluid temperatures were measured to be approximately 1000 °F (540°C). Particles entrained in the coolant flow entered the coolant cavity, passed through the impingement liner and film holes, and were then entrained into the main gas path, if they didn't deposit on any of the wall surfaces (Refer to Figure 1.3). The majority of deposit occurred on the upstream side of the vane internal cooling cavity wall. Figure 2.2 shows the dust deposit coating an internal wall of a nozzle guide vane after particle injection into the cooling cavities at engine-relevant conditions in the TuRFR facility. The impingement liner was removed to allow for visual inspection of the internal deposit, and the accompanying picture of a full vane doublet provides a reference for the location of the photograph.

Deposition on the internal cavities proved too difficult to measure without destroying the hardware. The impingement insert had to be removed to obtain visual inspection of the deposit, and the removal caused the destruction of many of the deposit structures. For these reasons, it was decided that the actual hardware would be replaced with a simplified geometry for both experiments and computations that could be

adequately controlled and measured. These experimental tests in the TuRFR did show, however, that deposit forms predominantly as individual mounds on the internal vane walls, corresponding to individual impingement jets from the perforated impingement liner. It was also observed that the deposit formations were unaffected by the film holes within the vane wall.

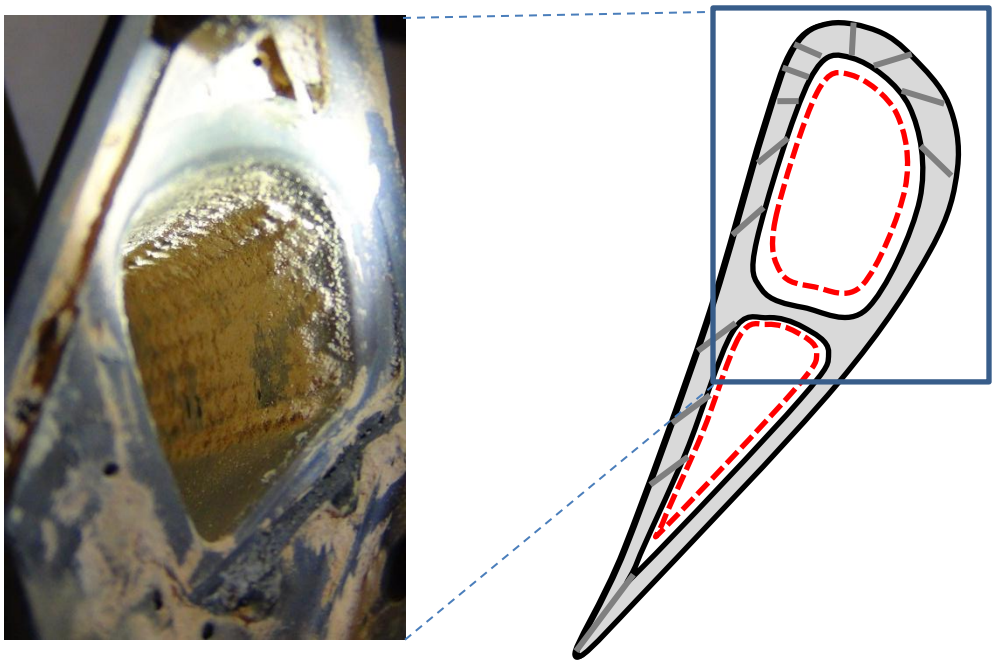

Figure 2.2 – (left) Internal cavity of nozzle guide vane leading edge without impingement insert after internal deposition experiment and (right) representation of turbine vane showing portion represented in left photograph

2.2 Experimental Facility

2.2.1 Test Section

An experimental facility was fabricated to study the buildup of particle deposition in the internal cooling passages of NGVs. The tests were designed to simulate the region between the vane walls and perforated impingement liners where deposition was

observed to develop. In order to isolate the effects that lead to deposition, and provide a geometry that can be readily compared and validated with computations, a simplified geometry was created as a test section. Heated, particle-laden air passes through a perforated stainless steel sheet and impinges on an Inconel plate, representative of an impingement cooled NGV. For simplicity, the impingement plate is flat and does not contain film cooling holes as would be present in an actual NGV, and the air exhausts through the gap between the perforated sheet and plate, as illustrated in Figure 2.3. All dimensions for the perforated sheet thickness, hole diameter and spacing, as well as plate thickness and gap spacing, are representative of actual turbine engine configurations.

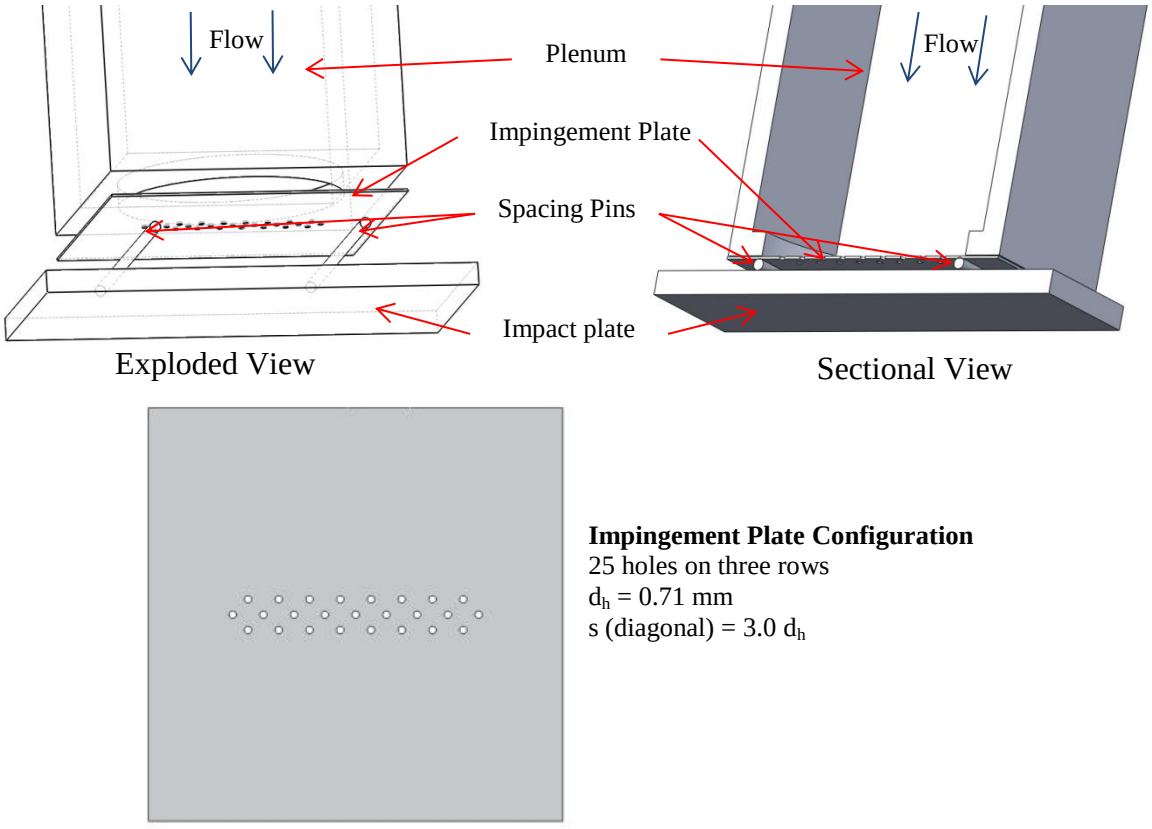

Figure 2.3 – Experimental test piece showing simplified geometry representing impingement cooling cavities of an NGV.

The test piece simplifies the internal cooling passage while maintaining important characteristics that were investigated in this study. The following list shows the similarities and differences of the test section geometry with the internal passages of an impingement-cooled NGV.

Matches	**Ignores**
• Double-wall (impingement insert/solid wall) • Hole, hole spacing, and gap geometry • Internal cooling temperatures (limited by experiment) • Materials (Stainless steel impingement liner, Inconel Impact plate, Arizona Road Dust particulate) • Elevated film plate temperature (limited by experiment)	• Film cooling holes • External hot gas flow • Non-uniform flow upstream of the impingement holes

The test piece was designed to closely match the internal cavities of actual engine hardware in areas that are expected to influence particle deposition. The major difference in the setup is the lack of film cooling holes and hot external flow. It is not expected that these features have a large effect on internal deposition, and is justified by the TuRFR experiments and prior research in [36][37]. In these studies, as observed in Figure 1.5 and Figure 2.2, the deposition patterns are defined by the impingement hole configurations, and not by the film cooling holes. However, the temperature of the impact plate is expected to have an influence on deposition, which is caused by the presence of external hot flow and consequently increase deposition rates. For the experiments, the impact plate can be heated by a flame torch and thus account for higher wall temperatures.

Because the test section does not contain film cooling holes, the flow must exhaust elsewhere. The test section allows for the flow to exhaust to ambient in the direction perpendicular to the impingement hole rows and parallel to the impact plate. This is illustrated in Figure 2.4.

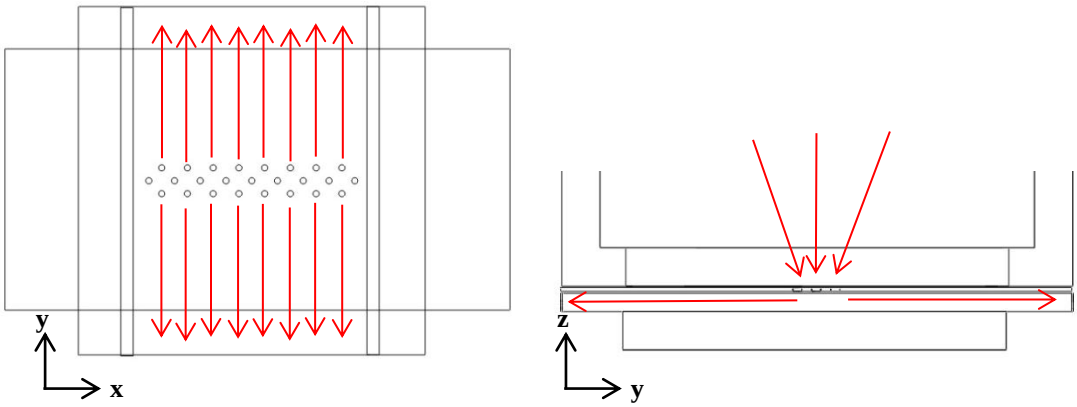

Figure 2.4 – Representation of flow in test section in (left) x-y plane and (right) y-z plane.

The other major difference is the lack of non-uniform flow upstream of the impingement liner. It is assumed that the flow stagnates in the cavity upstream of the impingement holes but this is only partially true in the vane geometry. The area ratio of the sum of all of the holes in the leading edge cavity compared to the inlet area of the cavity is less than 1:2, indicating potential upstream influence. From prior deposition tests in the TuRFR, there is no evidence, however, that this had a significant impact. For the simplified geometry, the area ratio was approximately 1:20 at the narrowest point of the plenum, allowing for ease in computing the flow field and ensuring uniform flow to the impingement holes.

2.2.2 Supply System

Particle-laden flow is supplied to the test section according to the diagram in Figure 2.5.

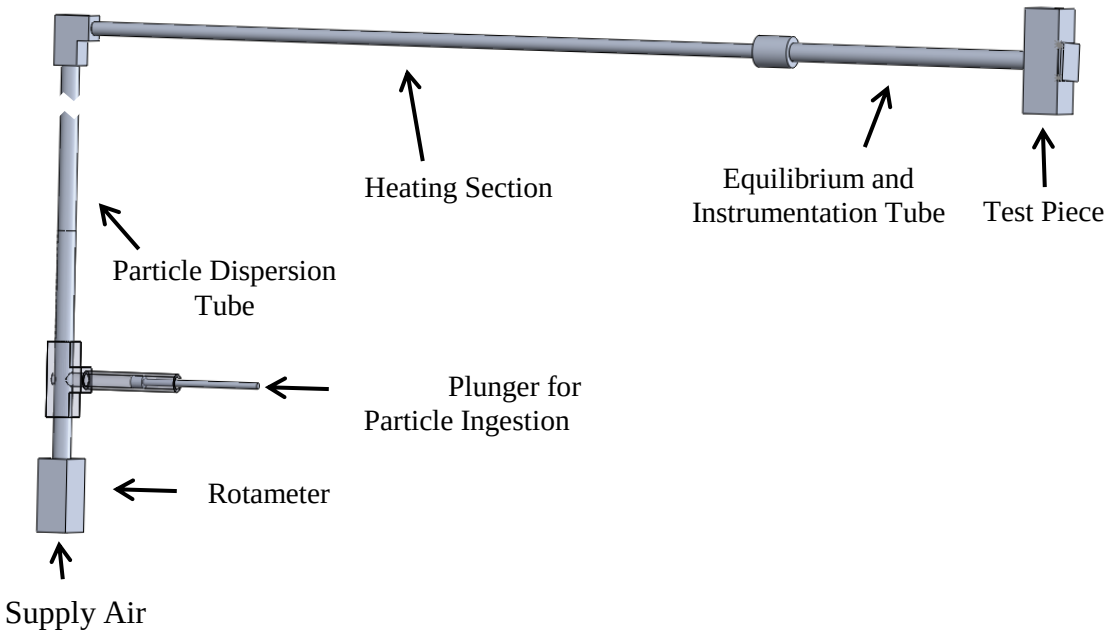

Figure 2.5 – Diagram of experimental facility

Air is supplied from high pressure tanks and passes through a pressure regulator and mass flow meter. The flow meter ranges from 0.4 to 4.0 scfm (standard cubic feet per minute), with increments of 0.2 scfm and an uncertainty of ±0.05 scfm. For each test, the pressure regulator is controlled to maintain a constant flow rate.

Particles are injected through use of a syringe fabricated with clear PVC. The syringe can hold 1-3 grams of the dust used in the study. A threaded plunger was fabricated to slowly and evenly inject the particulate into the flow stream, directly

downstream of the flow meter. For the tests in this study, a total amount of 2.0g or 1.0g of dust was injected at a rate of about 0.33 g/min.

The dust particulate has a tendency to enter the flow stream in small clumps, and must be broken up prior to reaching the test section. If the particulate enters the test section as clumps, it may behave as unrealistically large particles and clog impingement holes. A twenty-foot section of smooth rubber tubing was added to provide for a longer residence time and allow for the particulate to become evenly dispersed. The rubber tubing is also advantageous in that the particles do not easily stick to the internal walls of the tubing compared to other materials. Beyond the rubber tubing, the heating system allows for continued particle dispersion.

2.2.3 Heating System

The heating system was designed to heat the flow to temperatures above 1000 °F without altering the gas chemical composition and also to prevent the particulate matter from accumulating in the heating section. The system consists of a six foot length of brass or stainless steel pipe wrapped in three lengths of eight-foot, ultra-high temperature resistance heating tape, rated to function at 1400 °F (See Figure 2.6). The pipe and heating elements were shielded by several inches of high temperature insulating ceramic fabric, which prevents the heat from being lost to the surroundings. Each heating tape length is powered by standard 120 VAC with a rated output of 624 W. This resistive tape heats the metal pipe, which in turn heats the flowing air through convection along with the dispersed particulate matter. The inner diameter of the pipe was 0.3 inches, which promoted turbulent flow and increased heat transfer through the pipe. The internal walls of the pipe were smooth, without any obstructions, preventing particulate buildup within

the heating section. The heating system was able to deliver unobstructed, particle-laden flow to the test section at temperatures exceeding 1000 °F. The particulate matter is expected to reach thermal equilibrium with the flow through a distance on the order of 1.0 cm (analysis in section 3.3.5).

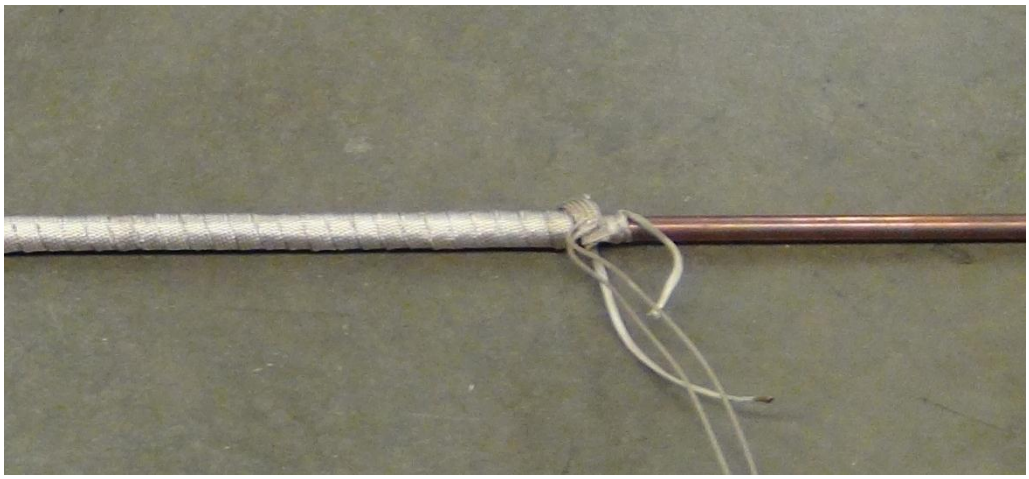

Figure 2.6 – Section of heating pipe wrapped with resistive heating tape

A K-type thermocouple and total pressure probe measure the air temperature and pressure immediately upstream of the test section plenum. These values were continually monitored and recorded during each experimental test.

For tests involving a heated impact plate, a Benzomatic flame torch is positioned to impinge on the backside of the plate. Thermocouple readings indicate that the flame impingement increased the plate temperature to about 1350 °F at steady state conditions. Infrared thermography showed uniformity in temperature for the regions where deposition is expected to accumulate, shown in the non-dimensional temperature measurements on the impact plate in Figure 2.7. This figure, with impingement hole

locations illustrated for reference, show near uniformity for the region of interest. The temperature difference on the plate relative to the impingement hole locations ranged by about 30 °F.

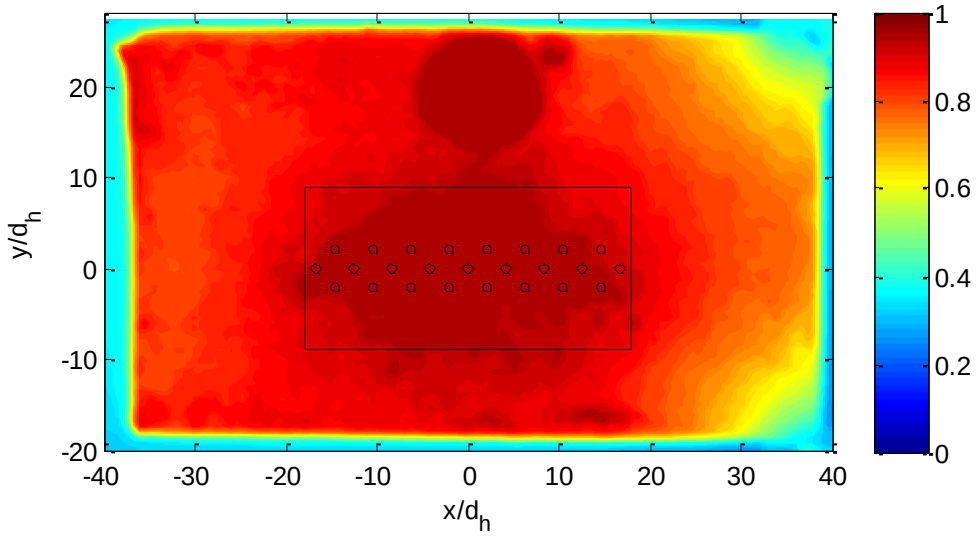

Figure 2.7 – Non-dimensional temperature contours of flame impinged impact plate.

The region between the perforated plate and the heated impact plate has open optical access for video recording of deposition buildup. The spacing of the gap is kept constant through the use of two Inconel spacing pins, shown in the test section diagram in Figure 2.3. Previous experience shows that deposit forms predominantly as individual conical mounds corresponding to individual impingement holes. A digital camera records the size of the mounds correlating to two of the three rows of impingement holes over the duration of the test. After the test, the plate is scanned to determine the deposit topography and the total mass is removed and measured. The deposit is measured on a digital weight scale with an accuracy of about ±0.0001 gram, or about 1% of a typical

measurement. Other measurements include the test section plenum temperature and pressure, and mass flow rate of both the air and particulate matter. The geometry of the impingement holes, gas velocity and temperature, and particle properties all match conditions that can be replicated in the TuRFR facility and are similar to actual engine configurations.

2.2.4 Particulate Type

The particulate matter used in this study was Arizona Road Dust (ARD) acquired from Powder Technology Inc. The density was measured at 2.65 g/cm^3 and the chemical composition is given in the following table.

Table 2.1 – Particulate matter composition by weight

SiO_2	Al_2O_3	Fe_2O_3	Na_2O	CaO	MgO	TiO_2	K_2O
68-76%	10-15%	2-5%	2-4%	2-5%	1-2%	0.5-1.0%	2-5%

Three nominal sizes of particulate were acquired from a distributor, along with size distributions in mass percentages calculated by a Coulter Multisizer. Unless otherwise noted, the size distribution for the experimental tests in this study used the 0-20 µm distribution, which is an expected distribution of particle sizes that can occur during actual engine operation and is similar in range to those measured by Dunn [1]. The mass median diameters of the 0-20 µm, 0-10 µm, and 0-5 µm distributions are 7.4 µm, 4.1 µm, and 2.0 µm, respectively.

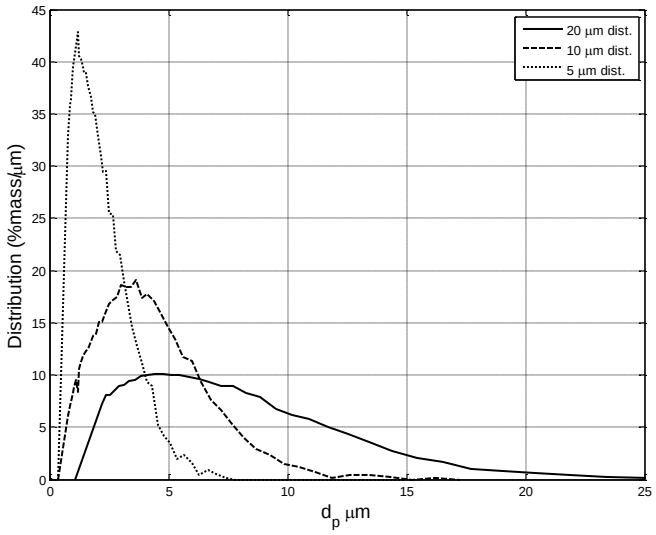

Figure 2.8 – Size Distribution of Arizona Road Dust

Thermal properties of the particulate were not available, but were assumed to be identical to the ash properties used in previous studies [38][39] with the thermal conductivity equal to 0.5 W/m°K and specific heat equal to 984 J/kg°K.

2.2.5 Testing Matrices

Previous deposition studies reveal many factors that affect deposition rates in external deposition studies, such as temperature, fluid velocity, and particle composition. A test matrix was developed to test three factors that may contribute to deposition; flow temperature, plate temperature, and fluid velocity. Initial, exploratory tests were run at three mass flow rates and two flow temperatures. Tests were repeated with a heated impact plate well above the temperature of the impacting fluid. An experiment was run at ambient temperature at the intermediate flow rate, and replicated for the two smaller particle size distributions. All tests were run with the same amount of total particulate matter injected, at 2.0 grams. The test cases are numbered in Table 2.2. The Reynolds

number Re_D is calculated based on the flow properties through the impingement hole by the eqn. 2.1.

$$\mathbf{Re_D} = \frac{\dot{\mathbf{m}}_\mathbf{h} d_h}{A_h \mu_f} \qquad \mathbf{[\ 2.1\ ]}$$

Table 2.2 – Experimental test matrix for 2.0 g injected

Air Flow Rate / Flow Temperature	$\dot{m} = 2.3 \times 10^{-4} kg/s$ $Re_D \sim 500$		$\dot{m} = 4.6 \times 10^{-4} kg/s$ $Re_D \sim 1000$		$\dot{m} = 6.9 \times 10^{-4} kg/s$ $Re_D \sim 1500$	
	Unheated Plate	Heated Plate	Unheated Plate	Heated Plate	Unheated Plate	Heated Plate
70 °F (20 °C)			13a(0-20 µm), 13b(0-10 µm) 13c(0-5 µm)			
700 °F (370 °C)	5	6	1	2	9	10
1000 °F (540 °C)	7	8	3	4	11	12

After these initial tests were conducted, several more were conducted with lower amounts of particulate injected. It was determined, that for some experiments, 2.0 g of particulate saturated the test section with deposit, significantly altering the flow field and making it difficult for comparison with other experimental tests. The repeated tests, with only 1.0 g of particulate, are shown in Table 2.3.

Table 2.3 – Experimental test matrix for 1.0 g injected

Air Flow Rate / Flow Temperature	$\dot{m} = \times 10^{-4}\ kg/s$ $Re_D \sim 500$	$\dot{m} = 4.6 \times 10^{-4}\ kg/s$ $Re_D \sim 1000$		$\dot{m} = 6.9 \times 10^{-4}\ kg/s$ $Re_D \sim 1500$
	Unheated Plate	Unheated Plate	Heated Plate	Unheated Plate
70 °F (20 °C)	-	14(a-c)	-	-
400 °F (205 °C)	-	15(a-c)	-	
700 °F (370 °C)	19(a-c)	16(a-c)	-	20(a-c)
1000 °F (540 °C)	-	17(a-c)	18(a-c)	-

Chapter 3. Computational Methods

The computational model builds on models that have previously been developed (discussed in detail in [38][39]). The deposition involves a one-way coupled, Eulerian-Lagrangian tracking approach used extensively in previous research as explained in the background. The one-way coupled approach assumes that while the fluid certainly affects the flow of the particulate matter, through drag and other forces (discussed in section 3.3), the mass flow rate of the particulate is so low that it has no appreciable effect on the fluid flow field, and that the flow field may be calculated independent of particulate. This is justified because the volumetric flow rate of the particulate matter is separated by six orders of magnitude compared to the fluid flow rate [19].

Two important additions are applied to the model, the first of which involves particle sticking upon impact. Previous research has applied differing forms of the critical velocity model or critical viscosity model for particle sticking. Both of these models have significant shortcomings (discussed later) and are not expected to accurately predict deposition in this setup, so they cannot be applied without modification. Other sticking methods are also investigated for adequacy. In the end, a shear-based sticking model is developed and shows considerable promise for internal deposition applications.

The second addition to the computational model is the transient buildup of ash deposit, changing the geometry and flow solution. The method employed involves the following steps.

1. Define geometry
2. Generate appropriate computational grid
3. Obtain flow solution with accurate boundary conditions
4. Run deposition model and determine the deposition rate on the surfaces
5. Extract a deposit thickness from the deposition rate
6. Establish new surface
7. Repeat steps 1 – 6 until simulation is complete

The progression of these steps incorporated into the entire deposition model is illustrated in Figure 3.1.

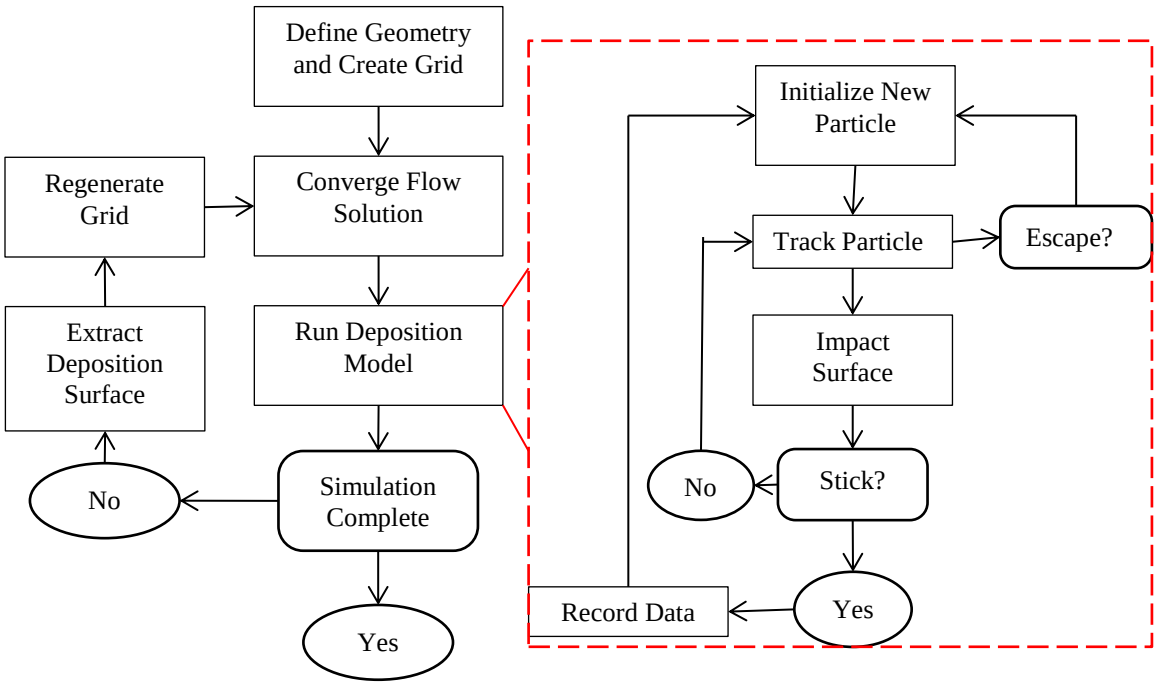

Figure 3.1 – Flowchart of computational model

3.1 Grid Generation

The geometry of the computational domain was defined to match the experimental geometry test section. The hole diameter, hole spacing, gap thickness, and material properties were all matched. The experimental test section simulated three rows of impingement holes, though it is not necessary for all rows to be simulated computationally due to symmetry and periodicity. Figure 3.2 shows a solid model domain of the test section to be modeled computationally.

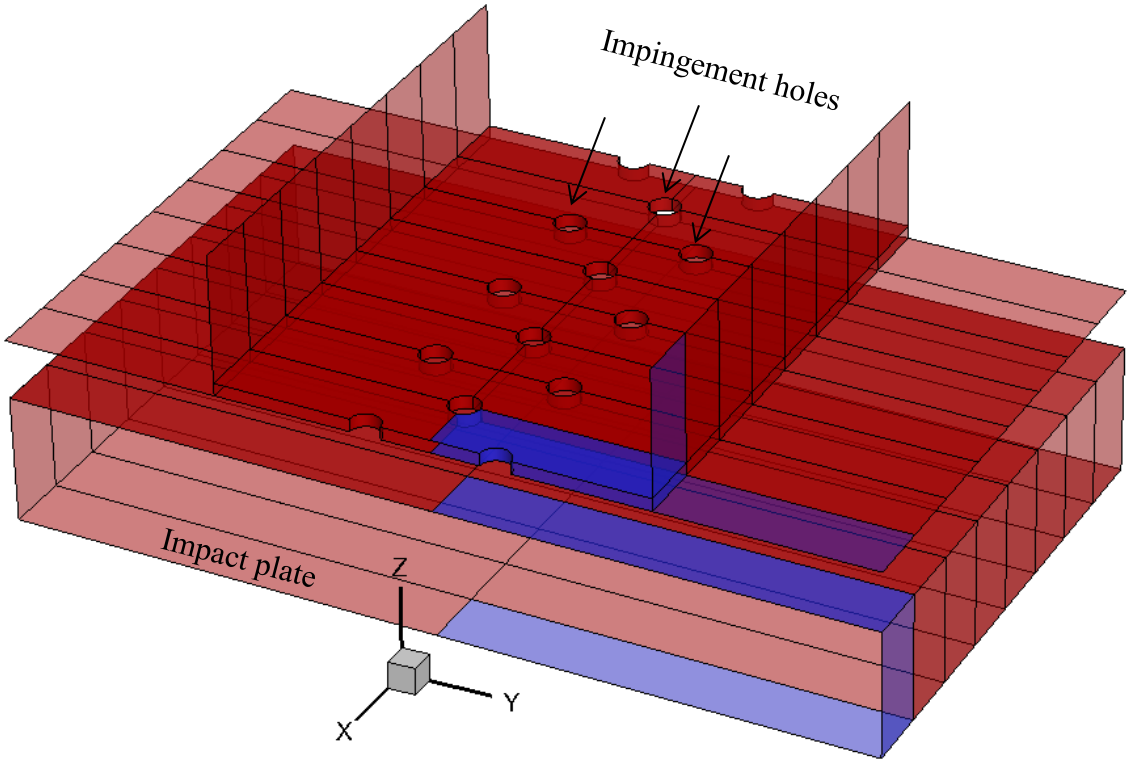

Figure 3.2 – Solid model domain for CFD. Blue highlight represents region to be meshed with symmetry boundaries on three sides.

The solid model shows a section of the impingement holes and solid impact plate. This section ignores the impingement holes on the end of the rows, illustrating the

symmetry and periodicity of the test section. Because of the periodicity, only a small slice was modeled computationally, represented by the blue section in Figure 3.2. This allowed for higher grid density and lower computational cost.

The grid was generated using Gridgen software on an unstructured mesh, refined near the boundary layers and regions of interest (vicinity of impingement holes, impingement jet, wall jet, and fountain regions). Further grid refinement was performed in Fluent software to perform a grid independence study and ensure that all regions of interest are properly converged. All wall cells in the regions of interest had y^+ values on the order of unity.

The grid contained four volumetric regions; the fluid flow path, the perforated plate, the impact plate, and if necessary, the deposit layer. As the grid simulated three patterned rows of impingement jets, symmetry boundary conditions were utilized on three sides to model the array, resulting in only the modeling of a quarter of the center hole and half of one of the outer row holes. A depiction of the geometry, without the deposit layer is shown in Figure 3.3 and a representation of the grid prior to refinement is shown in Figure 3.4.

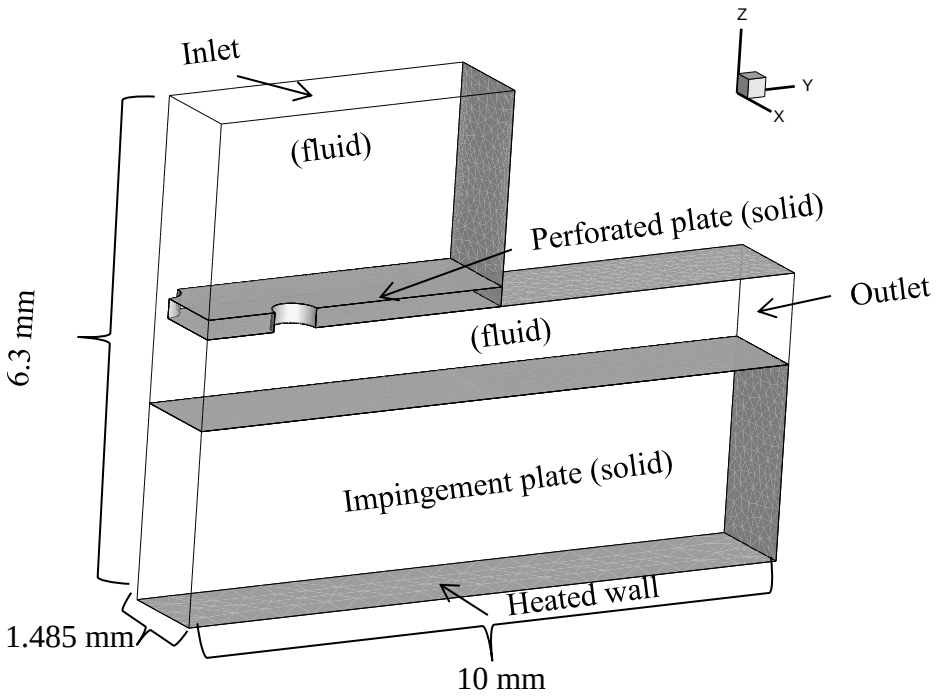

Figure 3.3 – Computational geometry without deposit

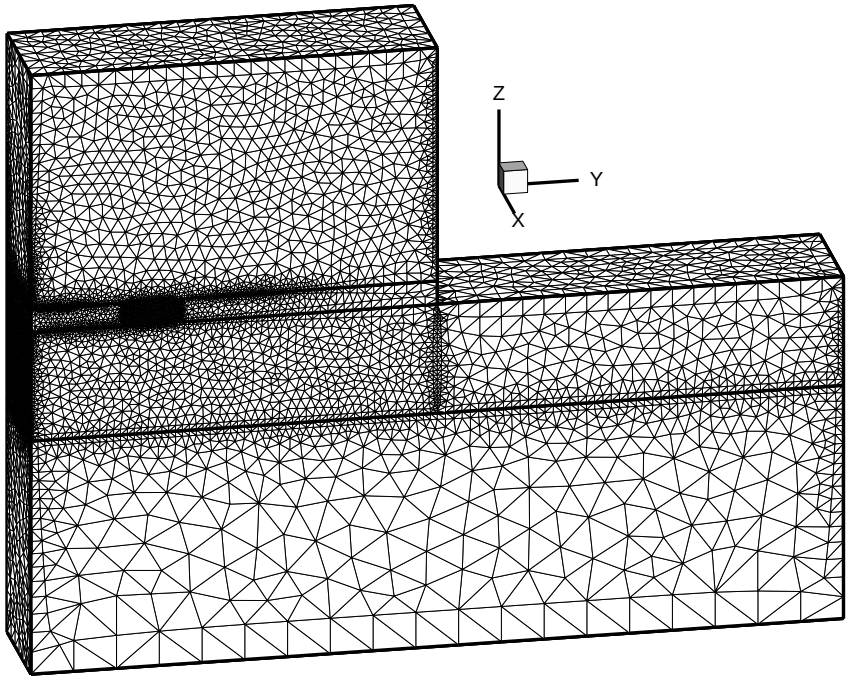

Figure 3.4 – Computational Geometry grid prior to grid refinement

3.2 Flow Solution

The flow solution was calculated using the same boundary conditions that are applied to the experimental tests: velocity and temperature at the inlet to match mass flow with given temperature, and ambient pressure at the flow exit. The turbulence intensity is assumed to be 10% at the inlet. This value was not measured experimentally, though the value was assumed based on fully turbulent pipe flow decelerating into a diffuser and then a plenum. Additionally, simulations showed that the flow solution and particle trajectories downstream of the impingement holes were relatively insensitive to the inlet turbulence with downstream turbulence changing by less than 5% when inlet turbulence changes by a factor of two.

The turbulence model for the simulation was chosen to be the k-ω SST developed by Menter [40]. This method combines the strengths of the two-equation k-ω model near wall boundaries (which is expected to perform well in the wall-jet region) and of the k-ε model which is expected to perform well for the impinging jet in free-shear flow. Zuckerman and Lior [33] state that the k-ω SST and v^2f turbulence models "produce better predictions of fluid properties in impinging jet flows and are recommended as the best compromise between solution speed and accuracy."

Conjugate heat transfer is applied at the fluid-solid and solid-solid interfaces. To simulate the flame impingement heating as conducted in the experimental tests, the external wall of the Inconel plate, not in contact with the fluid, applied a convective boundary condition with an assumed convective coefficient of 1000 exposed to fluid at 1500 °F. This boundary condition resulted in a back side temperature of about 1350 °F, which was measured in the experimental tests with flame impingement. All other walls in

the CFD geometry were given adiabatic boundary conditions. The steel and Inconel test section material, along with the particle deposit, are assumed to have the following constant thermal properties:

Table 3.1 – Thermal Properties of Solid Material

	Density (kg/m3)	Thermal Conductivity (W/m-K)	Specific heat (J/kg-K)
Dust Deposit	1330	0.25	984
Stainless Steel 304	8000	21.5	500
Inconel 625	8400	17.5	536

Gas properties utilized those of dry air treated as an ideal gas, viscosity was modeled using Sutherland's law, and thermal properties were modeled as polynomial functions dependent on temperature.

3.2.1 Flow Solution Validation

The flow solution was compared against experimental data and empirical relations in order to justify the turbulence model and flow solution. However, the flow solution in this study using the three dimensional geometry is unique. Compared to most experimental data, this simulation contains a unique geometry, generally low Reynolds numbers, gap to diameter ratio and hole spacing. To account for this, an alternate mesh was created utilizing similar node spacing and geometries. The mesh was two-dimensional, and simulated a single, axisymmetric hole. The flow Reynolds number was raised to 2000 and inlet temperature was 27°C while the impact plate was held a constant temperature at 37°C. A representation of the flow is shown in Figure 3.5.

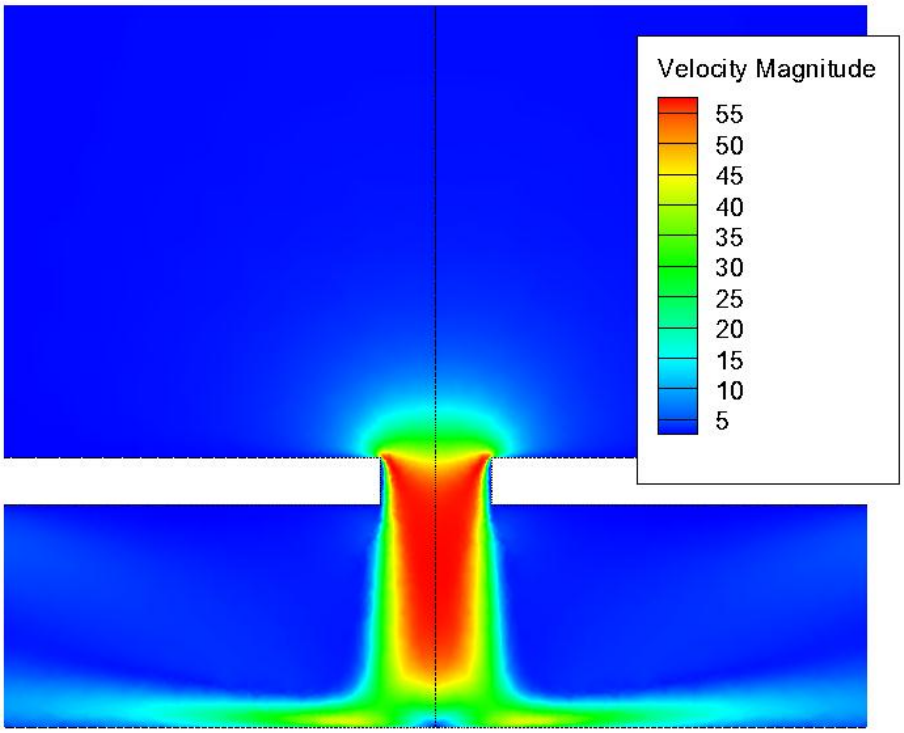

Figure 3.5 – Velocity magnitude (m/s) of flow through a single orifice hole using unstructured, axisymmetric mesh

The flow solution was compared against relations described by Martin [41]. These relations are semi-empirical and analytical solutions for idealized laminar jets, based on the properties of the fluid flow and hole-to-gap distance ratio. For the impinging jets in this study, it is expected that the stagnation region and wall jets near the jet core will resemble these analytical solutions. Figure 3.6 shows the flow centerline velocity, or flow velocity along the axis of rotation. The yellow region represents the location of the impingement plate where the impingement jet begins. The flow near the wall at $z/d_h = 0$ shows deceleration in a nearly linear fashion. This is in agreement with the deceleration associated with the stagnation region predicted by [41], illustrated by the dashed red line that predicts the linear deceleration rate as a function of Reynolds number and geometry.

It is also predicted that the stagnation region is limited to $z/d_h < 1.2$, as this is the point where the centerline flow begins to decelerate. The flow along the center axis is relatively inviscid and incompressible at these velocities, so it is expected that there will be very little total pressure loss. The CFD solution predicts this as well, showing no significant total pressure drop along the axis of rotation. (Total pressure does experience significant pressure loss at higher radial positions, as the wall jets are decelerated by viscosity and turbulent mixing).

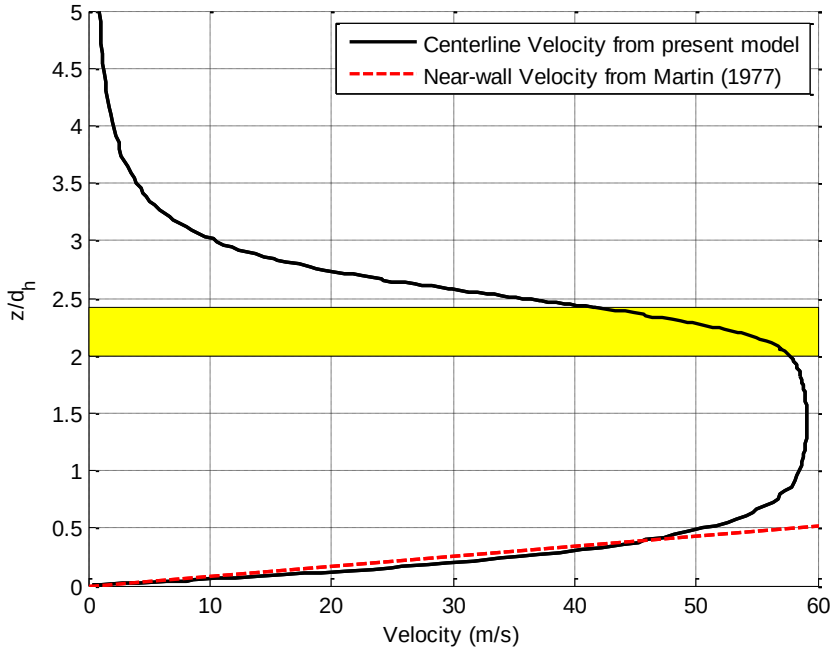

Figure 3.6 – (left) Centerline velocity magnitude through single orifice hole with expected relation from Martin [41] in the stagnation region

The impinging jet on the solid wall results in radial jets seen in Figure 3.5 and illustrated in Figure 1.4. The velocity of these radial jets is also given by correlations in [41] and an illustration is shown in Figure 3.7. There is general agreement in that the

radial velocity increases nearly linearly for $r/d_h < 0.7$, and decelerates at higher radial positions due to viscous dissipation and adverse pressure gradients. The relation from Martin predicts only the acceleration of the wall jets near the core, so it should not be expected to match the actual velocities at higher radial positions.

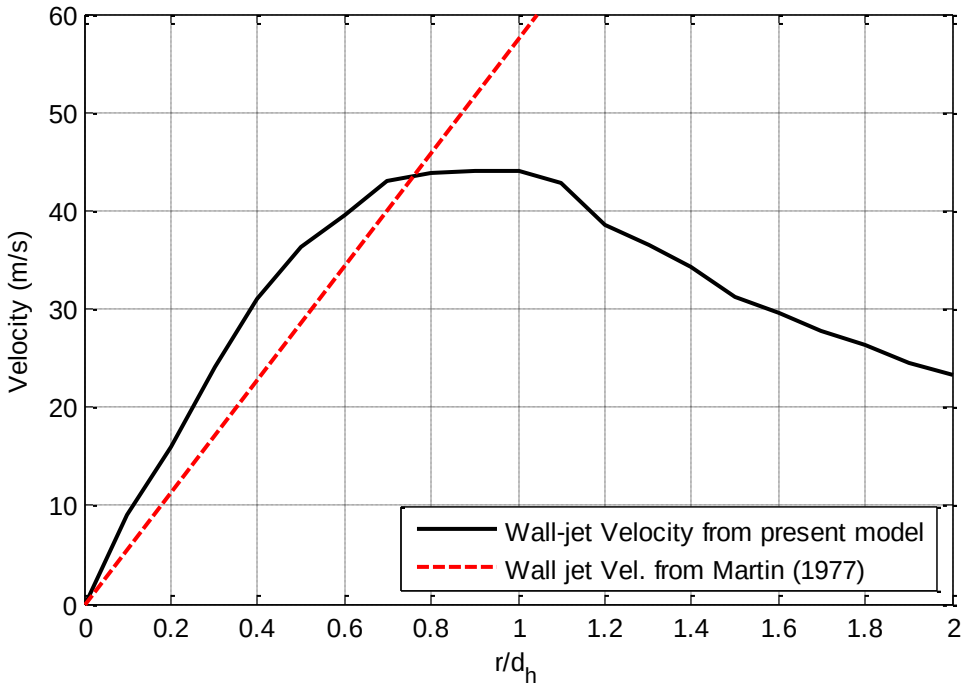

Figure 3.7 – Maximum wall jet velocities in radial direction from impinging jet flow

The average surface Nusselt number below the hole was calculated and compared against the empirical relations from Martin [41]. The average Nusselt number values within $r/dh < 2.5$ were 21.4 for the computation and 24.6 for the Martin relation, or a deviation of 13%. Errors up to 20% were predicted by Zuckerman and Lior for this turbulence model. With these comparisons of impinging jet flow features compared

against experimental data, it was concluded that the flow solution would be adequate for the three dimensional simulations.

3.2.2 Grid Independence Study

Figure 3.8 shows a representation of the flow solution for the test apparatus prior to any deposit growth. The simulation matches the experimental conditions of inflow temperature of 1000 °F with a total mass flow rate of 0.8 scfm.

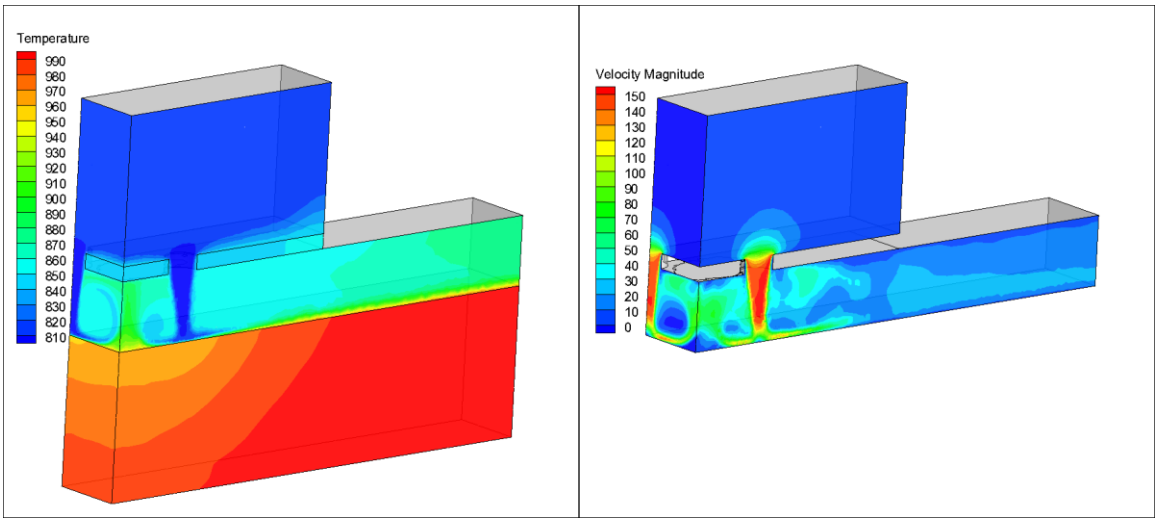

Figure 3.8 – Converged solution showing contours of (a) temperature [°K] and (b) velocity magnitude [m/s]

A grid independence study was performed by monitoring the heat transfer rates on the impact wall in the impingement jet regions and total mass flow rates. This was performed on the geometry without any accumulated deposit. The grid was refined based on mass imbalance and temperature or velocity gradients, with results shown below.

Table 3.2 – Grid Independence

Number of Nodes	Impact Wall Temp (°K)	Relative Change
257,212	919.4	*
493,525	916.9	0.28%
984,855	917.8	0.10%

Total mass flow and pressure values were monitored at the inlet and outlet, and showed no significant change (<0.01%) for the different grid refinements, indicating that the grid was sufficiently refined with 500,000 cells. The solution was converged using second-order upwind discretization schemes and residuals all fell at least three orders of magnitude.

3.3 Particle Tracking

Particles are tracked in a Lagrangian reference frame by integrating the forces on the particle through time and space. The equations of motion for the particles are given below.

$$\frac{d\vec{x}}{dt} = \vec{V} \qquad \textbf{[3.1]}$$

$$\frac{d\vec{V}}{dt} = \vec{a} = \frac{\vec{F}}{m} \qquad \textbf{[3.2]}$$

3.3.1 Drag

Dispersed particles are tracked by integrating the forces on the particle through the flow field. The most dominant of these forces is the drag force, and is responsible for over 90% of the force acting on the particles, and hence acceleration, in this study. The drag force is calculated treating the particles as spherical according to the relation

$$F_D = \frac{1}{2} C_D \rho_f V_{rel}^2 A \qquad \textbf{[3.3]}$$

Because the particles sizes are on the scale of microns, and the Reynolds numbers are well below the turbulent transition region of about 10^5, the drag coefficient is taken from the relation of Morsi and Alexander [42]. When the Reynolds numbers are generally in the Stokes flow regime (Re < 10^2), the drag can be approximated as

$$\boldsymbol{F_D \approx 3\pi\mu_f d_p V_{rel}} \qquad \textbf{[3.4]}$$

Where F_D is the drag force, μ_f is the viscosity of the fluid, d_p is the particle diameter, and V_{rel} is the relative velocity between the particle and the fluid.

A correction is applied to the drag coefficient for very small particles which accounts for molecular boundary layer slip. The correction lowers the drag coefficient for particles on the order of a micron in diameter or smaller. The change in the drag coefficient can be as large as 20%, and as such must be accounted for in order to accurately track the particles in this study. This modified drag law is described by Ounis et al. [43] and is given by the following relation.

$$\boldsymbol{F_{Dc} = \frac{F_D}{C_c}} \qquad \textbf{[3.5]}$$

$$\boldsymbol{C_c = 1 + \frac{2\lambda}{d_p}\left(1.257 + 0.4e^{-(1.1 d_p/2\lambda)}\right)} \qquad \textbf{[3.6]}$$

F_{Dc} is the corrected drag force, C_c is the Cunningham correction factor, and λ is the mean free path of the gas.

3.3.2 Turbulent Diffusion

A random walk technique is used to model turbulent diffusion of the particles. Local turbulence values are extracted from the flow solution to model turbulent eddies acting on the particles. The directional force of the random walk is randomized so that each particle experiences a slightly different trajectory even if they are initialized from

the same location with the same initial properties. The force from turbulence comes by modifying the local flow direction and intensity due to turbulent fluctuations. For two-equation turbulence models such as k-ε, k-ω, or k-ω SST, it is assumed that turbulence is isotropic, and that the turbulent fluctuations may be defined as

$$\sqrt{\overline{u'^2}} = \sqrt{\overline{v'^2}} = \sqrt{\overline{w'^2}} = \sqrt{2k_e/3} \qquad [\ 3.7\ ]$$

At a given point for the particle tracking, the velocity in the x-direction is modified by

$$u' = C_1\sqrt{\overline{u'^2}} \qquad [\ 3.8\ ]$$

where C_1 is a normally distributed random number. The same is applied to the velocity in the other directions. The turbulent fluctuations are applied to the particle being tracked for a characteristic eddy lifetime assumed to be

$$\tau_e = 0.3\frac{k_e}{\varepsilon} \qquad [\ 3.9\ ]$$

This random walk technique assumes isotropic turbulence in all regions of the flow field, which can be problematic in regions of anisotropic turbulence such as the boundary layers. Studies from external deposition modeling provide justification for applying this model in these studies.

3.3.2.1 Deposition Modeling on Turbine Endwalls

Computational studies were conducted investigating the effects of turbine endwalls on deposition, reported in [39]. This paper investigated particle tracking using multiple turbulence models. One problem with particle tracking relates to modeling turbulent diffusion of particles in the boundary layers. For 2-equation turbulence models like k-ε and k-ω, turbulence is assumed to be isotropic. This assumption is applied to the

random walk method, where forces from turbulent eddies are applied equally, on average, in the three spatial dimensions. While this assumption is acceptable for most of the free flow, it does not apply in the boundary layer where the flow is highly anisotropic, as shown by Dehbi [44] (Figure 3.9).

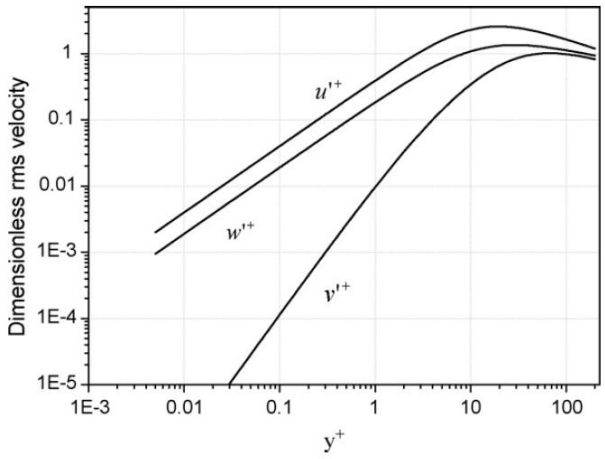

Figure 3.9 – RMS values of velocity showing anisotropic turbulence in boundary layers from Dehbi [44].

The isotropic turbulence assumption in particle tracking results in artificially delivering particles to the wall due to non-physical turbulence. However, the RSM (Reynold's Stress Model) turbulence models do not assume isotropic turbulence, accounting for the three spatial dimensions. As a result, this model does not have a problem with turbulent diffusion in the boundary layers or other locations of anisotropic turbulence. Additionally, these models are advantageous for predicting swirling flows, which are common features of secondary flows near turbine endwalls. For this reason, the stress-ω model was used to computationally model endwall deposition and was concluded to be superior compared to other turbulence models in this area.

Particle trajectories and the resulting deposition are only influenced by secondary flows if the Stokes numbers are sufficiently small. For flow around a blunt leading edge, deposition rates were highest on the center of the leading edge and uniform in the span-wise direction, whereas endwall deposition was highest near the junction with the leading edge, representative of the location of the horseshoe vortex. While the locations of maximum deposition were independent of particle size, the magnitudes of deposition varied significantly. Leading edge deposition increased significantly with Stokes numbers above 0.1, whereas endwall deposition was enhanced at intermediate Stokes numbers. For Stokes numbers above 1.0, endwall deposition diminished as secondary flows and turbulent diffusion had less effect on these larger particles. This is shown in Figure 3.10.

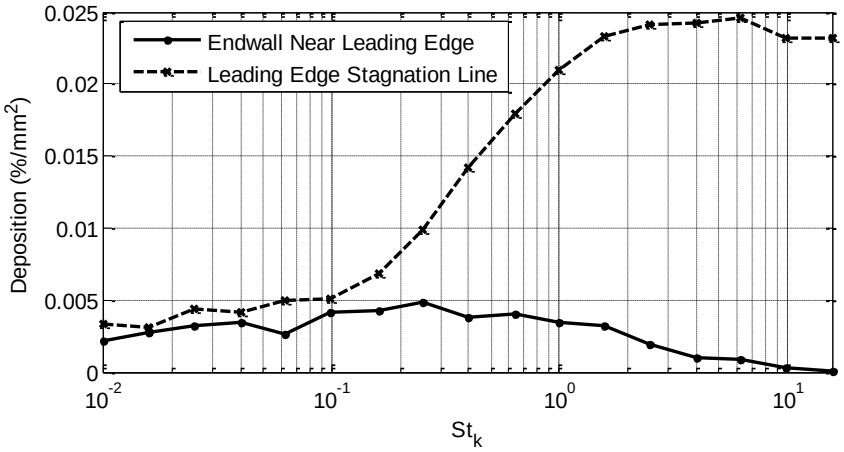

Figure 3.10 - Endwall Deposition rates from [39]

In the studies discussed in this work, the Stokes numbers of the particles exceed 10, so it is assumed that turbulent diffusion in the boundary layers does not have a significant effect. For this reason, the more physically accurate random walk

implementation particular to the RSM models is unnecessary, and less sophisticated turbulence models may be used without significant negative effects of assumed isotropic turbulence in the boundary layers. Thus, it was determined that the k-ω SST turbulence model would not unrealistically affect the particle trajectories in the boundary layers.

3.3.3 Saffman Lift

Saffman lift is the force on a particle in a shear flow. Assuming that the particle is not moving at the same velocity as the local flow, the shear flow results in faster moving fluid around one side of the particle compared to the other, as illustrated in Figure 3.11. The faster moving fluid results in asymmetric pressure around the particle, resulting in a force in the direction of the gradient.

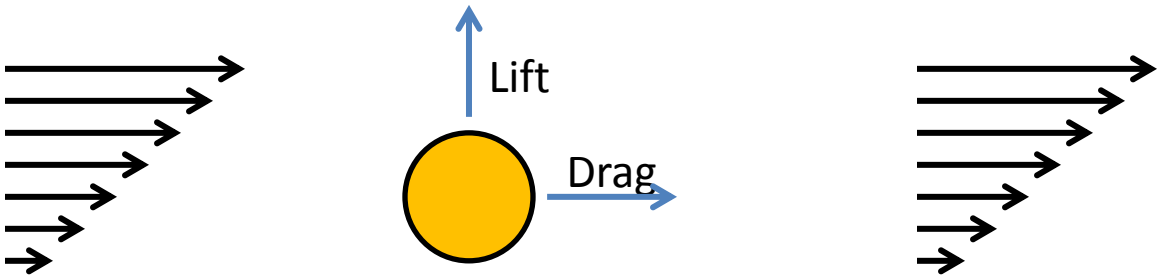

Figure 3.11 – Saffman Lift Illustration

The lift force is given by eqn. 3.10, and a discussion of the lift force is given by Saffman in [45].

$$F_{SL} = 1.615\rho_f \mu_f^{0.5} d_p^2 V_{rel} \sqrt{\frac{du}{dy}} \qquad [3.10]$$

F_{SL} is the Saffman lift force, and ρ_f is the fluid density.

As an applicable example, if a particle moving with the flow enters the flow boundary layer near the wall, the relative velocity of the flow around the particle is faster on the wall-side. The Saffman lift force compels the particle toward the wall. Alternatively, if the particle is moving at a lower velocity than the local flow within a wall boundary layer, the Saffman lift pulls the particle away from the wall.

The Saffman Lift force applies only to small particles on the order of microns, and assumes that particle Reynolds number is small and particle rotation is neglected. The force relative to drag is weak, with magnitudes less than 4%. However, it was still incorporated into the tracking of particles. Additionally, this force only influences particles in regions of high shear. The following plot shows where this force can be important.

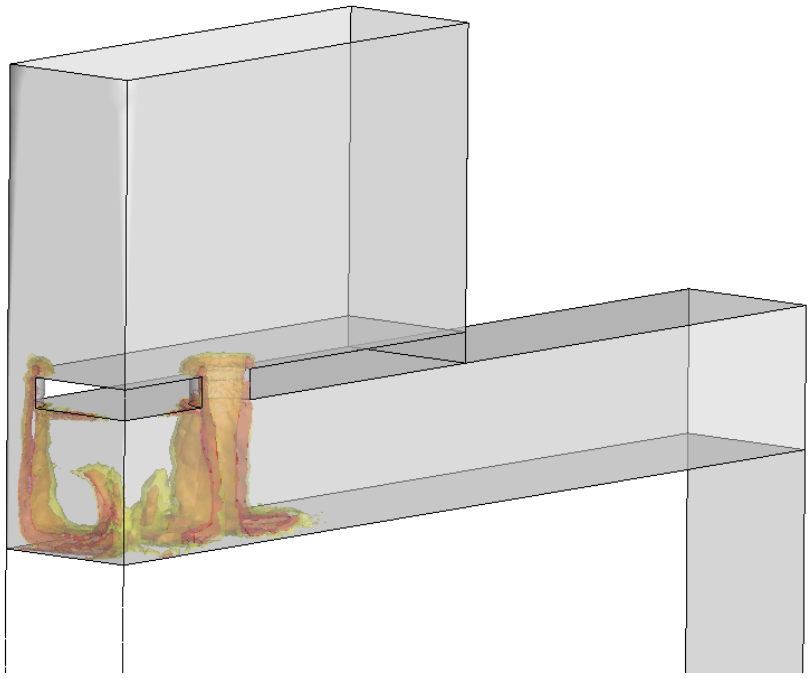

Figure 3.12 – Region of high fluid velocity gradients where Saffman Lift force may influence particle trajectories. Red ≈ 4% relative to drag; Orange ≈ 2.5%; Yellow = 2%.

3.3.4 Thermophoresis

Thermophoresis is the force on the particle in the presence of strong temperature gradients. Hot fluid particles are more energized than colder particles. For small particles on the order of microns or smaller, where the particle size is comparable to the mean free path of the gas, the energized gas particles exert a force on the particle in the direction opposite to the temperature gradient (except in rare cases where the solid particle is smaller than the gas particles, in which case the force is in the opposite direction). This is illustrated in Figure 3.13.

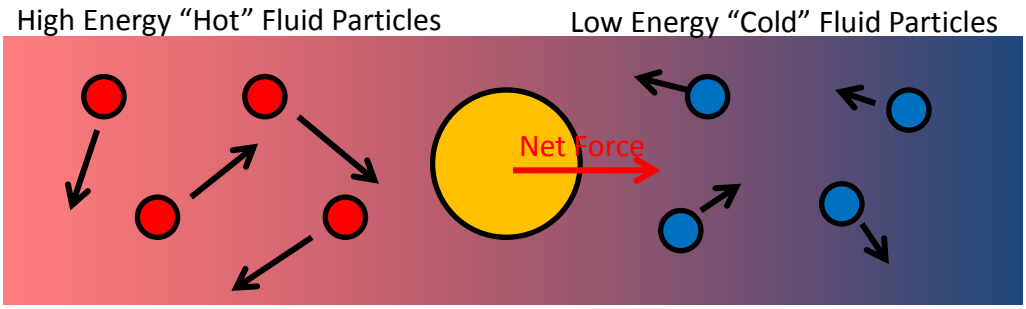

Figure 3.13 – Thermophoresis representation

$$\boldsymbol{F_{Therm} = f\left(Kn, \frac{\partial T}{\partial x}, k_p, k_f, \ldots\right)} \qquad \textbf{[3.11]}$$

Like the Saffman lift, thermophoresis is weak compared to the drag, and is never expected to exceed about 2% of the total force, but is considered strong enough to still be applied. Figure 3.14 shows the temperature gradient field in the flow solution, illustrating locations where thermophoresis may influence particle movement. The location of the highest gradient within the fluid is near the impact plate in the region of the impinging jet. The red regions represent where the thermophoretic force may exceed only 1% of the

typical drag force, showing how the effect of thermophoresis is limited to a very small region within the flow field. The thermophoretic force in this region would (weakly) act to push particles away from the hot surface into the colder flow.

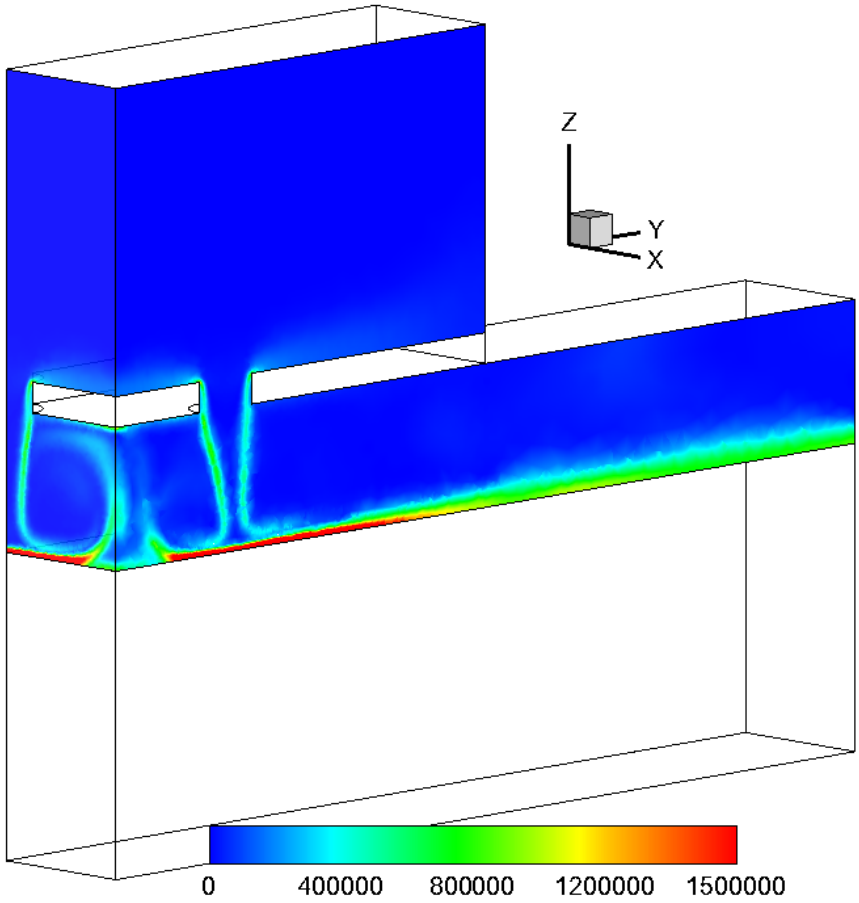

Figure 3.14 – Contours of temperature gradient magnitude [°K/m] showing locations where thermophoresis may influence particle trajectories

Several other forces can affect the trajectory of the particles, but are neglected in this study. Gravity is neglected because the influence of gravity is very small compared to the drag and other forces. For this study the influence of gravity is only about 0.1% that of the drag, even for large particles. For other applications involving larger particles

or much lower velocities, the force of gravity may need to be applied. Other forces, such as Brownian motion, lift due to particle rotation, and electromagnetic forces are neglected.

3.3.5 Thermal modeling of particles

The thermal modeling of particles is required as multiple sticking models are dependent on the temperature of the particle upon impact with a surface. The temperature of the particle is also determined by integrating the heat transfer on the particle over time. Because the particles are very small and have a Biot number much less than unity, the temperature of the particle is assumed to be spatially uniform throughout and a lumped capacitance model is considered valid.

The heat transfer to the particle from convection is approximated using the relation from Ranz and Marshall [46].

$$\boldsymbol{Nu = 2.0 + 0.6 Re_D^{\frac{1}{2}} Pr^{\frac{1}{3}}} \qquad \textbf{[3.12]}$$

The Reynolds number is based on the particle diameter and the relative velocity of the particle with respect to the fluid velocity.

Using this relation, one can estimate the time or distance required for a particle to reach thermal equilibrium with the flow. Figure 3.15 shows an example of several particles of different diameters and the distance required to reach thermal equilibrium, necessary to determine the particle temperatures at the test section for either computational models or experiments. Additionally, the figure shows the comparison of particle tracking using Fluent software's built-in Discrete Phase Module (DPM) and particle tracking performed externally in a Matlab routine created by the author. As expected, the two methods agree perfectly.

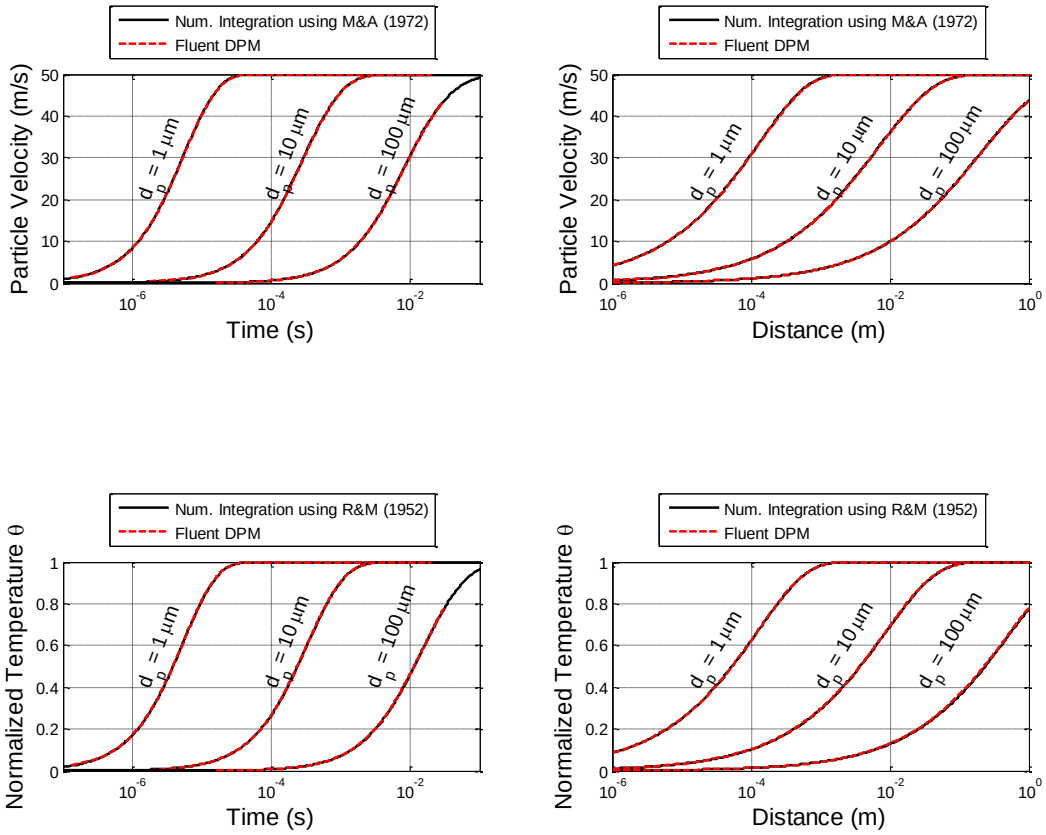

Figure 3.15 – Comparison of Fluent DPM with Runge-Kutta tracking scheme of velocity and temperature.

In this example the particles are injected without any initial velocity and the fluid is moving at a constant 50 m/s, with a 50 °C temperature difference between the two. The distance required for reaching flow and thermal equilibrium (within 1%) is very dependent on the diameter of the particle. While the 1 µm particle reaches both flow and thermal equilibrium in only about 0.5 mm, it takes the 10 µm particle a distance of 50 mm, and the 100 µm particle about 5 m. In this case, the distance required to reach thermal equilibrium is proportional to the square of the particle diameter. From this analysis, it is expected that all particles in the experimental tests will be in thermal and

flow equilibrium approaching the impingement holes. Particles in the computations were initialized in thermal and flow equilibrium with the fluid.

These validation calculations assumed several properties of the fluid and properties. The particles were assumed to be perfect spheres, with

$$\rho_p = 2320\frac{kg}{m^3} \;\; \rho_f = 0.4\frac{kg}{m^3} \;\; k_f = 0.08 \;\; k_p = 0.5 \;\; c_p = 984 \;\; Pr = .71 \;\; \mu_f = 5 \times 10^{-5}$$

3.3.6 Particle Rebounds

When particles impact and do not stick, coefficients of restitutions are applied using trends from Whitaker et al. [47]. Whitaker et al. acquired coefficients of restitution data by impacting quartz particles against flat metal surfaces at multiple angles and velocities. Velocity and restitution data were acquired through the use of a particle shadow velocimetry technique. While the materials and velocities of the particle data were similar to what would be expected in internal deposition applications, the tests were run at ambient temperatures and the particles were considerably larger, on the order of 100 µm.

Normal and tangential coefficients of restitution were determined to be most dependent on incoming particle impact angle. Polynomial curve fits were created for the average restitution coefficients and standard deviations for those curve fits. For each particle impact, the mean coefficient of restitution was calculated and a deviation was applied using the standard deviation and a normalized random number. The restitution trends are given in equations 3.13-16.

$$\boldsymbol{e_N = 2.721 - 0.153\alpha + 3.80 \times 10^{-3}\alpha^2 - 4.25 \times 10^{-5}\alpha^3 + 1.76 \times 10^{-7}\alpha^4} \qquad \textbf{[3.13]}$$

$$\boldsymbol{e_T = 0.572 - 0.00885\alpha + 3.86 \times 10^{-4}\alpha^2 - 1.72 \times 10^{-5}\alpha^3 + 1.47 \times 10^{-7}\alpha^4} \qquad \textbf{[3.14]}$$

$$\sigma_{e_N} = 1.431 - 0.0947\alpha + 2.70 \times 10^{-3}\alpha^2 - 3.34 \times 10^{-5}\alpha^3 + 1.49 \times 10^{-7}\alpha^4 \quad [3.15]$$

$$\sigma_{e_T} = 0.242 - 0.00961\alpha + 5.02 \times 10^{-4}\alpha^2 - 9.52 \times 10^{-6}\alpha^3 + 7.74 \times 10^{-8}\alpha^4 \quad [3.16]$$

For these polynomial functions, α is the incoming impact angle in degrees.

3.4 Particle Sticking

Six particle sticking models were investigated and compared against experimental results, discussed in the following order.

1. Critical viscosity model from [38]

2. Critical velocity model from [38]

Other models generated for this research include the following proposed models

3. Calibrated critical velocity model using experimental data

4. Calibrated critical kinetic energy model using experimental data

5. "Simple" calibrated model using experimental data applied with geometry adaptation

6. Shear-based sticking model

These models are evaluated for adequacy for internal deposition applications, and strengths and weaknesses are discussed within the results section.

3.5 Grid Adaptation

For a single iteration, the deposition model predicts a deposit rate on the surfaces of a computational geometry. After the deposition model is run by tracking a large number of particles, the deposit locations and particle size statistics are collected. The surface is discretized into a rectangular mesh for 3D simulations (not necessarily the same as the CFD mesh, but on the same order of grid spacing) or along the linear wall mesh for 2D simulations. The number of deposits occurring within each surface cell is

counted, analogous to a multi-dimensional histogram. The particulate volume is calculated from the particle sizes, resulting in a total volumetric growth in each surface cell, which is then divided by an assumed porosity factor of 0.5. This deposit growth rate is multiplied by a time step factor to acquire the total mass of particulate injected relative to the amount actually tracked. By multiplying the rate by a time step, a deposit thickness is acquired. This thickness is used to modify the geometry for the next iteration of the computational model.

For two-dimensional simulations, the deposit layer is not modeled directly (meshed) as only the fluid zone is modeled. The mesh is structured, allowing for more direct manipulation. The mesh is not recreated, but rather the original is simply stretched to account for the deposit buildup, as illustrated in Figure 3.16.

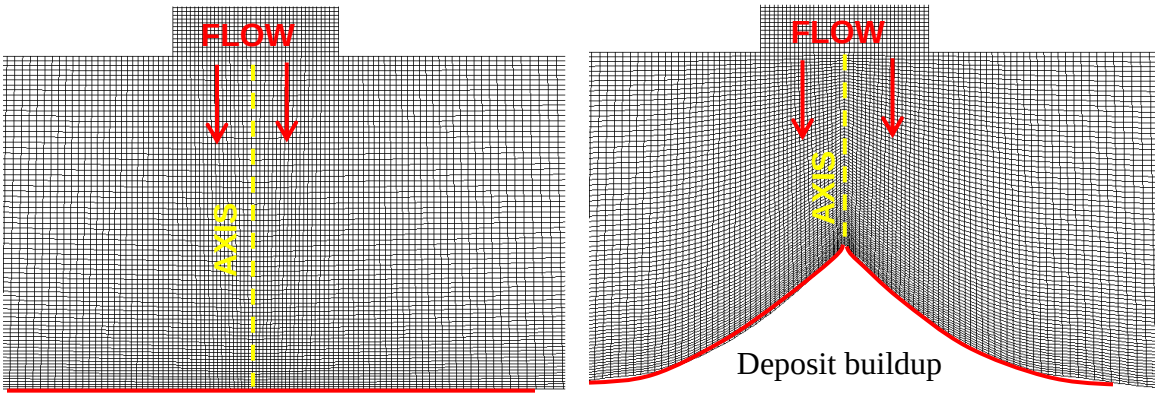

Figure 3.16 – Representation of two-dimensional mesh (left) before and (after) grid adaptation due to deposit buildup

For three-dimensional, unstructured meshes, the process is slightly different. The deposition rates are acquired through the deposition model, and multiplied by a time step to acquire a change in deposit volume and thickness. The surface cells are normally extruded to the deposit thickness distance with corrections applied due to the curvature of the surface. This correction in thickness is applied because the surface cell area, after the extrusion, grows if the surface is convex and shrinks if the surface is concave. The correction ensures that the change in total volume to each cell is equal to the volume predicted by the deposition model. This is illustrated in a simplified schematic in Figure 3.17. The time step, or change in thickness per iteration, was kept sufficiently small so that no extruded cells came close to overlapping one another in regions where the surface was concave. Otherwise this would create inaccuracies and singularities in the surface mesh [28]. The extruded surface is calculated and saved as an STL file through a Matlab routine.

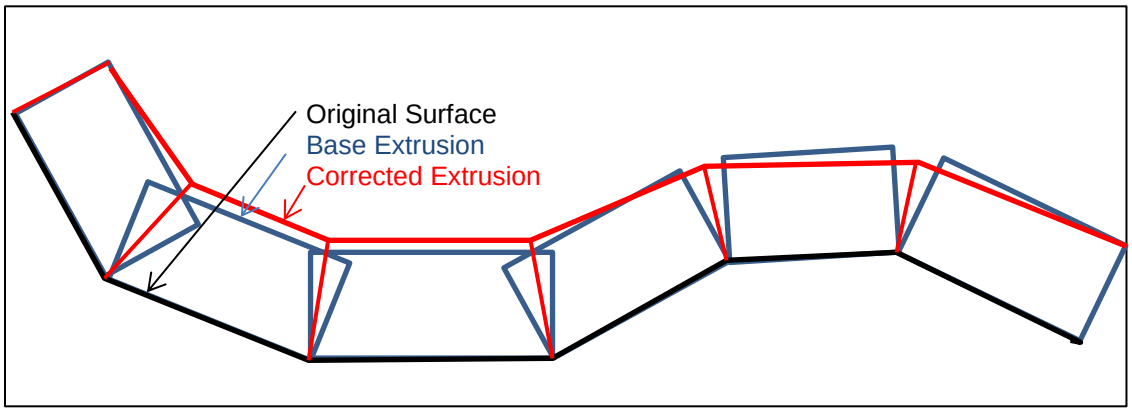

Figure 3.17 – Schematic showing grid adaptation by cell extrusion

The STL surface is imported into the grid generation software Gridgen. The old grid is recreated to account for the new surface. It should be noted that these regions of the grid are not merely stretched, but recreated and may result in slightly fewer or greater cells than the previous grid. The node spacing along the surfaces, however, is kept constant. This process is illustrated in Figure 3.18.

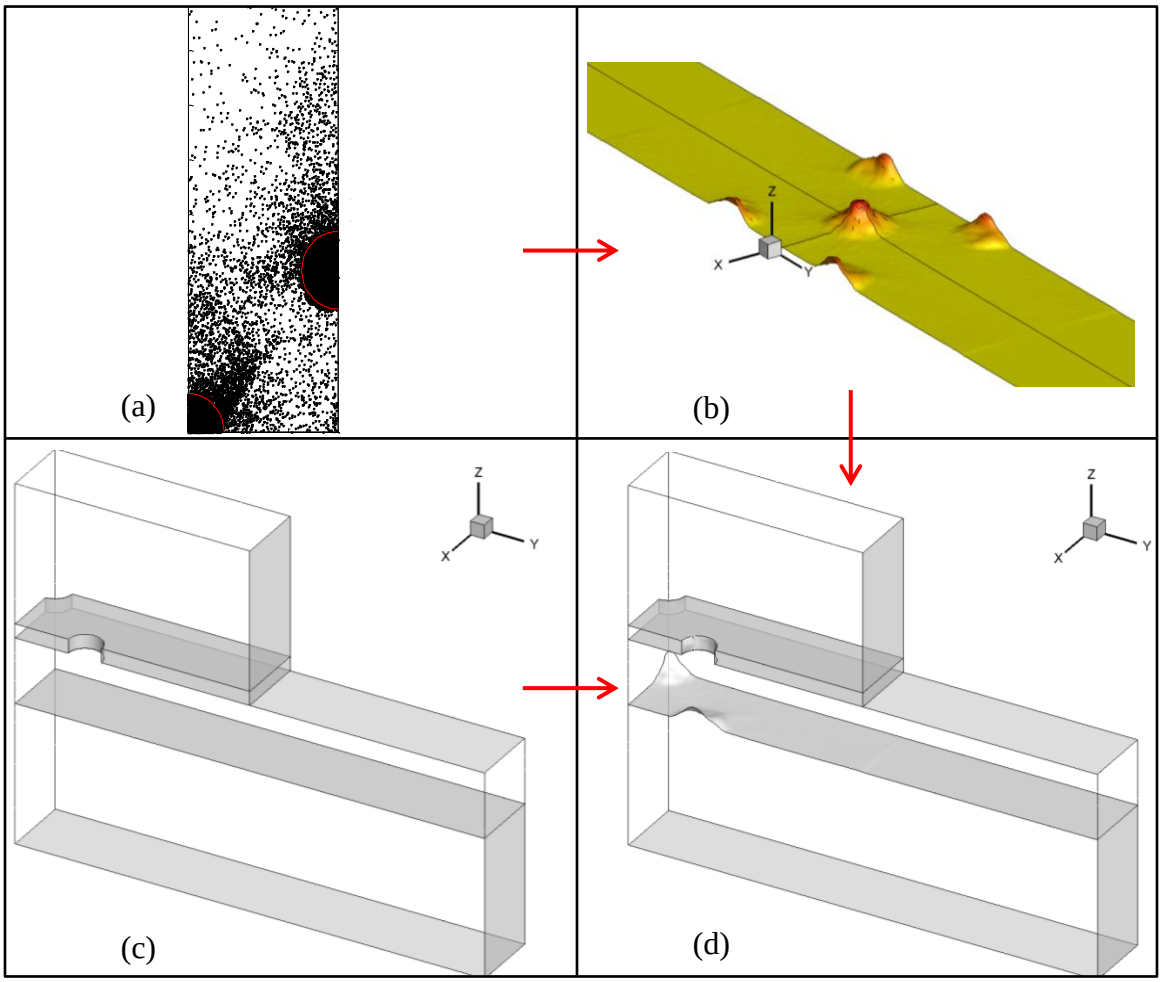

Figure 3.18 – Illustration of grid adaptation from deposit growth. (a) Particle sticks located and counted, (b) translated into new deposit growth surface, applied to (c) base geometry to (d) create new geometry.

This grid adaptation technique involves smoothing at certain steps. Smoothing automatically occurs when transforming discrete deposition locations into surface deposition rates. As the unstructured grid is created using the generated STL surface in the grid generation software, cell faces may not align perfectly with the surface faces, which results in further smoothing in the CFD grid by linear interpolation.

3.6 Solid Material Modeling

The grid generation of the deposit layer can be problematic in regions where the deposit layer is very thin or non-existent. This was initially corrected by imposing a thin layer of deposit over the entire plate surface, so any miniscule changes or growth would not create overly skewed cells. This is also problematic as even a thin layer of deposit may unrealistically affect the heat transfer through the plate. This is due to differences in thermal conductivity separated by almost two orders of magnitude.

This was corrected by defining a single solid zone mesh, and defining the properties of the material based on the spatial location. A User Defined Function (UDF) was written that defined any solid cells located above the horizontal surface of the plate, where the surface has grown due to deposit growth, to have thermal and material properties of the deposit. The grid was also refined in the region of the interface, allowing for easier grid generation and flow convergence. The UDF also defined the material properties of the perforated impingement plate, as illustrated in Figure 3.19.

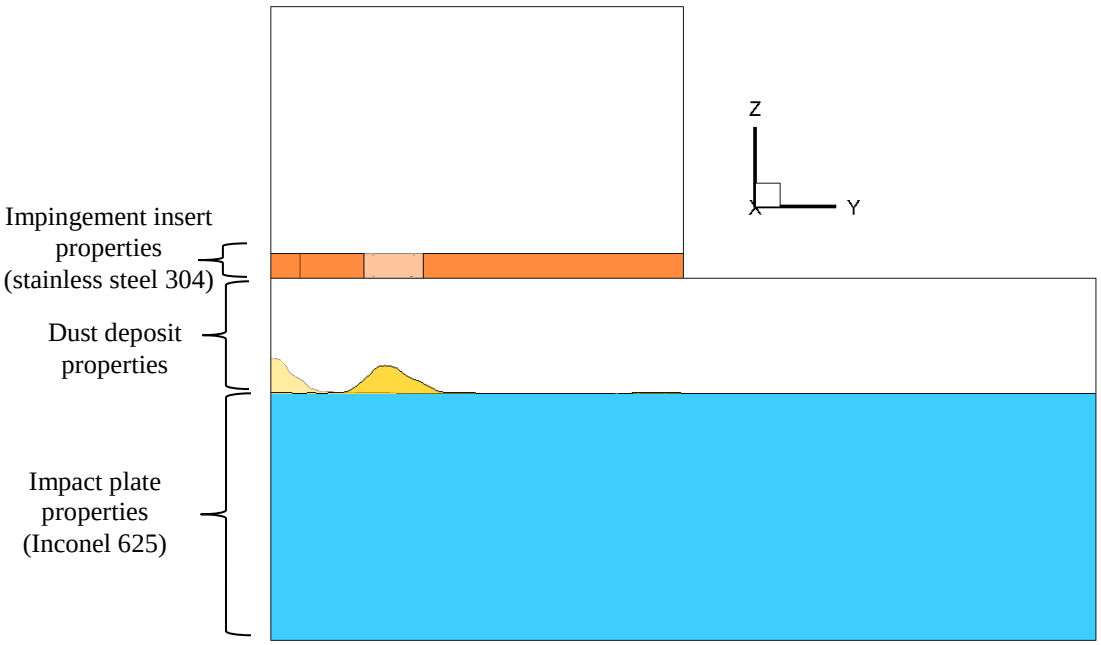

Figure 3.19 – Illustration of solid material modeling

Chapter 4. Experimental Results

Several tests were performed to determine the factors that contribute the most to particle deposition in internal cavities. Figure 4.1 shows a post-test photograph of the deposit-filled plate from test 18a, qualitatively similar to most tests performed. For this test, the flow rate was 4.6×10^{-4} kg/s at a temperature of 1000 °F (540 °C), corresponding to a Reynolds number of about 1000. The impact plate was flame heated from the back side. These test conditions are expected to be the most relevant to actual engine conditions.

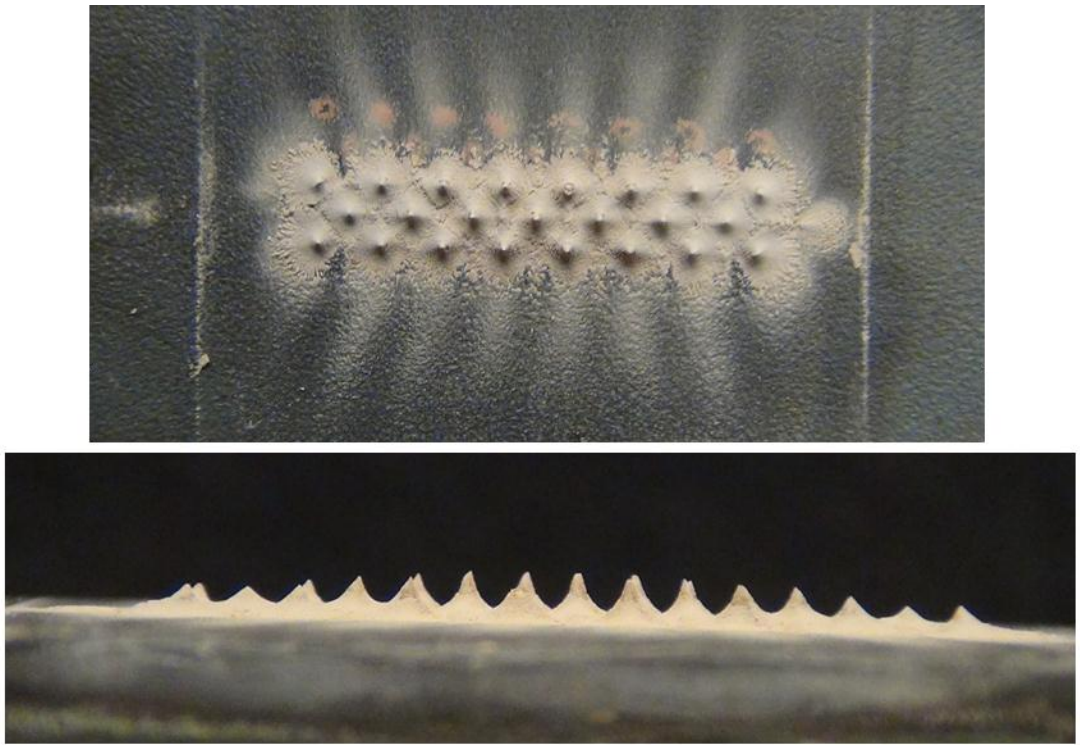

Figure 4.1 – Photograph of impact plate after deposition test from test 18a at high temperature and flame heating. (top) Top view showing the locations of deposit on plate (x-y plane) and (bottom) side view showing deposit thicknesses and structures (x-z plane).

The deposit dust completely covered the plate in the region of impingement holes, and easily visible cones match the impingement jet pattern. Very little deposit occurs far from the impinging jets, though faint deposit streaks are seen in Figure 4.1 representing the path of the exhausting flow. Prior to measuring the deposit on the impact plate, digital scans were taken of the deposit-laden surface, shown in Figure 4.2.

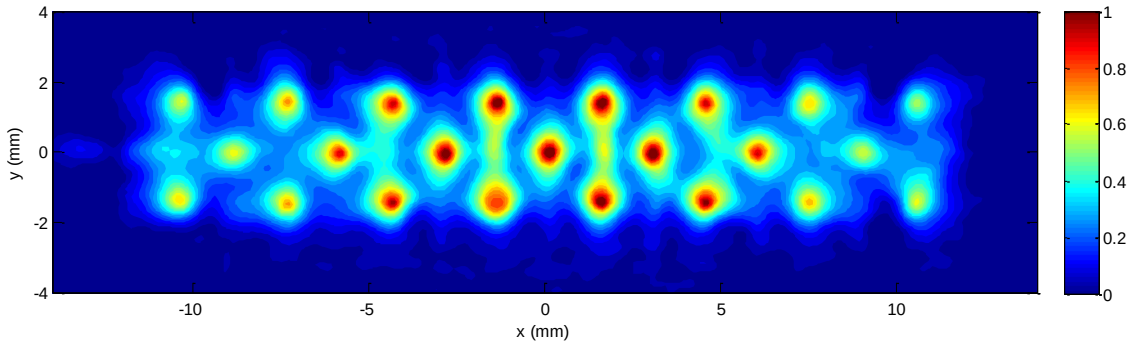

Figure 4.2 – Deposit thickness [mm] on impact plate from test 18a (high temperature, flame heating).

This scan of the deposit was taken to get a quantitative assessment of the deposit structure, and the surface clearly shows the presence and locations of the deposit cones. From these scans linear traces were acquired to ascertain the similarity of the deposit structures among the three rows of holes.

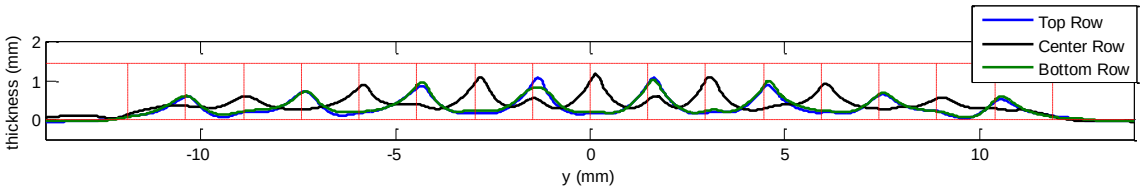

Figure 4.3 – Deposit traces along impingement hole centers from post-test scan for test 18a (high temperature, flame heating).

The red lines in Figure 4.3 correspond to the impingement hole center locations and plate locations. The lower and upper row of cones can be compared directly, and the scan shows strong similarity between the two. Likewise, the deposit cones on the center row are similar in size and shape to those on the outer rows. For the centermost deposit cones, the three center cones for the center row and the four center cones for the outer rows, the cones show uniformity from one to the next. The deposit cones on the left-most and right-most ends of the rows are much smaller in this test, and may be due to lack of periodicity from the edges of the impingement hole rows. The peaks of the tallest cones nearly span the entire gap.

A major distinction between the deposit from these experimental tests and those performed at higher temperatures for external applications is the lack of chemical change. For external studies in [48]-[51], the deposit is discolored through chemical reactions. The deposit forms as bulk conglomerates where individual particles are sintered or melted together, and cannot be reground into its prior state, In the experimental tests in the studies of this paper, the deposit material shows little to no distinction in appearance compared to the dust that is fed into the system. The deposits, upon removal, easily revert to their powder form. This indicates that temperatures of 1000 °F (540 °C) are too low to cause any sintering of particles of this composition.

4.1 Experimental Capture Efficiencies

After each experimental test, the deposit was removed and the accumulated mass was measured. The results from the exploratory tests are given in Table 4.1. The capture efficiencies presented indicate the measured deposit only on the impact plate, as deposit on the upstream or downstream portions on the impingement plate were generally negligible unless otherwise noted.

Table 4.1 – Capture efficiencies on impact plate for 2.0 g injected experimental tests

Air Flow Rate / Flow Temperature	$\dot{m} = 2.3 \times 10^{-4} kg/s$ $Re_D \sim 500$		$\dot{m} = 4.6 \times 10^{-4} kg/s$ $Re_D \sim 1000$		$\dot{m} = 6.9 \times 10^{-4} kg/s$ $Re_D \sim 1500$	
	Unheated Plate	Heated Plate	Unheated Plate	Heated Plate	Unheated Plate	Heated Plate
70 °F (20 °C)			1.58% 1.19% small 2.71% very small			
700 °F (370 °C)	**0.65%**	**0.59%**	0.87%	1.36%	0.78%	1.02%
1000 °F (540 °C)	**0.94%**	**0.85%**	**0.69%**	**1.48%**	**0.19%**	**1.06%**

These results are all from non-repeated tests, and therefore don't give a measure of natural variation. Additionally, for many of these tests, the capture efficiency may not be a valid measurement because the flow field was severely altered during the test. In Table 4.1, the capture efficiencies that are bolded in blue indicate that deposit cones grew so tall as to fill the entire gap and penetrate the perforated impingement sheet. In these cases, the peaks of the cones were broken during post-test disassembly and the measured capture efficiencies may be undervalued. Consequently, all these cases show where deposit grew to heights at or exceeding the gap spacing, even though the measured

capture efficiencies may be lower than other cases where the deposit cones were shorter. These cases all occur for the low Re_D cases at both intermediate and high temperatures, and for intermediate Re_D at high temperatures. Two tests are identified in Table 4.1 by being bolded in red, at the two high Re_D and high temperature cases. These tests experienced repeated large-scale deposit removal. Video showed that in these cases, entire deposit structures were broken off during testing, leaving only fragments or clean surfaces. These anomalies necessitated other tests run with less total injected particulate, in order to acquire capture efficiencies that aren't corrupted by clogged impingement holes in the low flow rate or high temperature cases, or lost deposit in the high flow rate cases. These new tests were all repeated three times in order to more conclusively verify any trends. Only certain test conditions were repeated to preserve functionality of the experimental facility, as the test section and heating system degrade during high temperature or flame heated tests.

Table 4.2 – Averaged Capture Efficiencies for 1.0 g injected experimental tests

Air Flow Rate / Flow Temperature	$\dot{m} = \times 10^{-4}\, kg/s$ $Re_D \sim 500$	$\dot{m} = 4.6 \times 10^{-4}\, kg/s$ $Re_D \sim 1000$		$\dot{m} = 6.9 \times 10^{-4}\, kg/s$ $Re_D \sim 1500$
	Unheated Plate	Unheated Plate	Heated Plate	Unheated Plate
70 °F (20 °C)	-	0.56 ± 0.10%	-	-
400 °F (205 °C)	-	0.50 ± 0.03%	-	-
700 °F (370 °C)	0.71 ± 0.14%	0.45 ± 0.15%	-	0.14 ± 0.04%
1000 °F (540 °C)	-	1.04 ± 0.21%	1.90 ± 0.42%	-

Table 2.3 shows the averaged capture efficiencies from the repeated experimental tests with 95% confidence bounds. By comparing the second set of tests with the first set, it is immediately apparent that, generally speaking, the capture efficiencies are lower when the amount of injected particulate is reduced from 2.0 g to 1.0. This is due to two likely reasons. Previous research suggests that the particle sticking efficiency increases over time, in that particles impacting a pre-existing layer of particles are more likely to stick compared to impacting a flat wall [11][52]. It is therefore expected that the second gram of injected dust will deposit at a higher rate than the first. The second reason is due to limitations in the facility. It was observed that, despite the design considerations of the dispersion tube and heating section, particulate matter did accumulate inside any crevasses of the facility and as thin layers on some of the walls. It is therefore expected that not all particulate matter passed through the test section. Unfortunately it was not possible to measure the amount that remained in the facility, and this is a source of error in the capture efficiency measurements. However, efforts were made to reduce this error by partially cleaning out the facility between tests in a consistent manner. It was cleaned by passing high flow rates of ambient air (four times the intermediate rate in the experiments) through the facility without the test piece installed. This high flow swept the internal flow path of the facility, so that each test was initiated under the same conditions. If it were possible to ensure that all injected feed dust were able to make it to the test section, without any dust accumulation inside of the facility, the capture efficiencies would be expected to be larger, though the trends are not expected to change.

The results show a surprising lack of influence of temperature (Tests 14-17). With external deposition, a difference in temperature of 100 °C could change deposition rates

by an order of magnitude. Indeed, the critical viscosity sticking model predicts an order of magnitude sticking reduction with approximately every 100 °C of temperature change below the critical sticking temperature. Alternatively, the capture efficiencies for the various operating conditions generally ranged from 0.5% to 1.0% despite spanning about 500 °C of temperature. Additionally, the change only occurs from 700 °F to 1000 °F, with capture efficiencies of all lower temperatures being relatively constant at the intermediate flow rate. This is in agreement with Clum [53] who ran similar experiments in the same facility. He found that for the same dust composition, the capture efficiency changed little from ambient temperatures to 700 °F, but increased by about a factor of two at 1000 °F. The repeated tests with the heated impact plate also showed a significant increase in capture efficiency, by almost a factor of two compared to the unheated case.

The flow rates also proved to have a significant impact on particle deposition. Capture efficiencies decreased in a nearly linear fashion across the same flow rates for the same flow temperature. This is fascinating in that it is the first trend that runs counter to external deposition results. For external deposition, higher flow rates correspond to higher Stokes numbers, and higher Stokes numbers correspond to higher rates of deposition. In these tests, however, lower Stokes numbers correspond to higher deposit rates. This also agrees with the sticking criteria discussed by Brach et al. [22], in that particles impacting at lower velocities have higher probabilities of sticking.

Not all deposit formations formed in the same manner, as individual cones associated with each impingement jet. The lower temperature and higher flow rate tests resulted in deposit ridges positioned between adjacent cones. These ridges were occasionally larger in height than the deposit cones. A photograph of the post-test impact

plate of test 14a (intermediate flow rate, ambient temperature) is shown in Figure 4.4 and the optical scan in Figure 4.5.

Figure 4.4 – Photograph of post-test impact plate from test 14a at intermediate flow rate and ambient temperature.

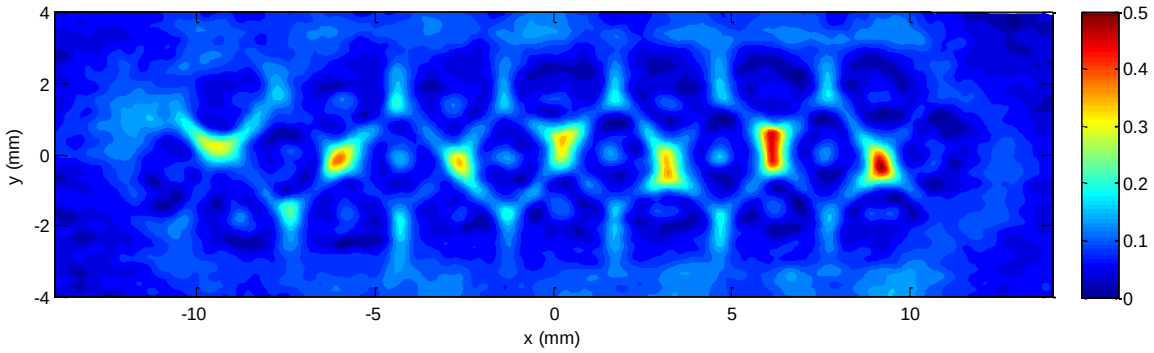

Figure 4.5 – Optical scan of impact plate from test 14a at intermediate flow rate and ambient temperature.

The ridges bear resemblance to the results from [36] and [37], where deposit accumulated generally not as mounds but rather as sectioning lines dividing the impingement jet regions. Figure 4.5 shows that the ridges in between the cones, specifically the midpoint of four adjacent holes (red and yellow regions in figure), are the

location of maximum deposit growth. Interestingly, this represents the point furthest from the impinging jet center within the array.

4.2 Video Showing Transient buildup

The test section was designed to allow for optical access. Video recording for various tests captured the transient nature of the deposit buildup. Figure 4.7 shows screenshots from various times during test 18a (intermediate flow rate, high temperature, and flame wall heating). The orientation of the image is looking through the gap between the perforated impingement insert on top and the impact plate on the bottom. Consequently, the particle-laden fluid jets impact from top to bottom, and a majority of the deposit accumulates on the lower impact plate. Because the images are in-plane with the plates, the impingement holes are not visible and the deposit shown as dark cones is a projection of the three rows of deposit. The cones of the outer rows are aligned, so the back row of deposit is obstructed by the front row. Likewise, as the deposit structures become large, the front row of deposit also obstructs the center row, as illustrated in Figure 4.6.

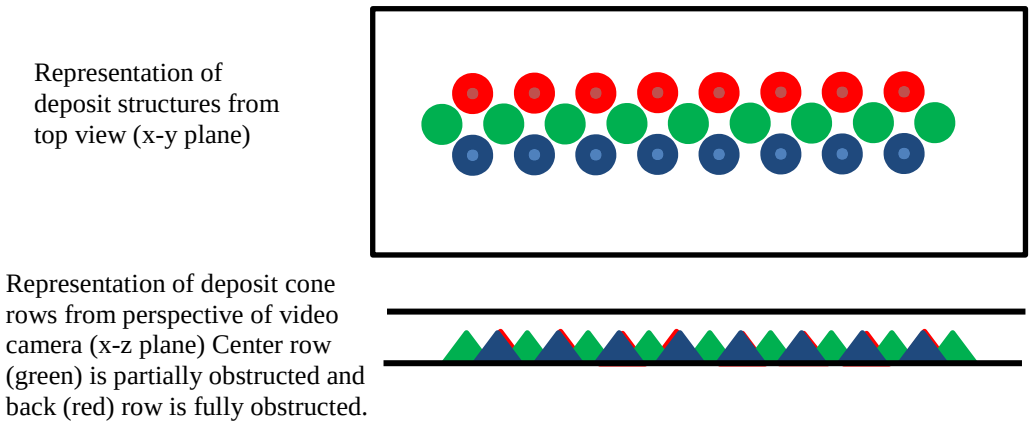

Figure 4.6 – Diagram showing how deposit cones are viewed from perspective of video camera

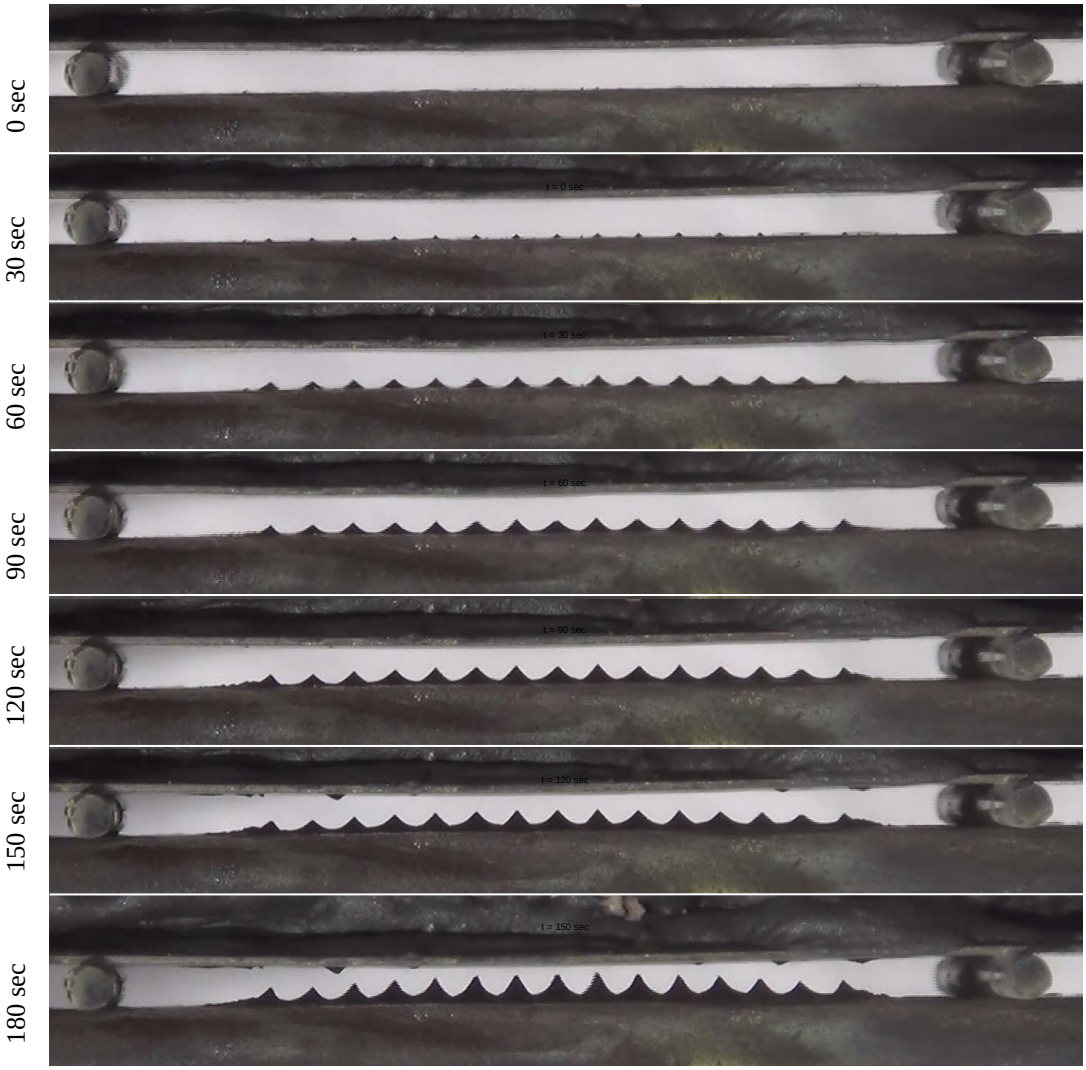

Figure 4.7 – Video images from experiment 18a (high temperature, flame heating).

The video recordings were used to monitor transient buildup during the test in order to compare with computational results. This was done through a processing routine in Matlab to extract the projection of the deposit growth. While these images can only detect growth in two spatial dimensions (x and z), the cones are generally axisymmetric and can be assumed to grow accordingly. Figure 4.8 shows the average growth of the

three center cones along the center row. Each line represents approximately 0.1 grams of dust injected into the system.

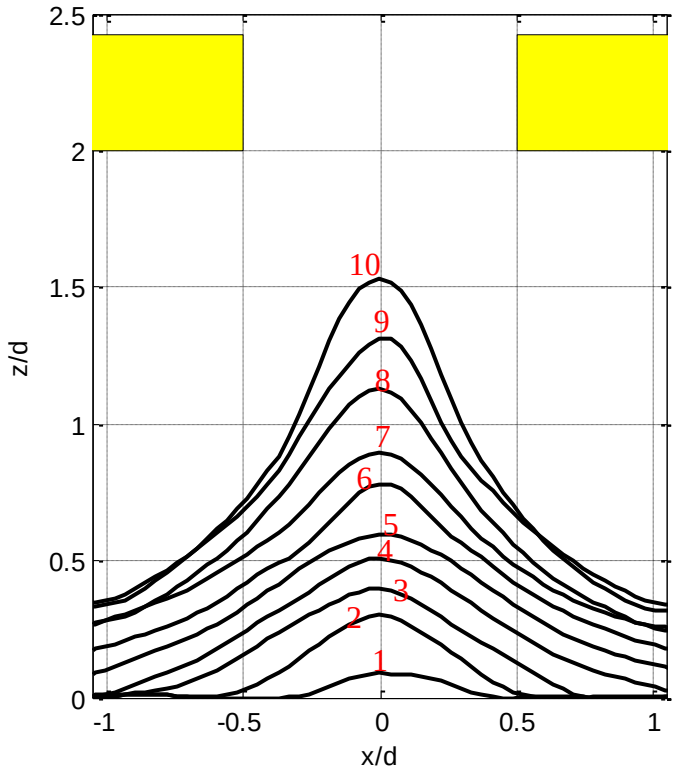

Figure 4.8 – Growth of deposit from video. Each line represents the addition of approximately 0.1 g of particulate.

This figure provides critical information regarding the transient nature of the deposit buildup. The deposit growth occurs in several distinct phases. Initially, the deposit growth is restricted in area to low radial positions relative to the jet center, occurring for lines 1-2 in the figure. From lines 2-6, the cone grows with a relatively constant angle, growing upward and outward. From lines 6-10, growth occurs

predominantly at low radial positions and the cone peak growth rate accelerates upward toward the impingement hole.

Some videos clearly show deposit structures that grew into the impingement holes. Test 8 shows this most distinctly, depicted in Figure 4.9.

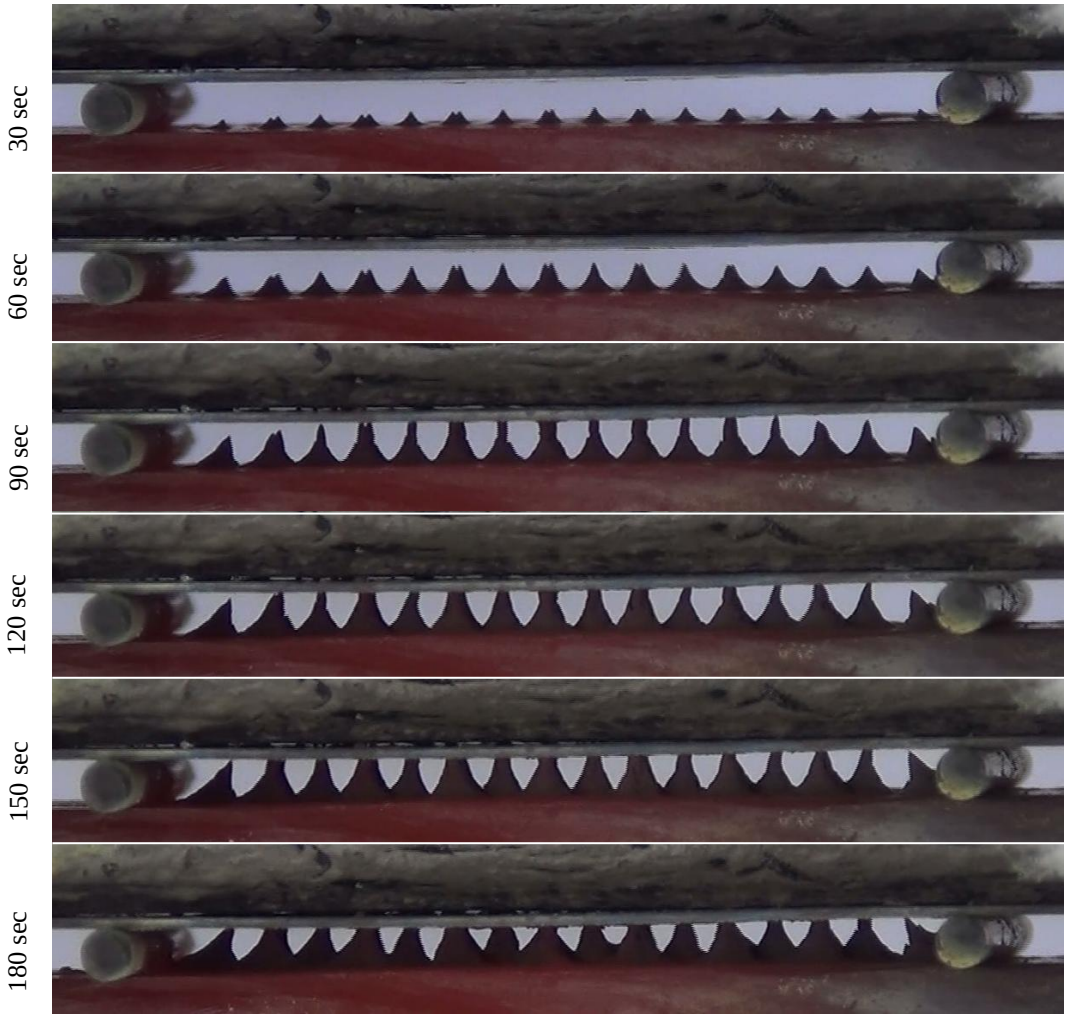

Figure 4.9 – Video frames from test 8 (low flow rate, high temperature, with flame heating) showing cones penetrating impingement holes.

This video reveals fast growing, steep deposit cones easily span the entire gap. As the cones grow into the impingement holes, flow is obstructed by the presence of the deposition. Because mass flow is held constant, flow through the various holes may become non-uniform, as flow may be rerouted from restricted impingement holes to non-restricted holes at the ends of the rows where deposit cones are smaller.

The cone structure is dependent upon the fluid temperature and flow rates. All experiments at low flow rates (Re~500) with 2.0 g of injected dust experienced these larger deposit formations that fill the entire gap, and the high-temperature, medium flow rates see these formations when 2.0 grams of dust are injected. Tests 18a-c experienced deposit cones almost reaching the impingement holes, and this would have been expected had 2.0g been injected instead of 1.0g (see Figure 4.3).

For the tests that see tall cones, the peaks of the cones were broken during disassembly, so scans of these tests are incomplete. When possible, broken cones were collected and included in the capture efficiency measurements.

4.2.1 Shearing of Deposit Structures

For the two high Re_D cases at high temperature, (red bolded values in Table 4.1), the tests experienced repeated large-scale deposit removal. Video showed that in these cases, entire deposit structures could be broken off leaving only fragments or clean surfaces. These occurred only for tests at high Re_D with large impingement velocities, signifying that the particulate removal is predominantly due to shear. This is shown in Figure 4.10, showing video images of test 11 (high temperature, high flow rate) at different time steps. Red markings on the image point to deposit structures that are removed between frames.

Interestingly, deposit on the downstream surface of the impingement plate continued to grow without any removal. The capture efficiency on this section was larger than most other tests (little or no deposit generally formed on the upstream or downstream portions of the impingement plate). This is at least in part due to the fact that when the impact plate cones were removed, the particulate matter was entrained again into the flow. The flow then transported the particulate to the fountain region (refer to Figure 1.4), and then to the impingement plate, where it had potential to stick.

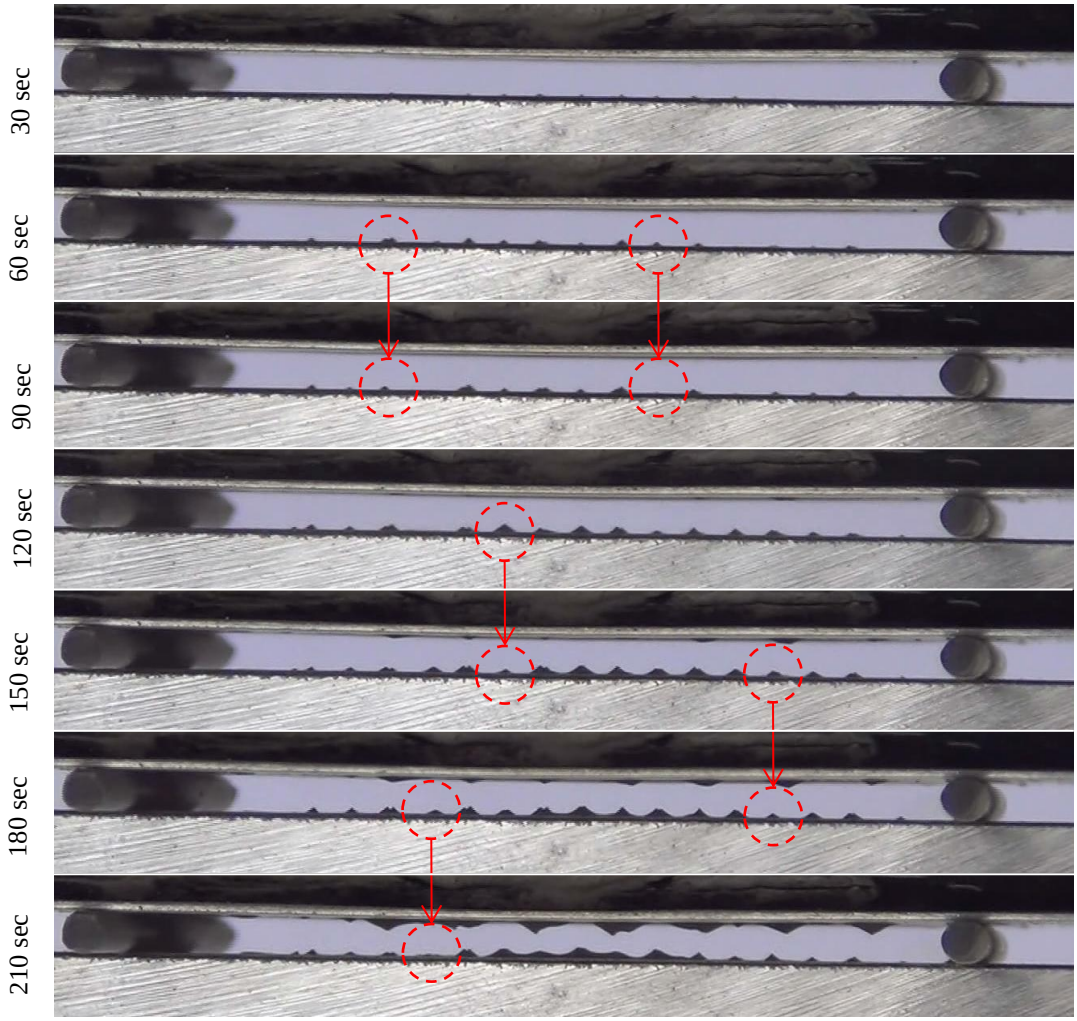

Figure 4.10 - Video frames from test 11 (high temperature, high flow rate) showing deposit structures that are removed during testing.

4.3 TuRFR Validation Test

An experimental test was conducted in the TuRFR utilizing two cylinders with double-wall cooling, simulating the cooling on a nozzle guide vane leading edge. The test allowed for the presence of hot external flow at temperatures of 1950 °F. The internal cooling flow was supplied with a temperature measured at 300 °F and the flow rate through the impingement holes was equal to the intermediate flow rates of the previously discussed experiments. The hole size and spacing matched all other experiments. This test was conducted to validate the simplified test section as representative of actual nozzle guide vanes, and ensure that the presence of film holes, external hot flow, or curved internal walls did not significantly affect the formation of deposit structures.

Like the TuRFR test with the NGVs in section 2.1, the inability to access or measure the internal deposits prevented a direct, quantitative comparison. However, the cylinder was fabricated to allow for removal of the impingement insert without destruction to the deposit structures. Despite the inability to measure the structures directly, the formation of individual cones, seen in the photograph of Figure 4.11, serves as qualitative validation of the deposit growth structures in the simplified test section. Like the results in section 2.1, the deposit forms as cones relative to the impingement hole locations, relatively unaffected by the external flow or film holes on the cylinder wall. Because of the similarity of the deposit formations with both the simplified test section experiments and nozzle guide vane experiments (Figure 2.2), it was determined that the simplified test section captures the dominant sources of deposition in the internal cavities of nozzle guide vanes.

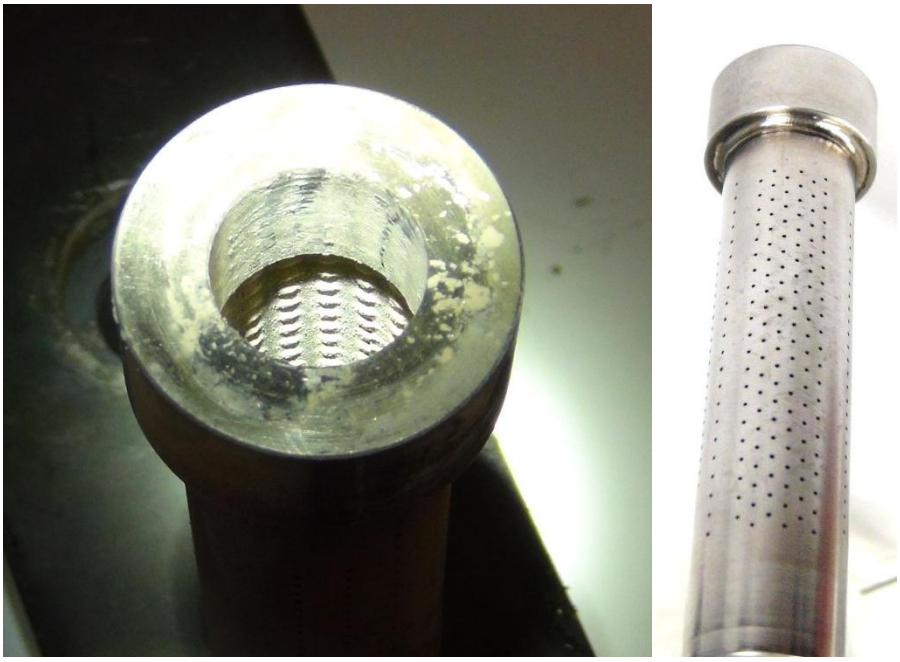

Figure 4.11 – Photograph of cylinder used in TuRFR deposition test (left – post-test viewing internal wall; right – clean cylinder prior to test). Deposit cones seen on internal side of wall with impingement insert removed.

4.4 Chapter Summary

The principle purpose of the experimental tests was to provide a baseline solution for comparison to the computational model. While more could be investigated regarding the results from individual tests, the following conclusions are applicable to the computational modeling.

- Deposit forms principally as cones on the impact plate, located in line with individual impingement jets.
- Deposit rates increase with increasing temperature above 700 °F, though only by about a factor of two between 700 °F and 1000 °F. Rates also increase when the impact plate is heated.
- Deposit rates increase with decreasing flow rates.

- At low temperatures and high flow rates, deposit forms not only as individual cones, but also as deposit ridges at the mid-plane between adjacent jets.
- Deposit cones do not form at constant rates. In the case of Figure 4.8, initial growth is restricted to low radial positions, and then grows both upward and outward with a generally uniform cone slope. At a certain point in height, growth at the peak is accelerated and confined to low radial positions.

Chapter 5. Computational Results

5.1 Results from Initial Flow Solution

The flow solution on the three-dimensional validation geometry was converged as discussed in the methods section (3.2). Flow conditions are also listed in Appendix A for all simulations. The flow field contained all of the features expected from an impingement jet array, including the free jet region, stagnation region, wall jets, and fountain region. Figure 5.1 shows contours of velocity at the x-z plane for the center jet holes.

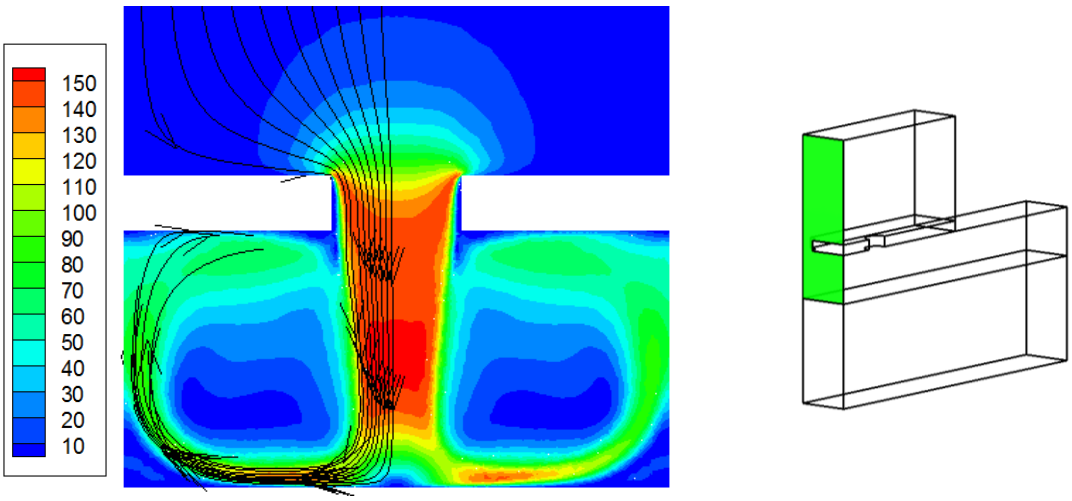

Figure 5.1 – Flow velocity magnitude (m/s) of 3D validation geometry of x-z planes at y = 0

5.1.1 Particle Tracking

Before any sticking model was applied, particles of varied sizes were tracked to determine locations where particles are likely to impact. Every time a particle impacted a solid surface, the location, impact velocities, and particle and surface temperatures were recorded. This preliminary simulation computed the impact efficiency for each size for the given geometry and operating conditions.

The results of these simulations are shown in Figure 5.2, showing a single point for each particle impact on the impact plate from the CFD geometry. For reference, the size and locations of the impingement holes are shown by the red arcs. The simulations allow for multiple rebounds and impacts, utilizing the coefficients of restitution previously discussed. For each particle size, 10,000 particles were tracked, initially distributed evenly at the CFD inlet plane.

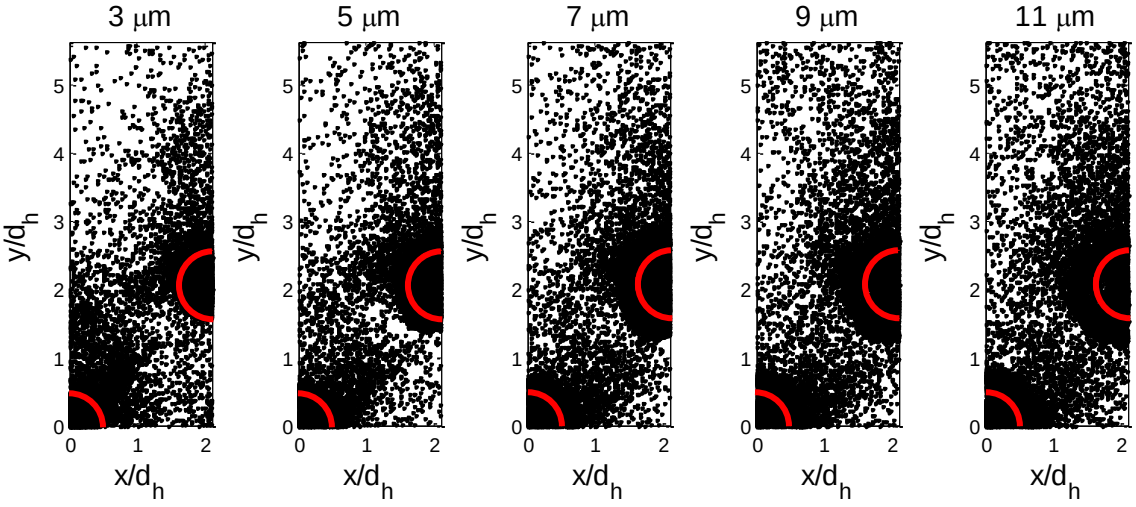

Figure 5.2 – Initial particle impact locations without deposit

These impact location results agree well with the deposit locations in the experiments. Even though no sticking model or geometry adaptation was applied, it was confirmed that a majority of the particle impacts on the plate do occur where the deposit cones form. In this sense the flow solution and particle tracking alone can be used to predict deposit locations, though they cannot predict the rate of growth. Additionally, there is no evidence of deposit growth in the patterns seen in Figure 4.5, where deposit forms as ridges between impinging jets.

5.2 Aerodynamic Focusing of Particles

Particles were also tracked investigating the particle trajectories through the impingement orifice holes, ignoring subsequent impacts and without pre-existing deposit. Figure 5.2 suggests that larger particles impact a larger area relative to the orifice hole diameter, and it was desired to know how the trajectories are influenced by the orifice and particle size.

Particles of 4, 6, 8, 10, and 12 μm diameters were tracked. Figure 5.3 and Figure 5.4 show the particle flux through multiple z-planes for each hole of the CFD geometry. The particle flux is shown as a relative particle flux at a radial position from the orifice hole diameter.

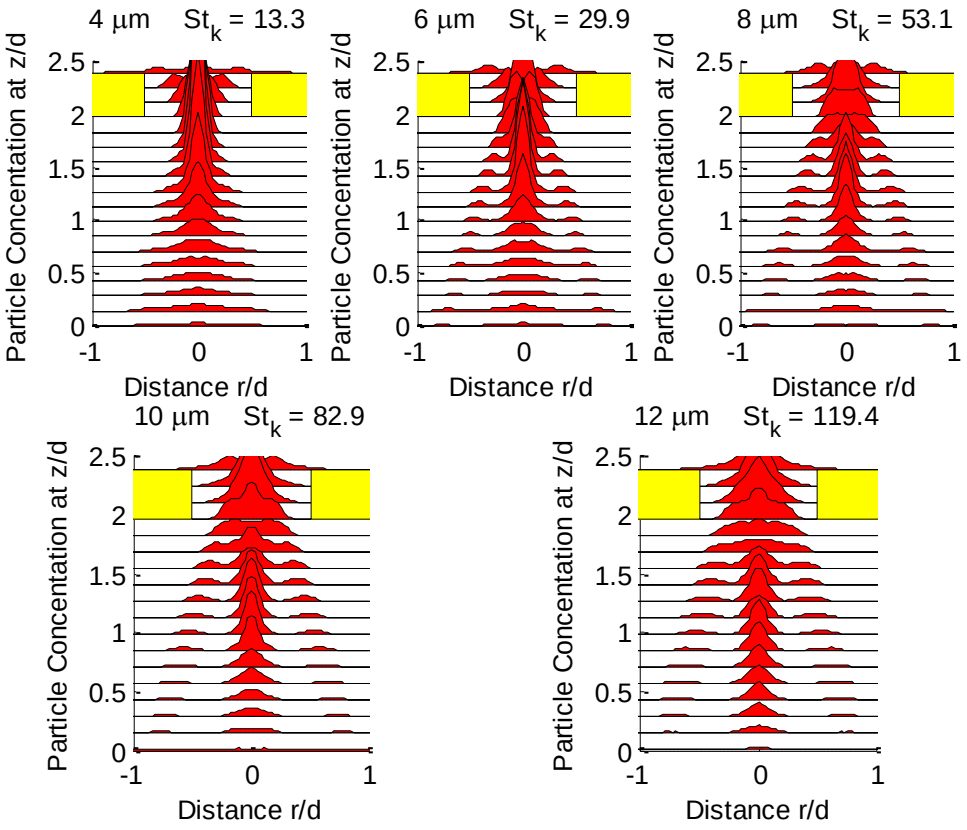

Figure 5.3 - Particle flux histograms at multiple Z-planes for quarter hole of CFD geometry, representing center row of impingement holes.

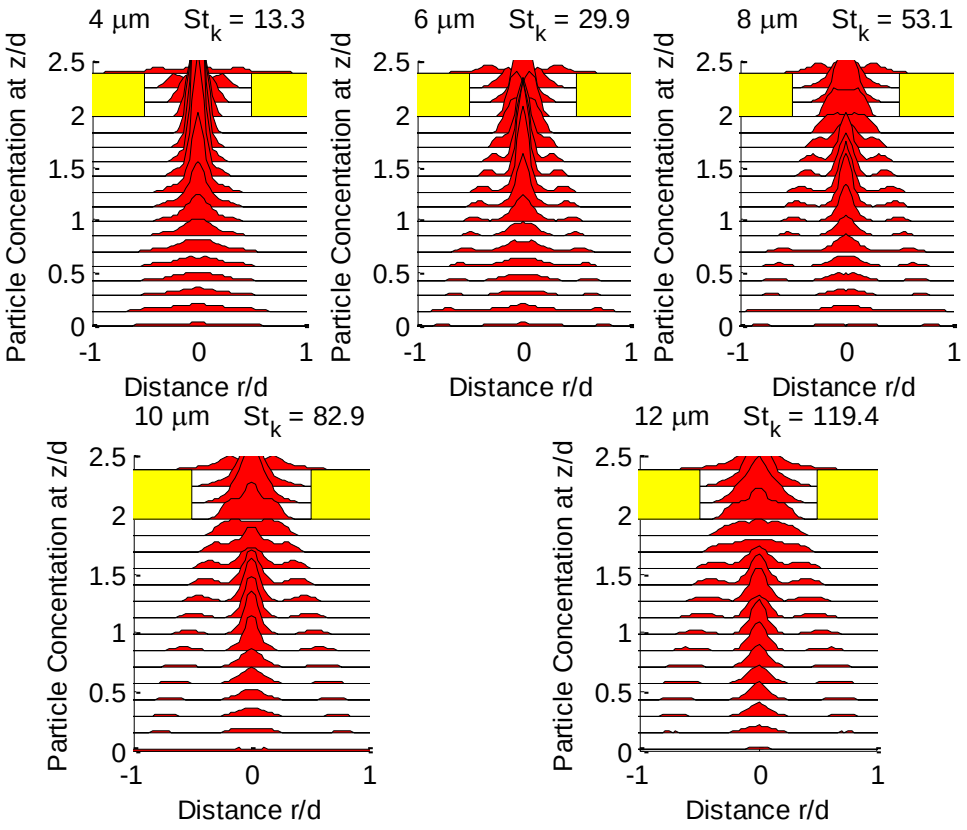

Figure 5.4 - Particle flux histograms at multiple Z-planes for half hole of CFD geometry, representing outer rows of impingement holes.

The particle flux histograms show no significant difference between the two holes in the CFD geometry. The larger particles spread more than the smaller particles, with the 12 µm particles impacting a region about twice the diameter as the orifice hole. Particle flux is much more focused near the exit plane of the orifice hole, with 4 µm particles focused to a jet diameter about one third of the orifice diameter, immediately downstream of the orifice exit. While these trajectories were performed on a clean geometry without deposit, this focusing suggests that as the deposit cones grow toward the impingement hole, the particle impact density will increase leading to much faster deposit growth in an

even smaller impact radius, as was seen in the experimental videos (see Figure 4.7, Figure 4.9).

Rao et al. [54] also discussed this focusing and spreading of particles through orifice jets and showed that the spread distance corresponding to the orifice jet was very dependent on the particle Stokes number. Particles with larger Stokes numbers, and hence more inertia, maintain lateral movement in the x and y directions even after being entrained in the orifice jet. These high Stokes number particles cross the jet axis and result in larger deposit diameters upon impact. Alternatively, smaller particles remain focused and impact the plate in a much more concentrated area. This particular phenomenon is investigated in more detail in [53].

Despite the spreading that occurs in the particle impact locations, the deposit structures that form experimentally can be considerably larger and even merge with adjacent cones. This indicates that other factors, such as particle sticking or adapted geometry may affect the particle trajectories and subsequent sticking locations.

5.3 Sticking Model Evaluations

5.3.1 Sticking Model Comparison on External Surfaces

Several studies were performed in OSU's Turbine Reaction Flow Rig (TuRFR) involving deposition on the external surfaces of nozzle guide vanes. As reported in [48], experiments were run with four different types of coal ash under the same operating conditions at temperatures near 1975 °F [1079 °C]. It was found that deposition is dependent on chemical composition, as deposition rates scaled inversely proportional with the rank of the coal ash, with higher ranks exhibiting a lower propensity to deposit.

Other experiments also found that deposition was dependent on fluid gas temperature, with little to no deposition occurring at temperatures below about 1800 °F [982 °C].

In the accompanying computational study [38], an Eulerian-Lagrangian deposition model was utilized to predict deposition rates on the nozzle guide vane surfaces based on the experimental conditions. It was found that particle impacts were dependent on the particle Stokes number. For the calculation of the Stokes number (eqn 1.4), the characteristic velocity and length scale were the average velocity at the vane cascade inlet and vane leading edge diameter, respectively.

Particles with larger Stokes numbers were much more likely to impact the vane surfaces due to ballistic (inertial) trajectories. Simulations were conducted for particle sizes ranging from 1 – 100 μm in diameter, and the results are depicted in Figure 5.5. The parameters plotted in Figure 5.5 are defined by equations 1.1-3.

Two sticking models were compared in this study, the critical viscosity and critical velocity models. The former, adapted from [25], assumes a sticking probability based solely on chemical composition and temperature, whereas the latter, adapted from [24], assumes a critical impact velocity, below which the particle kinetic energy is unable to overcome the adhesion forces during impact. This latter model proved to be overly sensitive to size, where small particles ($St_k < 0.1$) had a 100% chance of sticking and larger particles ($St_k > 2.0$) had nearly a 0% chance of sticking, but this was not observed experimentally. The critical viscosity model was used in subsequent external deposition studies because it more closely matched experiments in external deposition at high temperatures.

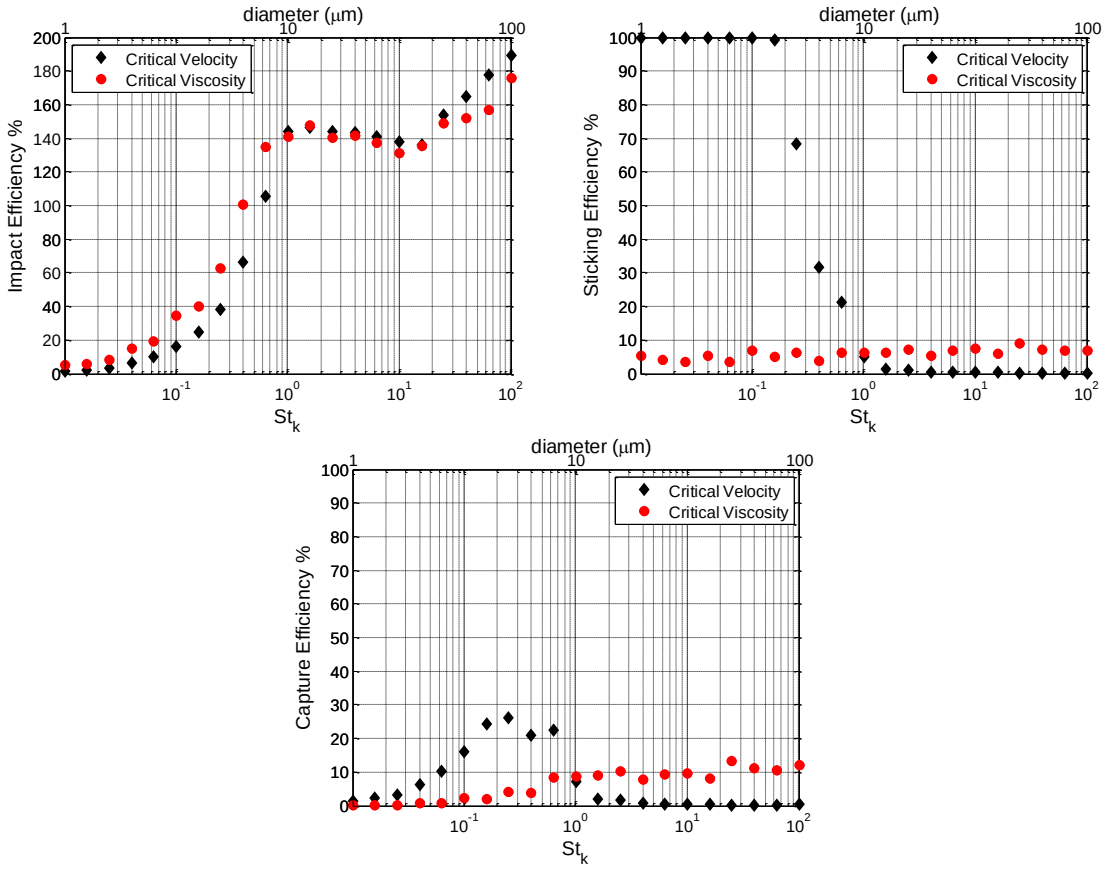

Figure 5.5 – Impact Efficiency, Sticking Efficiency, and Capture Efficiency from [38]

These sticking models were also evaluated for adequacy in internal deposition applications.

5.3.2 Critical Viscosity Model

As mentioned previously, simulations in external deposition made extensive utilization of the critical viscosity sticking model [38][39][51][55]. This model predicts particle sticking based solely on the particles' viscosity, which is a function of the elemental composition and temperature calculated from [26]. When particles impact a surface, kinetic energy from the particles can be dissipated by either elastic or plastic

deformation in the particles, in addition to creating or breaking adhesion forces of other particles on the surface. Particles with a large viscosity are less likely to plastically deform, and energy from elastic deformation can be restored to kinetic energy through the particle rebound. Alternatively, for low viscosity particles (with temperatures approaching the melting temperature of the particle material), the particle's kinetic energy upon impact is more easily dissipated through plastic deformation, increasing the probability of sticking.

5.3.2.1 Critical Viscosity Derivation

The critical viscosity sticking model assumes sticking based on a critical sticking temperature (T_{crit}). For temperatures below the critical sticking temperature, the sticking probability is given by the ratio of the predicted viscosity of the particle (μ_p) to the viscosity at the critical sticking temperature (μ_{crit}), according to the following relation.

$$P_{stick} = \begin{matrix} \mathbf{1}\ \boldsymbol{if}\ \boldsymbol{T_p > T_{crit}} \\ \frac{\boldsymbol{\mu_{crit}}}{\boldsymbol{\mu_p}}\ \boldsymbol{if}\ \boldsymbol{T_p < T_{crit}} \end{matrix} \qquad \textbf{[5.1]}$$

Senior and Srinivasachar [26] give a detailed derivation of the prediction of the viscosity-temperature relationship. A summary is shown here.

It is shown that the viscosity of silicate and aluminosilicate melts can be described by the form

$$\boldsymbol{\log\left(\frac{\mu_p}{T_p}\right) = A_{cv} + \frac{10^3 B_{cv}}{T_p}} \qquad \textbf{[5.2]}$$

Where T_p is the temperature in Kelvin, and A_{cv} and B_{cv} are constants that depend on the chemical composition. To acquire the values for the constants A_{cv} and B_{cv}, it is necessary to determine the chemical composition. Silicon dioxide is the basic building block of

these materials, and the presence of other oxides act to replace or disrupt the crystalline structure of the material, ultimately altering the temperature-viscosity relationship. The parameter used to describe this alteration is given by the ratio of non-bridging oxygen to tetrahedral oxygen, given by

$$(\boldsymbol{NBO/T}) = \frac{(\boldsymbol{CaO+FeO+Na_2O+K_2O+Al_2O_3-FeO})}{\frac{\boldsymbol{SiO_2+TiO_2}}{\boldsymbol{2}}+\boldsymbol{Al_2O_3+Fe_2O_3}} \qquad \textbf{[5.3]}$$

where the quantities are given in molar fractions. The values applied are the median values from the chemical composition of the ARD in Table 2.1, adjusted according to their respective molecular weight.

This value was used in conjunction with multiple constant values obtained through a multiple regression analysis described in [26]. Using these values, it was determined that the constants for A_{cv} and B_{cv} were -11.05 and 15.59, respectively. The critical sticking temperature was assumed to be 2200°F, identical to the measured sintering temperature of bituminous ash in [48].

The temperatures used in the present internal deposition studies are far below the sintering temperature of the particulate matter, estimated at 2200 °F (1200 °C) for the ARD. Because of this, the particles are not expected to exhibit these fluidic properties upon impact, and particle sticking would be the result of other forces.

Applying the critical viscosity model confirms that it is a poor predictor of particle sticking. Experiments show that deposition rates in internal cavities are only moderately dependent on temperature (factor of 2 between 700 °F and 1000 °F), but the critical viscosity model would predict no perceivable deposition at these temperatures. Simulations show that the viscosity model under predicts deposition rates by six orders of magnitude for temperatures at 1000 °F, and no measureable rates at lower temperatures.

Even major tuning of the model would not make the model predict what is observed in the experiments, so this model is not considered acceptable for these internal deposition applications.

The limitations of the critical viscosity model were also exposed in studies involving deposition on external surfaces, as illustrated in the following two papers comparing computations and experiments ([51][55]).

5.3.2.2 Critical Viscosity Model Results

Experiments and computations investigated particle deposition through vane passages with temperature non-uniformities (hot streaks) in the inlet gas flow. In the solely computational study (discussed in detail in [55]), the critical viscosity sticking model was utilized to model deposition on a nozzle guide vane passage with a simulated hot streak. The computational model incorporated non-uniform inlet temperature conditions to account for the existence of an idealized hot streak. The distribution of the temperature non-uniformity was shown to affect the location and amount of deposition measured on the nozzle guide vanes. Using a periodic condition that simulated one combustor nozzle for every two nozzle guide vanes, repeated at several clocking positions, the computational model predicted the optimal circumferential location of the combustor nozzle to minimize total deposition rates in the vane passage. Particles that were immersed in or passed through the hot streak were more likely to stick upon impact due to their elevated temperature. The deposition rates were strongly correlated to the average surface temperature of the vanes, but the clocking position with minimum deposition did not correlate to the clocking position with lowest average surface temperatures. The effect of particle size, or Stokes number, on deposition was also

studied and discussed. Predicted deposition trends also qualitatively matched the observed trends seen in Figure 1.1, where hot streaks, due to the fuel injector locations, caused elevated levels of volcanic ash deposition on every second vane within the passage.

Hot streaks were simulated experimentally in the TuRFR and modeled computationally, as discussed in [51]. Modifications to the TuRFR allowed for the creation of simulated hot streaks in a four-vane annular cascade operating at temperatures up to 2000°F [1093°C]. Total temperature surveys were made at the inlet plane of the vane passage, showing the variation caused by cold dilution jets. Deposition was generated by introducing sub-bituminous ash particles with a median diameter of 11.6 μm far upstream of the vane passage. Results indicate a strong correlation between surface deposits and the hot streak trajectory. A computational model was developed utilizing the critical viscosity model and an Eulerian-Lagrangian particle tracking technique. The computational simulations confirmed the migration of the hot streak and locations susceptible to enhanced deposition.

Figure 5.6 shows some of the experimental and computational deposition results from [51], with experimental results on the left for two vanes and two test conditions, and the corresponding computational results on the right. For the baseline case without the temperature non-uniformity, both experiments and computations show similar deposition patterns for the upper and lower vanes. However, the computational results predicted peaks in deposition on the trailing edge of the vanes not seen in the experiments. The over-prediction of deposit was also seen in the computational studies of [38].

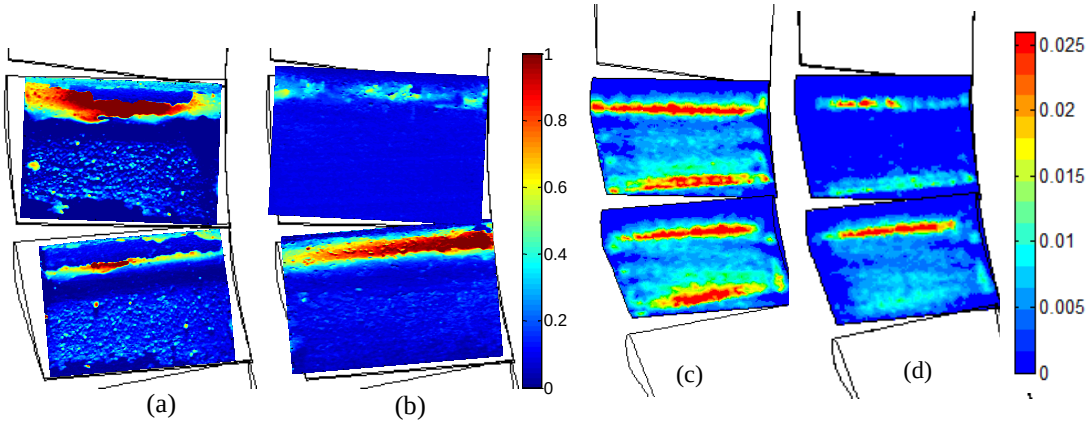

Figure 5.6 – Deposition results from [51]. Experimental thickness shown in mm. for (a) baseline and (b) hot streak. Computational capture rates shown in mm/g for (c) baseline and (d) hot streak.

Because this study directly compared computations and experiments with identical geometries and operating conditions, it exposed both the strengths and weaknesses of the computational model. The model accurately predicted deposition locations on the external vane surfaces, with peaks at the leading edge and buildup over the pressure surface, with little or no deposit on the suction surface. However, the computational model over-predicted total capture efficiency rates by a factor of ten. It revealed that the sticking model was not sufficiently sensitive to temperature, (whereas for internal deposition, it would be overly sensitive). It also predicted deposition peaks at the trailing edge of the pressure surface on the NGV, unseen in the experiments.

5.3.3 Critical Velocity Model

5.3.3.1 Critical Velocity Model Derivation

The critical velocity model predicts sticking if the particle impacts with a velocity below a critical value, according to the following relation.

$$P_{stick} = \begin{matrix} \mathbf{1} & \mathbf{if} & \boldsymbol{V_N < V_{crit}} \\ \mathbf{0} & \mathbf{if} & \boldsymbol{V_N > V_{crit}} \end{matrix} \qquad \textbf{[5.4]}$$

This assumes that the adhesion forces acting on a particle can overcome the rebounding kinetic energy of particles impacting below a critical velocity. This critical velocity limit is influenced by factors such as particle size and material properties of both the particle and surface. The value for the critical impact velocity, V_{crit} is calculated from the relations described in [22], by the following relations.

$$\boldsymbol{V_{crit} = \left[\frac{2E}{d_p}\right]^{\frac{10}{7}}} \qquad \textbf{[5.5]}$$

$$\boldsymbol{E = 0.51\left[\frac{5\pi^2(k_1+k_2)}{4\rho_p^{\frac{3}{2}}}\right]^{\frac{2}{5}}} \qquad \textbf{[5.6]}$$

$$\boldsymbol{k_1 = \frac{1-\nu_w^2}{\pi E_w}} \qquad \textbf{[5.7]}$$

$$\boldsymbol{k_2 = \frac{1-\nu_p^2}{\pi E_p}} \qquad \textbf{[5.8]}$$

In these relations, E is the composite Young's modulus, E_w is the surface Young's modulus, E_p is the particle Young's modulus, ν_w is the surface Poisson ratio and ν_p is the particle Poisson ratio.

These values are difficult to measure experimentally as they have a strong dependence on temperature. In the studies of this paper, correlations were applied from calibrations used by [24].

$$\boldsymbol{E_p = E_s = 3 \times 10^{20} e^{-0.02365\, T_A}} \qquad \textbf{[5.9]}$$

$$\boldsymbol{T_A = \frac{T_p + T_w}{2}} \qquad \textbf{[5.10]}$$

The values of the Poisson ratios were both assumed to be 0.27, and the temperature applied to calculate the Young's modulus used the average temperature of the particle and the wall.

5.3.3.2 Critical Velocity Model Results

The study in [38] compared the critical viscosity model to the critical velocity model. For external deposition, the velocity model proved to be very unrealistic for two principle reasons.

First, it doesn't account for plastic deformation. At high temperatures, particles can be partially molten upon impact and plastic deformation is a major contributor to particle sticking, which is why the critical viscosity model was justified and applicable.

Second, the model, as generally applied, is very sensitive to particle size. The study in Figure 5.5 predicted nearly 100% sticking for particles of $St_k < 0.2$, and 0% for particles of $St_k > 2.0$ (See Figure 5.5), whereas experiments refuted such a strong dependence on particle size. The model determines sticking based on whether the kinetic energy of the particle is able to overcome the adhesion forces and energy dissipation during impact. The predicted adhesion force within the model is proportional to the maximum contact area between the particle and surface during impact, which is derived from analytical approximations from perfect spheres impacting a perfectly flat surface. In reality, the particles are not spherical and the surfaces are not perfectly flat. Many of the particles don't impact a flat surface at all, but rather impact a layer of previously existing deposit. Hence, when particles impact a surface, the predicted "contact area" and associated adhesion forces, in reality, may vary by large factors or even orders of magnitude. Additionally, particles impacting other particles likely have contact with

multiple surfaces of other particles. Kinetic energy from the impacting particles is dissipated not only from the particle itself, but also from the breaking of adhesion bonds from preexisting deposit [52].

The first issue doesn't apply for internal deposition applications. With internal deposition, the temperatures and impact velocities are relatively low and plastic deformation is expected to be minimal. The physics leading to adhesion are assumed to be correct from the critical velocity model theory, but not in the simplified form of spherical impacts.

Experiments show that the same formations of deposit can occur whether the flow temperature is 1000 °F or 70 °F. The rates change moderately, but are certainly more similar as opposed to higher temperature, external applications. Simulations were conducted using the present flow model using the critical velocity sticking model, but again proved to be overly sensitive to both particle size and temperature. Like the viscosity model, deposition was under predicted at temperatures of 1000 °F by a factor of about 1000, and no deposit was predicted at ambient conditions. This confirms that the model, even if predicting the correct methods of adhesion, is not adequate in the current calibrated form for the present internal deposition case.

5.3.4 Calibrated Critical Velocity Model

As mentioned, the adhesion forces during impact are directly proportional to the area of contact, which can vary widely depending on the particle shape and size. As direct measurements of contact areas are impractical, experiments can be used to calibrate this factor in the particle sticking model. This calibration was performed through experiments and preliminary computations, according to the following steps:

1. Run simulation tracking particles of multiple sizes
2. Determine impact efficiency according to particle size
3. Analyze pre-test deposit dust to determine particle size distribution
4. Run experimental test at same conditions and measure capture efficiency
5. Analyze post-test deposit dust to determine particle size distribution
6. Extract capture efficiency as a function of particle size
7. Extract sticking efficiency by particle size from experimental capture efficiency and computational impact efficiency

The computational model utilized the results from the simulation in Figure 5.2. These test cases revealed that smaller particles impact the plate surface with higher velocities than larger particles, which is the opposite compared to external deposition applications. As the length scales are small, all particles have Stokes numbers well above unity, signifying that particle inertia will dominate the trajectories. Particles are initialized with low velocities near the CFD inlet (in equilibrium with the flow), and as the particles are entrained in the orifice jet, their inertia prevents the particles from ever being accelerated to the speed of the jet. Larger particles are more resistant to this acceleration, resulting in lower velocities upon impact.

These impact efficiencies were compared to experiments run at the same test conditions (Tests 18a-c). The accumulated dust deposit was collect and measured. The bulk capture efficiency was an average of 1.9% (Table 4.1), but this metric alone does not reveal enough for the sticking model. The collected deposit was measured with a Shimadzu SA-CP4 particle size analyzer (described in Webb [56]) and compared with the

size distribution of the feed dust shown in Figure 5.7, also measured with the Shimadzu SA-CP4.

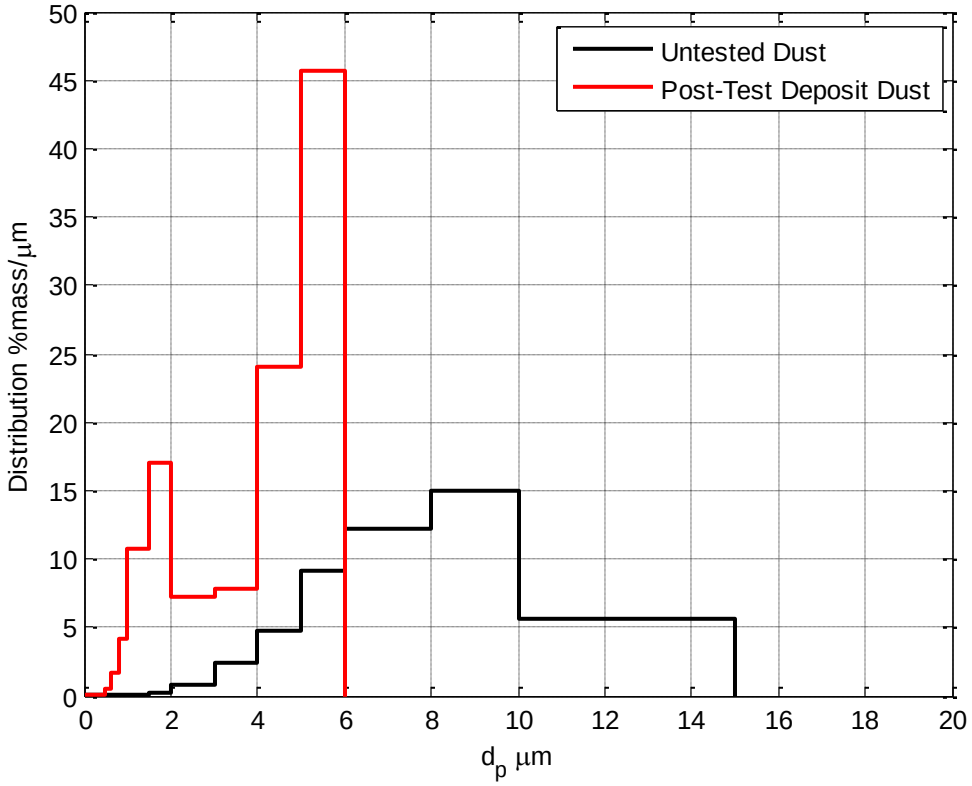

Figure 5.7 – Particle size distribution for untested dust and post-test dust

The size analysis shows a histogram of particle sizes acquired from samples of the pre-test and post-test dust. It revealed that the post-test deposit buildup was composed almost entirely of small particles below 6 µm in diameter, whereas the same analysis with the feed dust detected particles up to 15 µm. This suggests that particle sticking efficiency is inversely proportional to particle size, which is also predicted by the critical velocity model in Figure 5.5.

It should be noted that the Shimadzu particle size analyzer is limited at predicting mass distributions for large sizes, evidenced by the coarse bin structure in Figure 5.7. The size analyzer acquires a distribution by measuring thousands of individual particles from a sample. Because the mass of the particles scales as the third power of the diameter, the presence or absence of a few large particles in the measurement sample can skew the distribution of particle sizes based on mass. This may account for part of the discrepancy between the size analysis for pre-test dust from the Shimadzu (Figure 5.7) and the distribution provided by the distributor (Figure 2.8). It should also be noted that the size distribution of post-test dust in Figure 5.7 may be due to other possibilities than smaller particles having a higher propensity to stick. For example, if larger particles break apart upon impact with solid surfaces within the facility, or have a higher propensity to accumulate on the internal components of the facility, then the accumulated deposit would show a bias for smaller particles.

From the differences in the size distribution, the capture efficiency can be computed for multiple particle sizes. The distributions from Figure 5.7 were discretized into the five sizes that were used in the CFD computations, shown in Table 5.1.

Table 5.1 – Size measurements for sticking model calibration

	Experimental Measurements			CFD		
Particle Diameter (µm)	Untested % Shimadzu	Post Test % Shimadzu	Capture Efficiency (Total ~1.9%)	Particle Diameter (µm)	Impact Efficiency	Calculated Sticking Efficiency
<4	3.53%	30.2%	16.3%	3	168%	**9.7%**
4-6	13.8%	69.8%	9.6%	5	146%	**6.6%**
6-8	24.3%	0%	0%	7	143%	**0%**
8-10	29.9%	0%	0%	9	144%	**0%**
Over 10	28.5%	0%	0%	11	147%	**0%**

From the distributions shown in Figure 5.7, 30.2% of the collected deposit consisted of particles of diameter less than 4 μm, despite only 3.5% of the pre-test dust being measured at this size. The size-specific capture efficiency can be calculated by the following.

$$\textbf{Size Specific Capture Efficiency} = \frac{\textbf{Distribution}_{\textbf{Post}}}{\textbf{Distribution}_{\textbf{Pret}}} \times \textbf{Total Capture Efficiency} \quad \textbf{[5.11]}$$

The calibrated sticking efficiency can then be calculated by changing the form of Eqn. 1.4 to the following.

$$\textbf{Calibrated Size Specific Sticking Efficiency} = \frac{\textbf{Size Specific Capture Efficiency}}{\textbf{Impact Efficiency}_{\textbf{CFD}}} \quad \textbf{[5.12]}$$

This results in a predicted sticking efficiency for the different sizes, and assumes that the impact efficiency doesn't significantly change as deposit grows during a test.

The first calibrated sticking model assumes that the critical sticking velocity for the various particle sizes would equal the impact velocity from which the percentage of particles impact with a normal impact velocity slower than the resulting sticking efficiency from Table 5.1.

The impact velocities were investigated from the simulations previously discussed. The normal impact velocities of all particles were obtained, and Figure 5.8 shows the cumulative probability functions of impact velocity by size, relative to the velocity of the fluid impingement jet.

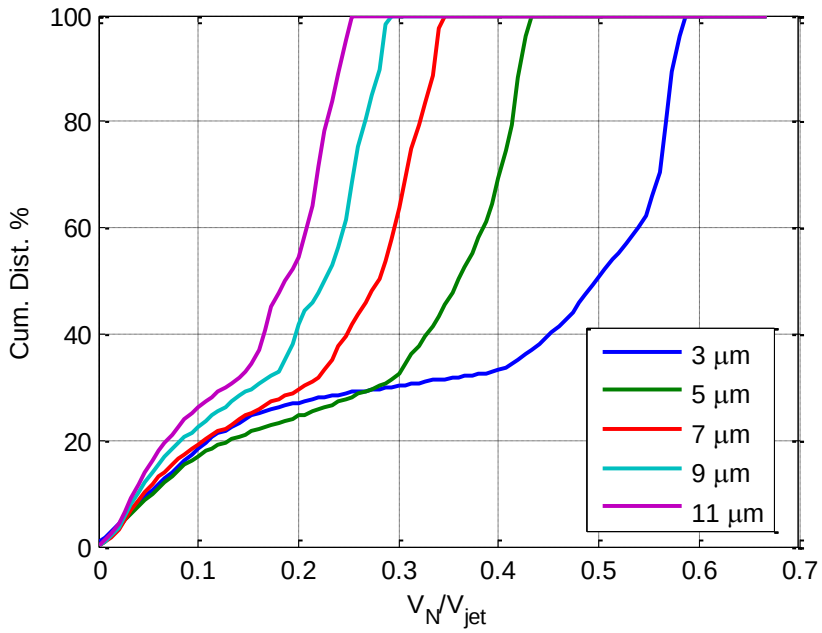

Figure 5.8 – Cumulative distribution of particle impact velocities by size

The critical velocity model predicts that the lowest-velocity particle impacts result in sticking. The predicted sticking efficiency for particles of 3 µm diameter is 9.7%. For these particles, 90.3% impact with normal velocities exceeding V_N/V_{jet} = 0.08, and 9.7% impact at lower velocities. It can therefore be predicted that, ignoring other factors such as temperature, V_N/V_{jet} = 0.08 would be a suitable critical velocity for this size which would result in the same capture efficiency from the experiments used for the calibration. By the same method, the critical sticking velocity for 5 µm particles is V_N/V_{jet} = 0.06, and V_N/V_{jet} = 0 for larger particles.

The deposition model was run with this sticking model using the same conditions as the simulation in Figure 5.2. The locations of sticking particles are shown in Figure 5.9.

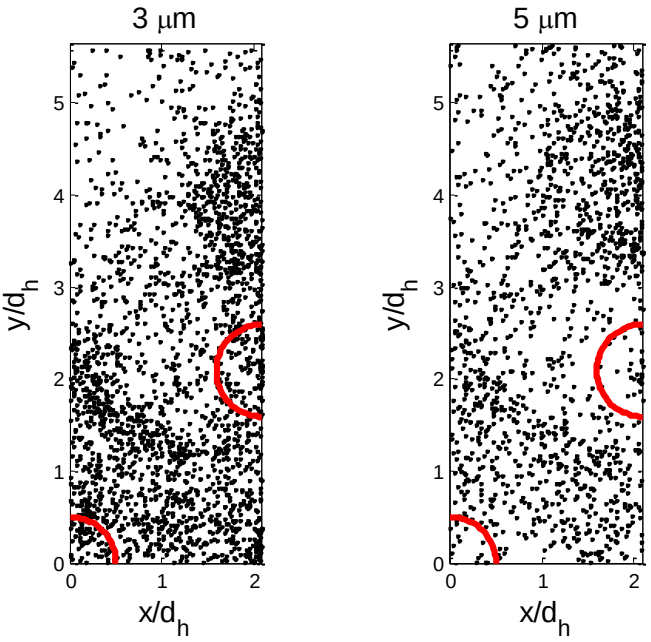

Figure 5.9 – Deposition locations with normal particle impacts below V_N/V_{jet} = 0.8 for 3 μm particles, V_N/V_{jet} = 0.6 for 5 μm particles.

The red arcs in Figure 5.9 show the spatial locations of the impingement jet holes, which also correspond to areas of both total impact propensity and deposit growth seen in experiments. However, the sticking locations in Figure 5.9 show the opposite trend, with particles sticking at locations spread everywhere, and in the case of 5 μm particles, fewer sticks near the impinging jet region. This is because the impacts that result in sticking, according to the model, are those at lower velocities which result from trajectories after multiple rebounds. The initial impacts, which correspond to the concentrated impact locations directly below the orifice holes in Figure 5.2, are at high velocities and therefore predicted not to stick under this model, Therefore, such a "calibrated" critical velocity model does not capture the same deposition patterns and is not adequate for internal deposition applications.

5.3.5 Calibrated Critical Kinetic Energy Model

The previously discussed model also assumed a distinct critical velocity for each particle size, making it unusable for other size distributions. Another calibrated model was developed to utilize the critical velocity principles and attempt to come closer to match the experiments. This was done by creating a sticking model based more directly on impact kinetic energy. The kinetic energy of all impacting particles was compiled as shown in Figure 5.10, comparable to Figure 5.8. Smaller particles have much less kinetic energy, even when impacting at higher velocities. If it is assumed that there is a critical sticking kinetic energy as opposed to a velocity, below which the particle does not have sufficient energy to overcome rebounding forces, then the model can utilize an individual value while still matching the predicted sticking efficiencies for all particle sizes in Table 5.1.

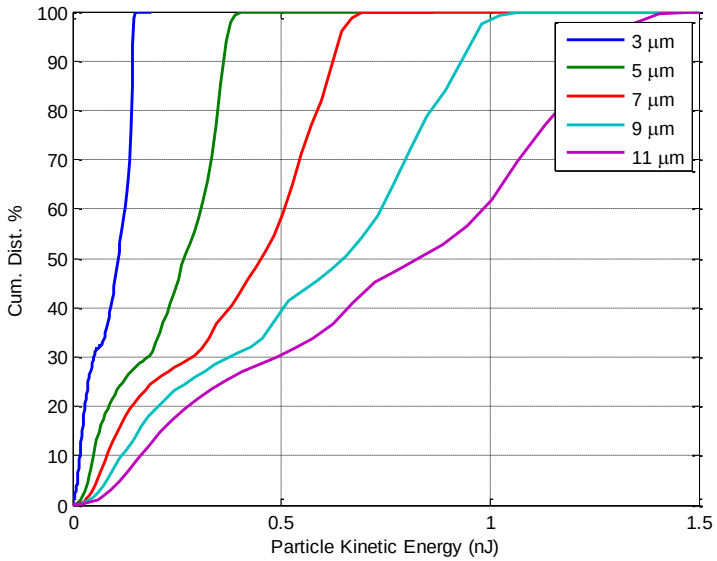

Figure 5.10 – Cumulative distribution of kinetic energy of impacting particles

As was explained previously, particles are not spherical, which leads to a wide range of particle adhesion values during various impacts, even for the same particle. Because of this, the particles of a given size are expected to have a probabilistic model of sticking, instead of a cutoff. (This probabilistic approach made the critical viscosity model better in matching experimental observations in previous studies [38][48]) To match the sticking probability for the 3 μm and 5μm particles, the probability of sticking can be written as

$$P_{stick} = \begin{matrix} \beta(T_P) \; if \; KE_p < KE_{crit} \\ 0 \; if \; KE_p > KE_{crit} \end{matrix} \qquad \textbf{[5.13]}$$

β is the probability of sticking that is dependent on temperature. From Table 5.1, 3μm particles are about 50% more likely to stick than 5μm particles. Utilizing the distribution from Figure 5.10, a value is found where 50% more impacts occur (below this value) of 3μm particles compared to 5μm particles. The determined value is 0.33 nJ, as 100% of 3μm and 66% of 5μm particles impact with less energy.

Experiments in this study as well as Carey [53] suggest that while temperature is a factor in particle sticking, even at low temperatures, the influence is much less pronounced compared to hot, external deposition applications. The difference in rates is only about a factor of two comparing inlet temperatures of ambient and 1000 °F. The sticking probability based on temperature can be matched with the critical kinetic energy value defining the probability of sticking, and is given as the following equations. The temperature applied is the average of the particle and wall surface temperatures.

$$\beta(\%) = 2.6 + \frac{T_A[°K]}{117} \qquad \textbf{[5.14]}$$

This incorporates the necessary probabilistic nature of particle sticking which is inherent in these calculations, with the potential to more closely match the sticking trends seen in the calibration analysis. The first simulation was run using this sticking model, and particle sticking locations are shown in Figure 5.11.

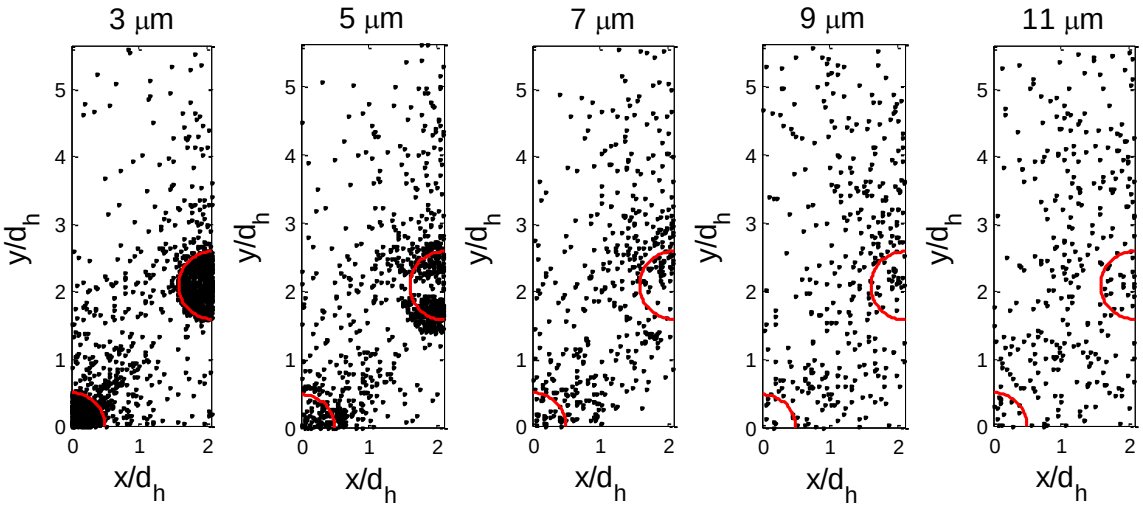

Figure 5.11 – Deposition locations using calibrated kinetic energy model

The impact locations for the smaller particles occur predominantly where the impingement jets are located. This is expected, as the critical impact energy was chosen to be above all impact energies of 3μm particles and 67% of 5μm particles. The sticking locations of the 3μm particles are therefore simply a sample, by a factor of β, of the impacts from Figure 5.2. Because the temperatures of all of the particles upon impact are relatively uniform, the sticking locations of the 5μm particles are also a slightly biased sample of the impacts from Figure 5.2. For the other particle sizes, the particles that stick experience the same issues as those in Figure 5.9, in that particles only stick after being decelerated by prior impacts, and stick in locations that aren't supported by experiments.

Another problem with this model occurs with the sensitivity to particle size. While the smaller particle sizes contain much less kinetic energy, some larger particles do impact with lower kinetic energies and are assumed to stick. Because 82% of the injected particles (by mass) are larger than 6 μm, and 0% are predicted to stick, (Table 5.1) a small inconsistency in calibration for these particles causes large discrepancies between the measured experimental capture efficiencies and predicting sticking efficiencies from the model. This model was calibrated using 3 μm and 5 μm particles, and larger particles were neglected. However, simulations on a clean geometry reveal that 3.85% of particles larger than 6 μm stick, leading to a total capture efficiency of 5.05% instead of 1.9%, or an over-prediction of 166% and is not consistent with Figure 5.7.

Further, the agreement of this model with experiments occurs not because of the critical energy criterion, but simply that most particles below 6 μm in diameter are given a probability of sticking, with little influence from other factors.

5.3.6 Simple Probabilistic Model

Each of the previously discussed sticking models falls short of predicting deposition locations and buildup seen experimentally. Smaller particles were found to be the particles that resulted in sticking, but their sticking locations appeared to not be directly influenced by impact velocity. The highest velocity impacts for all particle sizes from the simulations were the first impact after passing through the impingement hole, and this was generally the location of highest deposition growth. For this reason, a sticking model was used to investigate the geometry modification using a sticking probability taken directly from Table 5.1; 9.7% for <4 μm particles, 6.6% for 4-6 μm particles, and 0% for particles larger than 6 μm in diameter. This was done to investigate

the influence of geometry adaptation on the deposition of particles, isolated from other factors that may have an effect.

5.4 Influence of Geometry Adaptation

A simulation was run utilizing the geometry adaptation technique discussed in the methods section, and maintaining a constant sticking efficiency from the measurements taken in Table 5.1. Each iteration involved the injection of 50,000 particles, consisting of five particle sizes (though only two of the sizes were considered for sticking), and simulated an injection of 0.05 grams of deposit per iteration, relative to the experimental tests. This was necessary to maintain steady growth of the deposit structures without any abnormally large growth in any single iteration. The three dimensional deposit growth surfaces are illustrated in Figure 5.12.

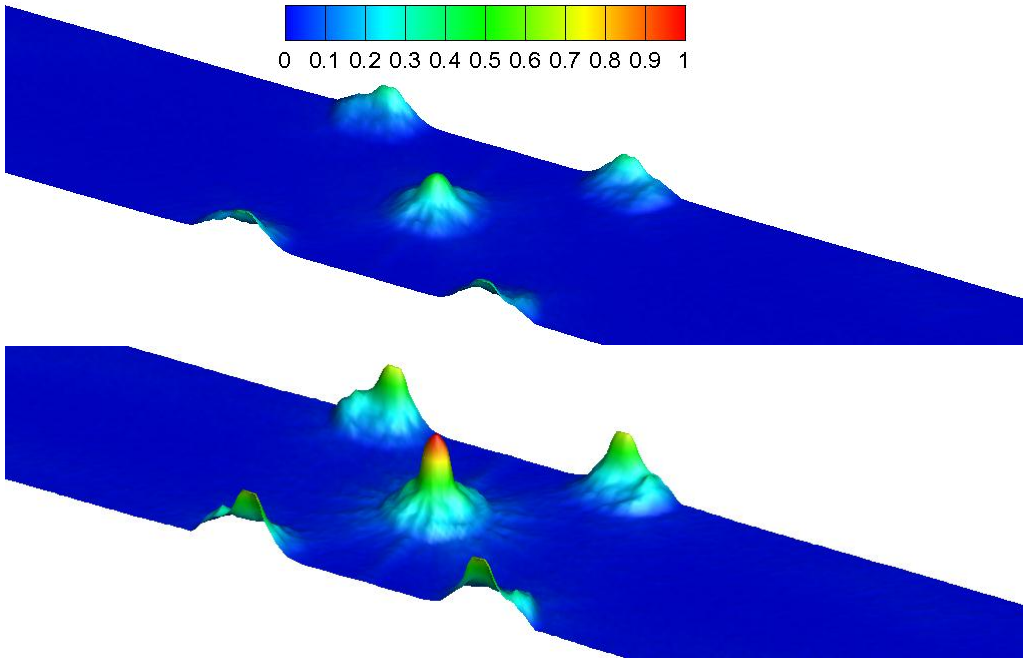

Figure 5.12 – Mesh surfaces generated from deposition model after (top) 4 iterations representing 0.2 g of injected dust, and (bottom) 8 iterations representing 0.4 g of injected. Contours are surface height in mm.

From these surfaces, linear traces were taken in the x and y directions through the center of each impingement jet, and the results are shown in Figure 5.13.

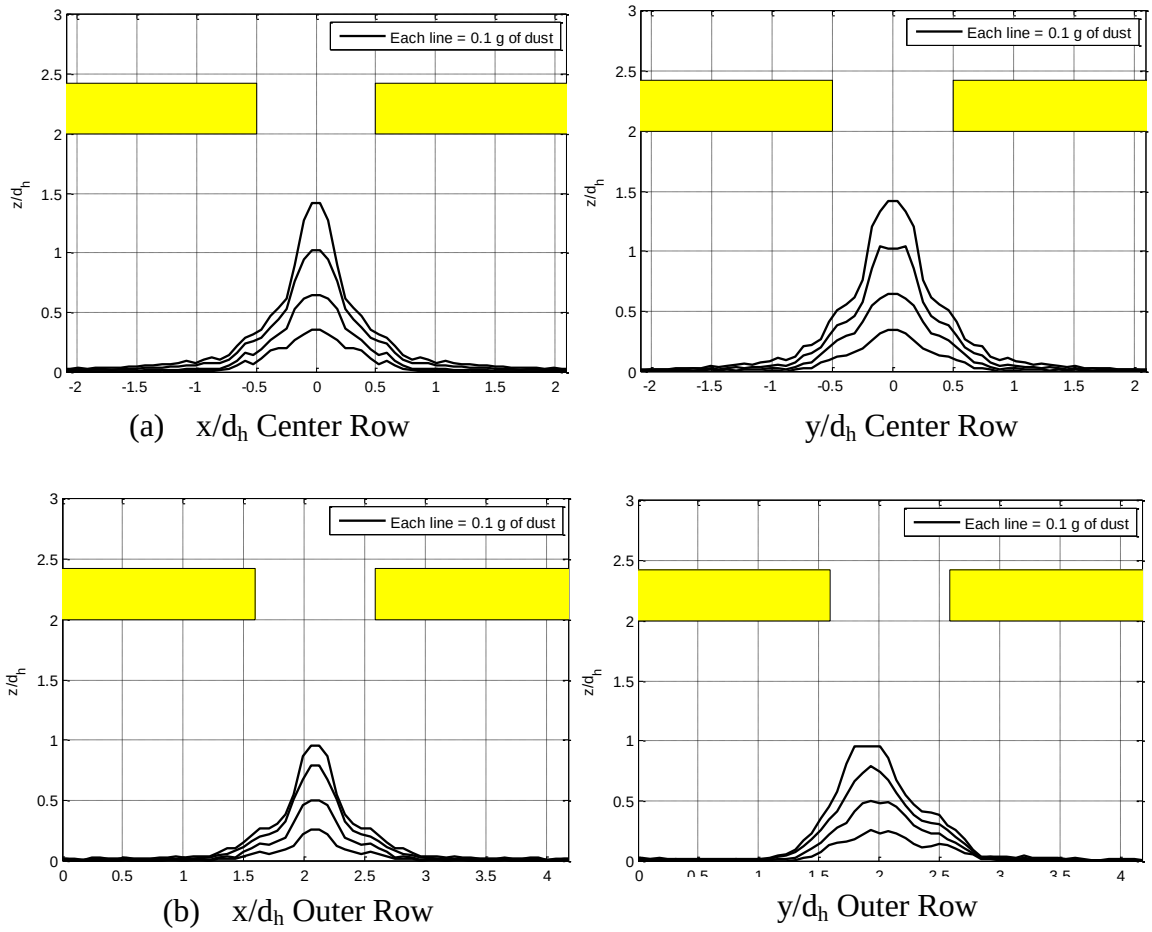

Figure 5.13 – Deposit growth over eight growth iterations for (a) center row of holes and (b) outer row of holes

After only 0.4 grams of simulated deposit dust was fed into the system, the computational flow solution failed to converge. For this reason the computational simulation was not continued beyond this point. However, by this iteration in the computation, the deposit cone representing the center row had already grown to a height of 70% of the gap width. It can be assumed that only about 0.2 g of additional simulation

deposit would be required for the center row deposit cone to fill the gap to the impingement hole, assuming a continued growth rate. In reality, it may require less as the growth rate of the cone is increasing due to the aerodynamic focusing effect discussed previously.

This shows the influence of geometry adaption, which can be seen in the Figure 5.14 where the deposit thickness is predicted without grid adaptation. These plots assume a constant vertical deposition growth rate.

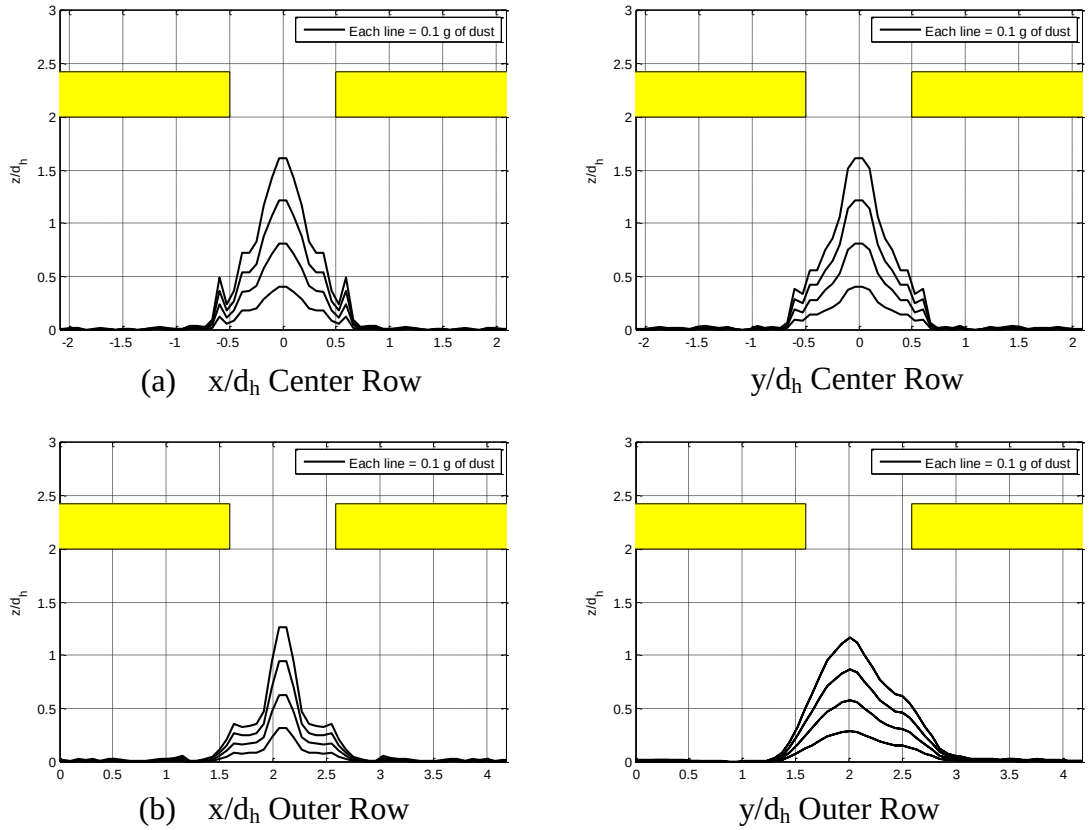

Figure 5.14 – Deposit growth without grid modification for (a) center row of holes and (b) outer row of holes

Deposit growth without grid modification indicates that the deposition cones remain confined in width, never to exceed a diameter of about 1.4 hole diameters, whereas the adaptation technique predicts widths of nearly 2.0 hole diameters.

The grid adaptation also revealed an important conclusion regarding particle tracking. While the presence of the deposit cone did change how the particles rebounded, when impacting preexisting deposit, it did not significantly alter the initial trajectories of the particles through the orifice or the initial impacts. The fluid flow field upstream and within the orifice was not altered with the growth of the cone, and it is this region that has the dominant influence on the particle trajectories. Particles that are entrained in the flow near the orifice are accelerated with the impingement jet. With this acceleration in velocity, the particles' Stokes numbers increase well above unity. With the higher Stokes numbers, the path of the particle becomes more ballistic, and the trajectory prior to the initial impact on the impact plate, or preexisting deposit, is unaffected by the alternate downstream geometry. Further analysis is shown in section 6.4.

5.5 Comparison to Experiment

These growth patterns both with and without geometry modification are compared to the linear traces from the experiments in Figure 4.8. Linear traces from the two computational data sets and the experimental growth are shown in Figure 5.15. While the general growth trend is similar, clear discrepancies also persist. The height of the cone grows vertically at a rate about 120% faster in the CFD with grid adaption compared to the experiments, whereas the CFD without grid adaptation grows at rates about 150% faster. Experiments show that the base of the deposit cones can expand to fill the entirety of the base plate, representative of a base width of about 3 hole diameters.

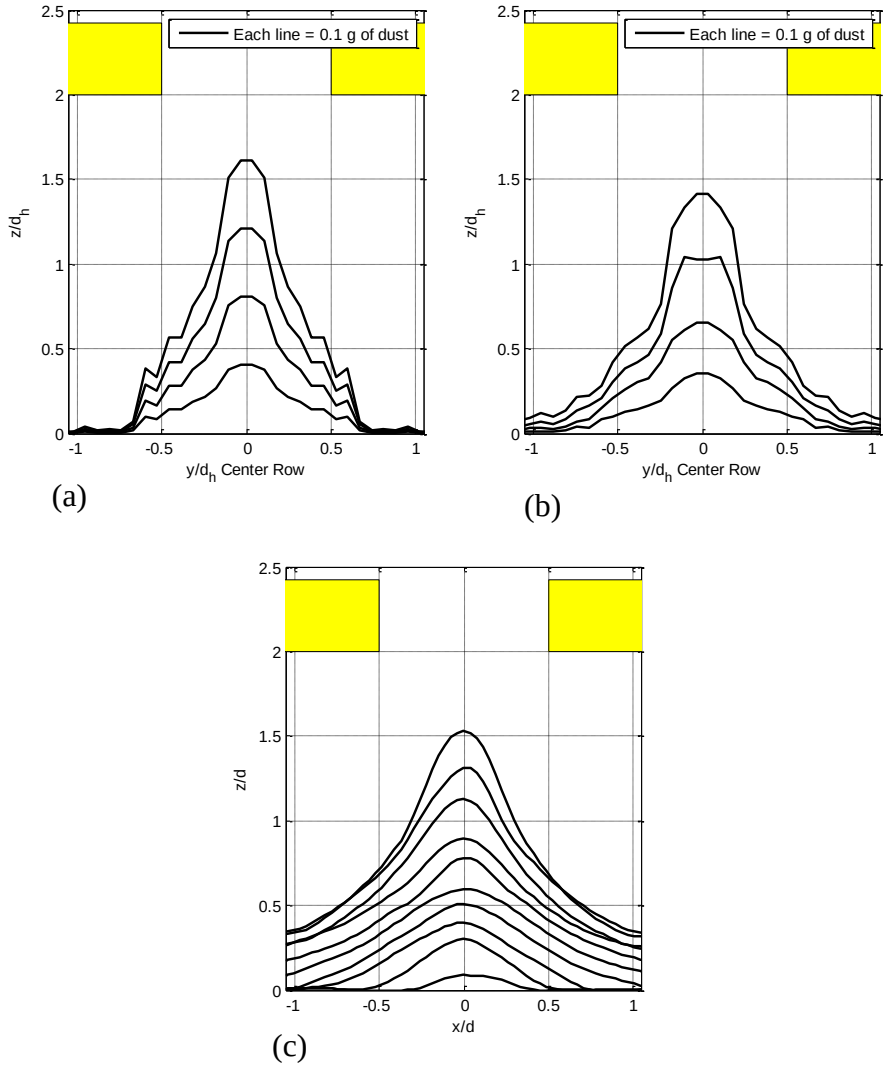

Figure 5.15 – Comparison of deposit growth (a) CFD without geometry adaptation – 0.4 g total, (b) CFD with geometry adaptation – 0.4 g total, and (c) experimental – 1.0 g total.

The grid adaptation was employed because it was believed that it would cause the deposit growth to more closely match the experiment, in that the conical deposit growth would cause more particles to impact and stick at larger radial positions relative to the impingement jet, due to modified rebounds from pre-existing deposit. While the geometry modification does slightly improve the comparison with the experimental

results, it still lacks agreement in structure, even after the capture efficiency calibration. Clearly some factor in deposit growth is lacking. Additionally, no sticking model predicts any growth in form similar to those seen in Figure 4.4.

5.6 Chapter Summary

Several computations were conducted on a 3D flow solution with multiple sticking models. The progression of the simulations, as well as the principle conclusions, is shown in the flow chart in Figure 5.16.

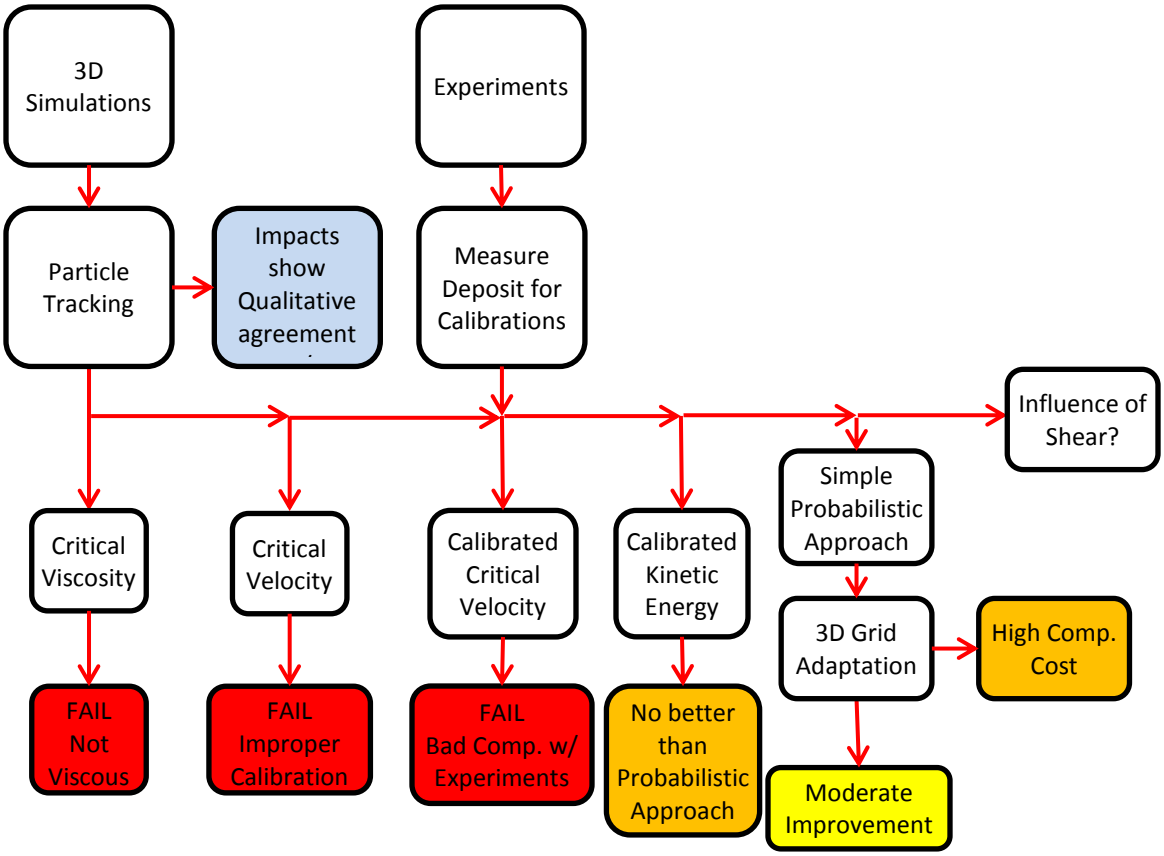

Figure 5.16 – Progression of computational simulations with principle conclusions

After acquiring a flow solution that closely matched the flow in the experiments, the particle tracking alone provided qualitative agreement with the experiments in that it predicted concentrated particle impacts in the locations of primary deposit buildup. Two previously used sticking models were applied to this particle tracking simulation. The critical viscosity model failed because the particulate matter was not hot enough for sticking to be based on viscosity. The critical velocity model also failed, presumably due to improper calibrations utilized in other studies. Attempts were made at calibrating the critical viscosity model, but the resulting deposit growth disagreed with experiments based on deposit growth. A second calibrated model showed that the sticking model was no better than a simple probabilistic approach to sticking, which was used in conjunction with grid adaptation.

The influence of grid adaptation only moderately improved the accuracy of the results, but at an order of magnitude of increased computational expense. Additionally, no sticking model would predict the “ridge” formations seen in some of the experiments. It was concluded that these computational models were lacking critical physics present in the deposition process, leading to further studies investigating the influence of shear on sticking.

Chapter 6. Influence of Shear on Sticking

Up to this point, the computational model has ignored the effects of wall shear on particle sticking. It was determined that particle tracking, previously discussed sticking models, and geometry adaptation were all incomplete in predicting particle buildup on deposition. Experiments at high flow rates revealed that shear may play an important role in large-scale particulate removal, and it was desirous to know whether this also played a role in individual particle sticking or movement along the wall surface.

This chapter discusses several studies relating to the effect of wall shear on deposition. It begins with an experimental and computational study that modifies the experimental test piece that provides cross flow to the impinging jets. This cross flow changed the wall shear in the impingement regions, and the resulting deposit buildup is discussed. The wall shear was then investigated computationally on single, axisymmetric impingement jets without deposit, showing that initial deposit growth occurs in regions of low shear. The computations were modified afterward by including idealized, triangular deposit cones to show how the wall shear changes in both magnitude and location, and suggest how this dynamic process changes locations that are susceptible to deposition. Computational studies also showed how particle trajectories, prior to initial impact, are mostly unaffected by the presence of deposit cones. This allows for simplifications in particle tracking for subsequent deposition models

A novel shear-based sticking model is then developed that predicts particle sticking based on wall shear, on an axisymmetric computational domain. The shear-based

model also allows for the transport of particulate along the wall in the direction of the shear, simulating the rolling or sliding of particles that were previously ignored. This model, combined with geometry adaptation and a simplified particle tracking technique, revealed features of deposit buildup observed in the experiments that weren't predicted by previously discussed computational models. The CFD outlet condition was modified to approximate conditions present in an array of impingement jets, and the deposition model was rerun. Adjustments to the flow solution and sticking parameters in the model also agree with trends in deposition investigated experimentally, furthering credence to the computational model.

Finally, the predictions of the computational model are compared and shown to be in agreement with experimental studies from external researchers. The model is also discussed in regard to studies of deposition on external deposition previously performed by the author.

6.1 Cross Flow Experiment

An experiment was run with the test section reconfigured so that the impinging flow was restricted from exhausting in the same way as previous experimental tests shown in Figure 6.1. Flow was blocked on either side of the rows of impingement holes, and at one end, forcing all of the flow to exhaust at the other end.

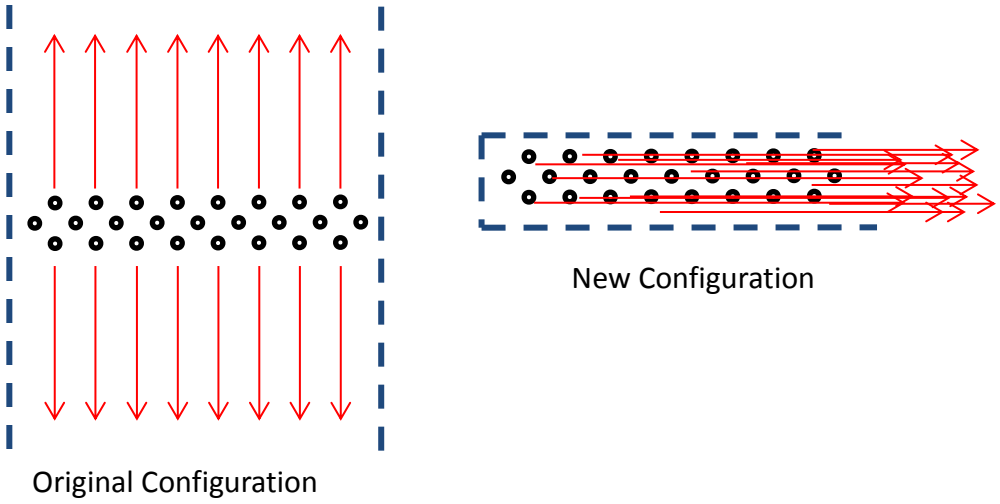

Figure 6.1 – Experimental configuration for impingement jets with cross flow

This configuration resulted in steadily increasing cross flow for right-most impingement jets in Figure 6.1, with cross flow being defined as the average flow velocity in the x-direction at the location of the impinging jets. A deposition test was run at ambient temperature conditions with the same total mass flow as in previous experiments (0.8 scfm). The growth of the deposit cones was inversely proportional to the cross flow velocity associated with each jet. In the right-most impingement jets, no deposition forms and the surface remained clean, even more than the region in between the cones where a very thin layer of dust accumulated. This is shown in Figure 6.2. The test was conducted on a transparent glass surface for backside optical access during the test, as the new configuration did not provide the same access as previous tests. Because of the difference in wall material and surface roughness, the capture efficiency was not compared to other tests, but it did provide valuable information.

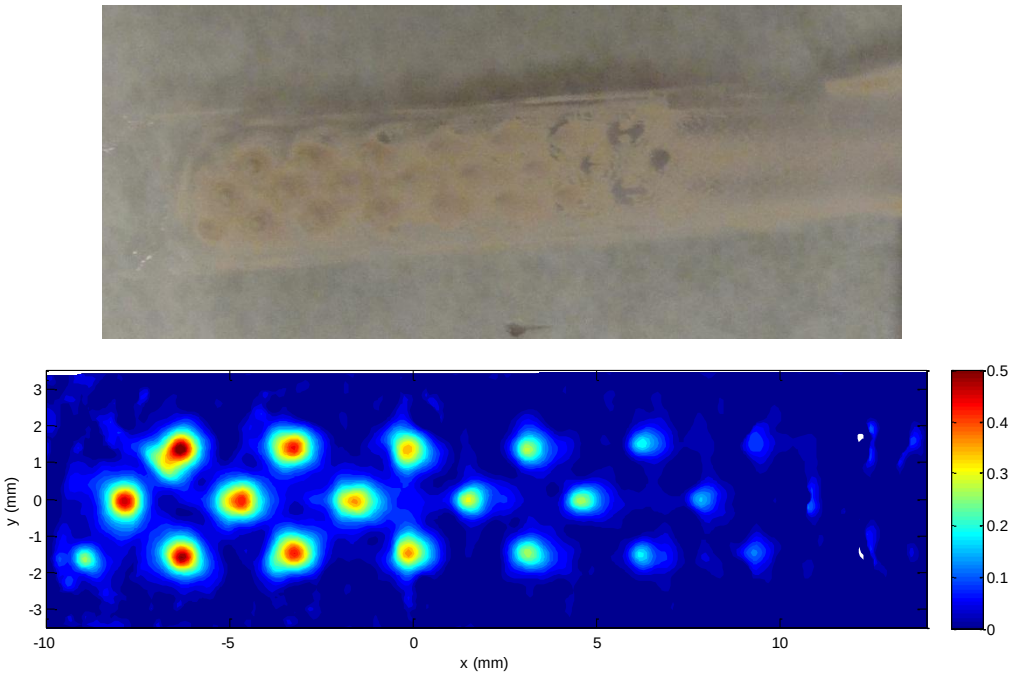

Figure 6.2 – Photograph and optical scan of deposit thickness [mm] from cross flow experiment

The distinction in deposit thickness is even more pronounced with the linear traces of deposit, shown in Figure 6.3.

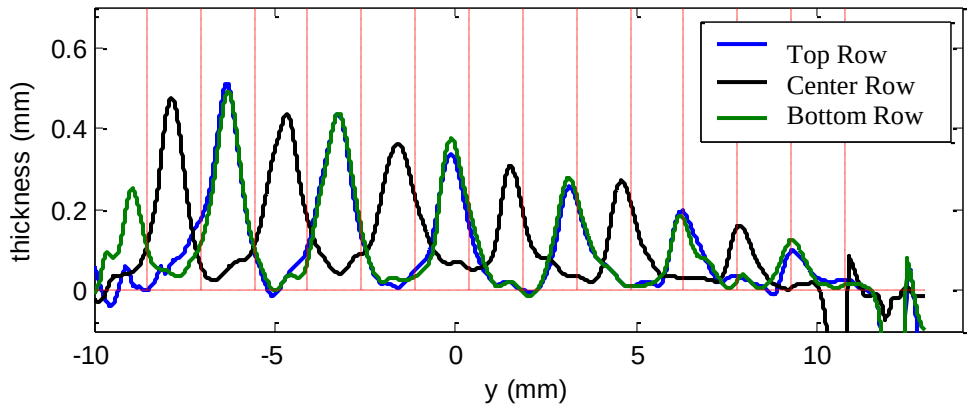

Figure 6.3 – Linear traces of deposit cones from cross flow experiment. Impinging flow exhausts to the right.

A computational grid of this geometry was created using a mixed structured and unstructured grid and a single symmetry boundary plane (1.5M cells). Flow conditions were matched to the experiment: mass flow rate at inlet with constant total pressure, exhausting to ambient. No deposit layers were modeled nor were particles tracked as only an investigation of wall shear was desired. Because no temperature gradients existed and the flow had low Mach numbers, the fluid was treated as incompressible air. The k-ω SST turbulence model was utilized.

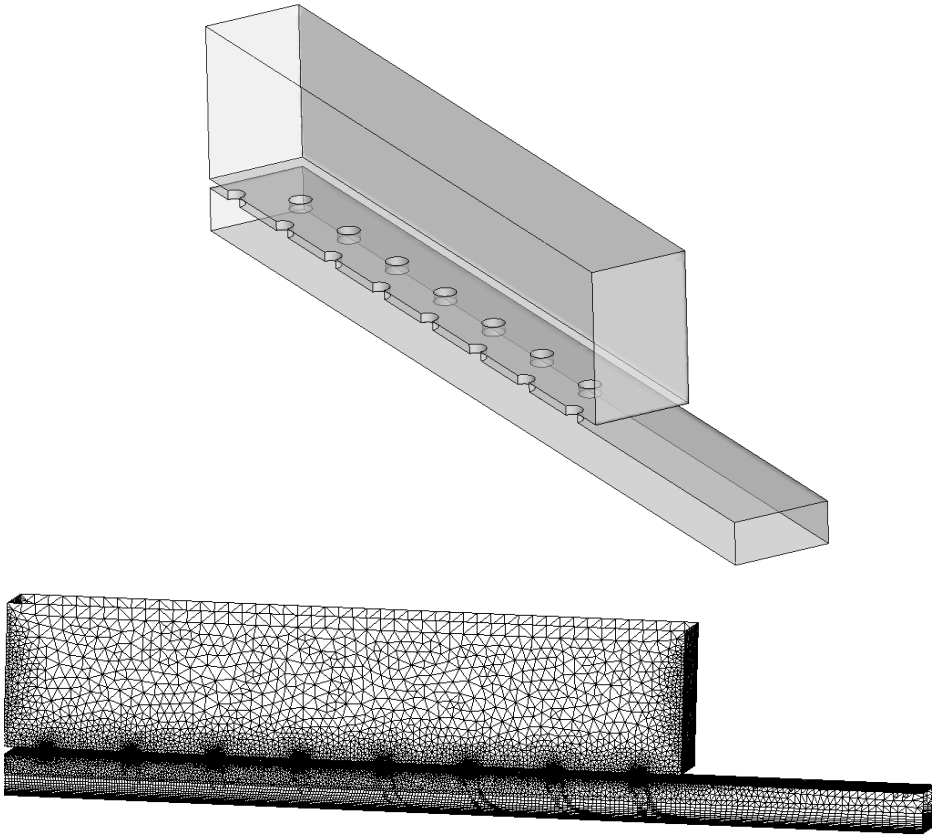

Figure 6.4 – Computational grid of "cross flow" geometry.

Figure 6.5 shows the local shear stress magnitudes on the impact plate surface. The impingement hole locations are marked with black circles for reference. The ring-like markings on the left show the shear stresses induced by the impingement jets that experience little to no cross flow. The regions are characterized by a locale of low wall shear in the center of the jets, surrounded by a ring of high shear. The shear patterns become distorted moving to the right as the jets experience steadily increasing cross flow. From the experiment, deposit initially builds within the rings where the wall shear is lowest. The impacting particles in the right-most jets never impact low shear regions and it is suggested that this prevents the particles from sticking.

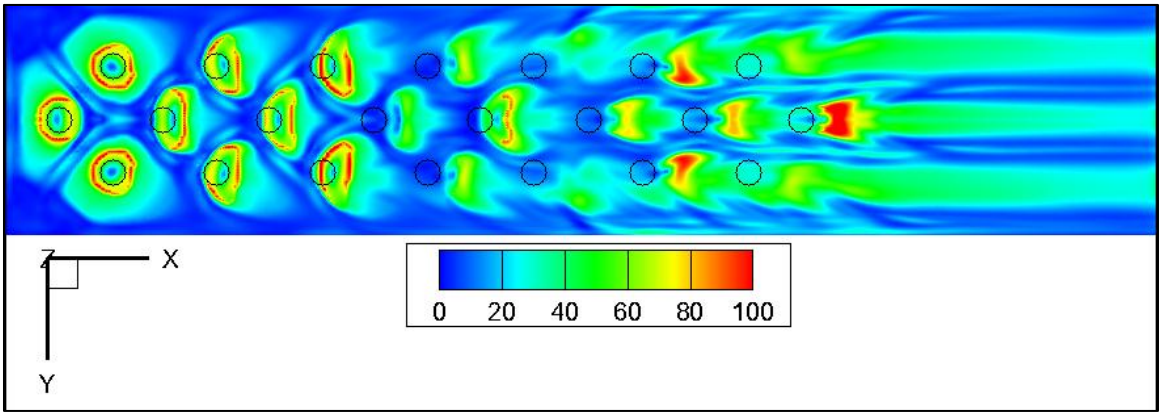

Figure 6.5 – Wall shear stress magnitudes (Pa) on impact plate for "cross flow" geometry. Flow exhausts to the right

Video recorded the deposit formation from the back side of the transparent glass. It revealed that deposit initially was restricted to the low shear regions of the left-most impingement jets without cross flow. Over time, deposit structures grew in the impingement region of the center jets, but never in the right most jets.

The post-test deposit structures that formed in the low cross flow jets were also much larger in height and width than the high cross flow regions on the clean plate. The low shear regions in the left-most jets in Figure 6.5 are similar in size to the diameter of the impingement hole. However, the final deposit structures are about twice as large. This is expected to be because as the deposit structures grow, the low shear regions also expand outward with the modified surface geometry, allowing for broader deposit growth. This is further investigated in computational simulations of single, axisymmetric impingement jets.

The objective of the studies in this paper is to determine the factors that lead to deposition in internal cooling cavities in order to improve the fidelity of the computational model. This experiment with cross flow, despite having a complex flow field that changes with deposit buildup, revealed that deposit buildup has an inverse relationship with the cross flow. It is assumed that this is caused by the increased wall shear on the impact plate for impinging jets with higher amounts of cross flow as well as the reduced, low-shear stagnation regions associated with these jets.

6.2 Shear Investigation on Simulations with Single Impingement Hole

Several simulations were performed on a two-dimensional structured, axisymmetric grid representing a single impingement hole to investigate how shear forces change with surface geometry and contribute to deposit buildup. The simulations use the same hole and gap spacing as the experiments, and same pressures and flow rates for a single hole. However, it includes no interaction effects with other impingement jets, as only a single hole is modeled, and the flow exhausts radially. A representation of the base mesh is shown in Figure 6.6.

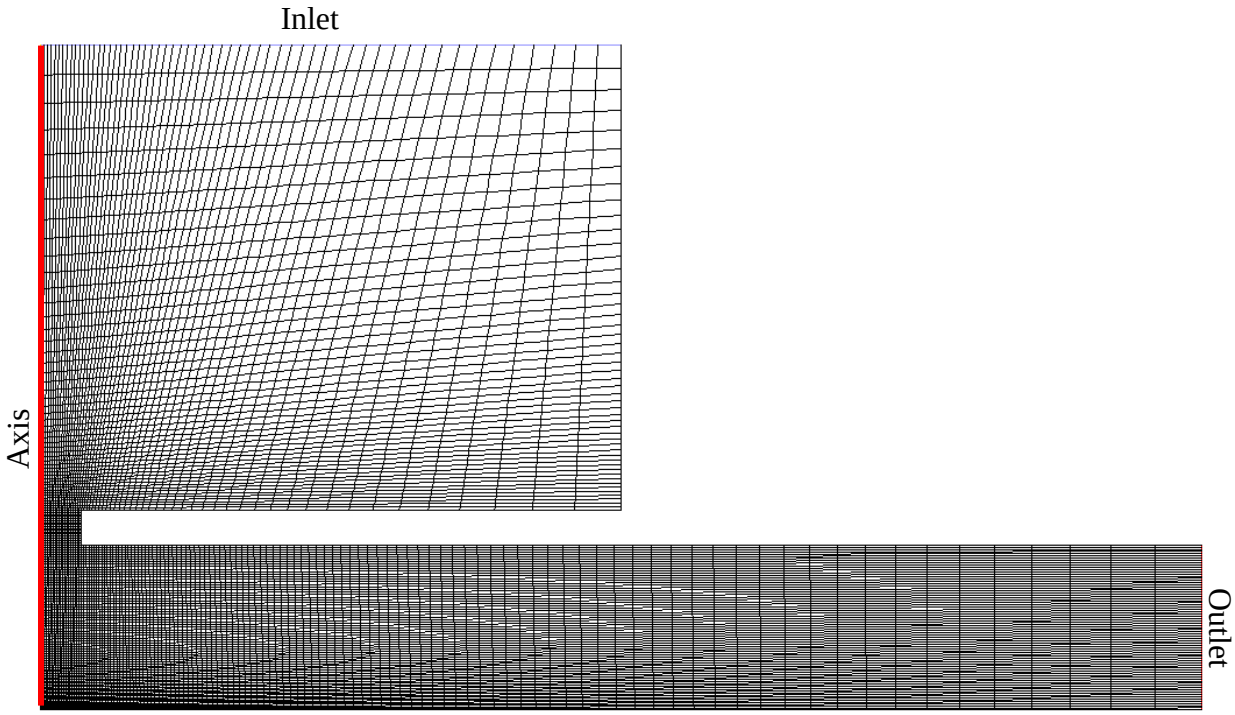

Figure 6.6 – 2D axisymmetric mesh of single impingement hole.

A simulation was run matching the intermediate flow rates through individual holes from the experimental tests ($\dot{m} = 4.6 \times 10^{-4} kg/s$). For simplicity, the flow solutions were run under ambient temperature conditions and the walls were assumed to be adiabatic. This was done as only the shear trends are of interest for these simulations, and effects of temperature are ignored. The wall shear along the impact plate is shown in Figure 6.7, with dashed red lines representing the location of the impingement hole.

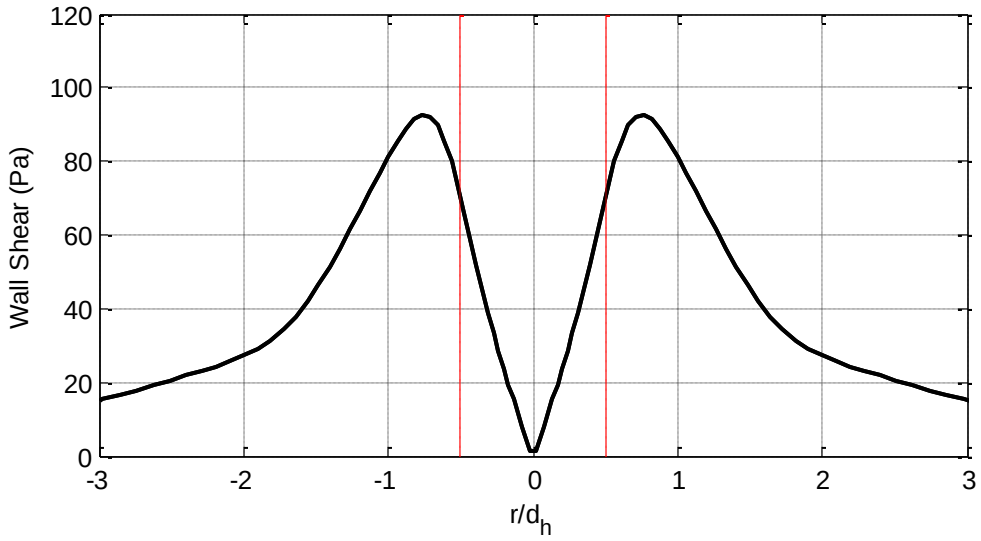

Figure 6.7 – Wall shear by radial position on axisymmetric grid.

The trend is typical of shear from an impinging jet, with shear rates increasing in the radial direction away from the origin, and then diminishing due to a growing boundary layer and flow deceleration due to a growing flow area. This shear trend can be used as a base comparison for other simulations with modified geometries.

The shear stress trends offer valuable insight as to how the deposit structures form in the manner seen in the experiments. With flow impacting a clean plate without any deposit, shear stresses increase in the radial direction from the center until about 0.75 d_h. If a particle impacts this region (and most particles of these Stokes numbers impact the plate within an r/ d_h of 1.0) and the adhesion forces do not overcome the force of fluid shear (ignoring rebounds), the particle will roll or slide along the surface in the direction of the shear, and be re-entrained into the flow or come to rest when adhesion forces dominate. If, for example, shear stress above 50 Pa overcomes adhesion forces on a clean plate and causes particles to roll, then deposit would only build within an r/ d_h of about

0.4, though particles continue to impact within an r/d_h of 1.0. Incidentally, the deposit in the very first time step in Figure 4.8 shows that deposit is restricted to within about $r/d_h <$ 0.4. This figure is recreated in Figure 6.8.

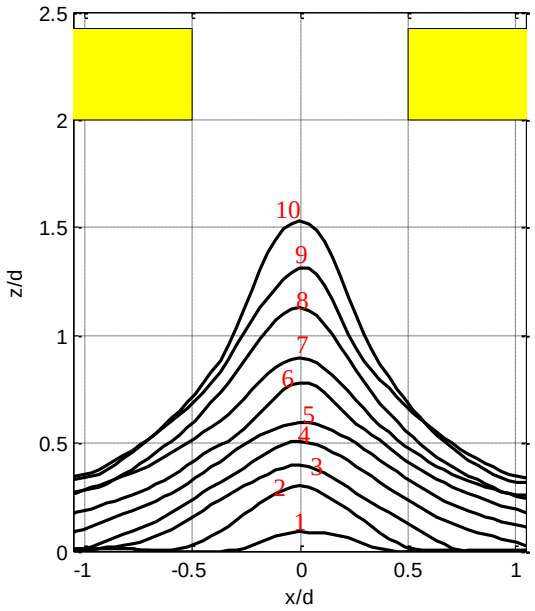

Figure 6.8 – Experimental deposit growth, recreated from Figure 4.8.

6.3 Cones of Varying Height

It was desired to assess the change in wall shear stresses on the surface with preexisting deposit. The geometry was adapted to include ideal triangular cones directly in line with the impingement jet hole. Two sets of simulations were performed, the first of which investigated cones of varying heights but uniform slope. This was done because in some experiments, such as the one in Figure 4.8, on the growth lines from 2-5, the cone slope is relatively uniform. This uniform slope of deposit is not predicted in any of the previously discussed deposition models. These simulations were run to determine whether wall shear might influence deposit structures with constant cone slopes. The

slope for these simulations was chosen to be 0.6 z/r, as this was the general slope for lines 2-5 from Figure 4.8. Cone heights were varied from 0 to 1.8 d_h.

The second set of simulations investigated cones of various slopes and uniform base widths. The width diameter was chosen to be 2.0 d_h, and the cone height was varied from 0 to 1.8 d_h.

The flow parameters for these simulations matched those from the simulation in Figure 6.7. Figure 6.9 shows the results of these simulations, showing the wall shear magnitude by radial distance for several geometries.

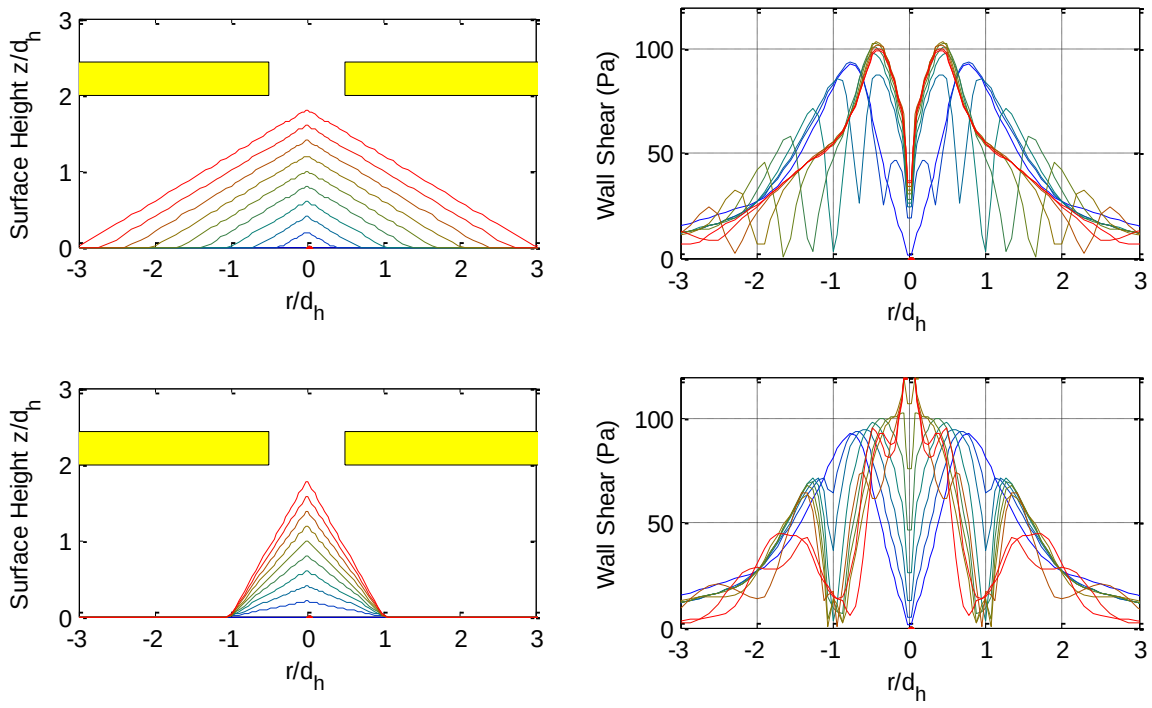

Figure 6.9 – (Left) Cone geometry and (Right) wall shear for deposit cone growth

For cones of constant slope, regions of low shear change with cone growth. Shear minimums are found at the base of the cones, so any dislodged or shear driven particles are likely to accumulate at the base as the deposit grows. Regions of high shear also

change with deposit growth, as the maximum peaks in shear, originally located at r/d_h = 0.75, diminish and move radially outward until a cone height of about z/d_h = 0.4. At this size, the maximum shear is located on the deposit cone itself. This suggests that deposit growth rates may be reduced beyond these sizes. For larger cone sizes, the wall shear on the plate at outer radial positions is also reduced.

The shear at the center peak increases slightly for larger cone sizes. Figure 6.10 shows the wall shear at the radial position near r/d_h = 0 at several cone heights. While for a flat plate this value is 0, the shear at the center increases to values of about 20 Pa for a cone height of z/d_h = 0.3, and increases gradually for larger cones. This figure also shows the area-averaged wall shear within multiple radial positions. The region within $r/d_h < 0.5$ experiences the greatest change, with average wall shear doubling at cone heights $z/d_h >$ 0.3 compared to smaller cone sizes.

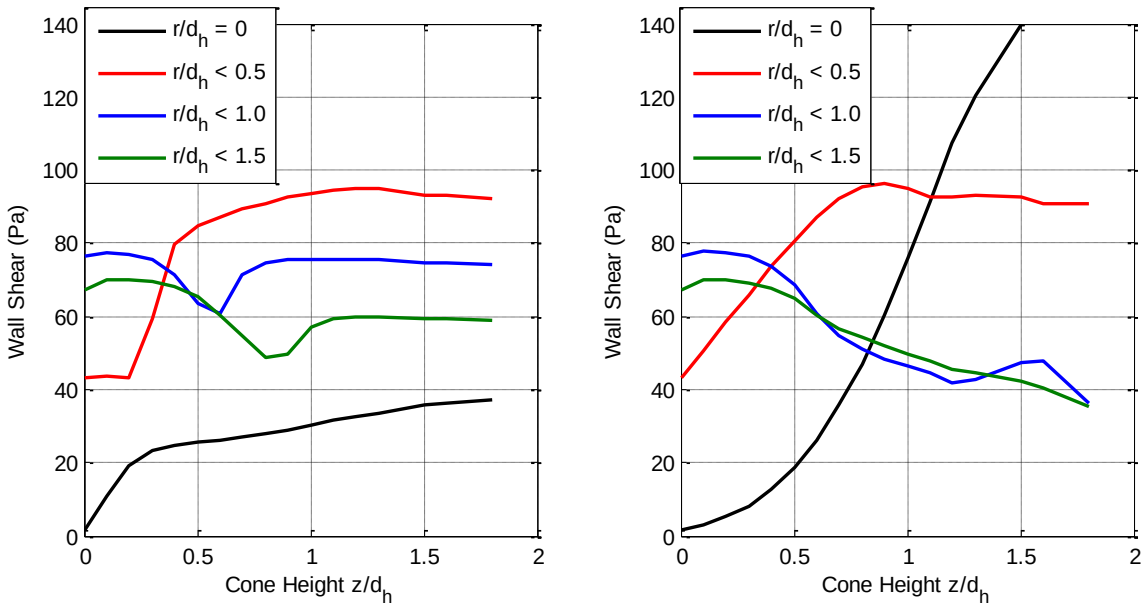

Figure 6.10 – Average wall shear for various radial positions and cones heights for (left) cones of constant slope and (right) cones of constant width

For cones of varying slope and constant base width, there are much more pronounced changes in wall shear. Figure 6.9 and Figure 6.10 reveal that shear forces increase at low radial positions (on the cone) with increasing cone angles. At cone angles above about 45 degrees ($z/d_h \geq 1$), there is no perceived region of low shear in the jet center. Additionally, the wall shear at the center of the jet, on the peak of the cone, continually increases with increasing cone slope. This suggests that when shear is a factor in particle sticking, deposit may not form beyond some critical angle. The shear at low radial positions ($r/d_h < 0.5$) also increases with increasing angle, but levels off at z/d_h above about 0.8. Similar to the constant slope simulations, low shear regions exist at the base of the cones. Particles impacting preexisting deposit, if unable to rebound and shear forces prevent sticking, may roll and accumulate at the base of the cone, broadening the deposit structure even though there is no change in the distribution of particle impacts.

From these simulations of impinging jets on idealized cones, several conclusions can be made that are potentially applicable to deposition modeling. Experiments showed that initial deposit growth occurred at confined radial positions which are also regions of low wall shear. As deposit grows, shear at the low radial positions increase but the shear at the base of the cone decreases. If shear plays a role in particle sticking and transport, then this would explain why the deposit cones grow both upward and outward.

6.4 Insensitivity of Upstream Flow Field to Deposit Growth

It was observed in the three-dimensional simulations that the particle impact (and subsequent sticking) locations did not change much with the growth of the deposit. This was further investigated on the axisymmetric simulations with idealized deposit cones. Figure 6.11 shows velocity magnitude contours from the flow simulation for both the

baseline geometry and the cone with a height of $z/d_h = 1$. For these flow solutions, the flow upstream and at the impingement hole are nearly identical.

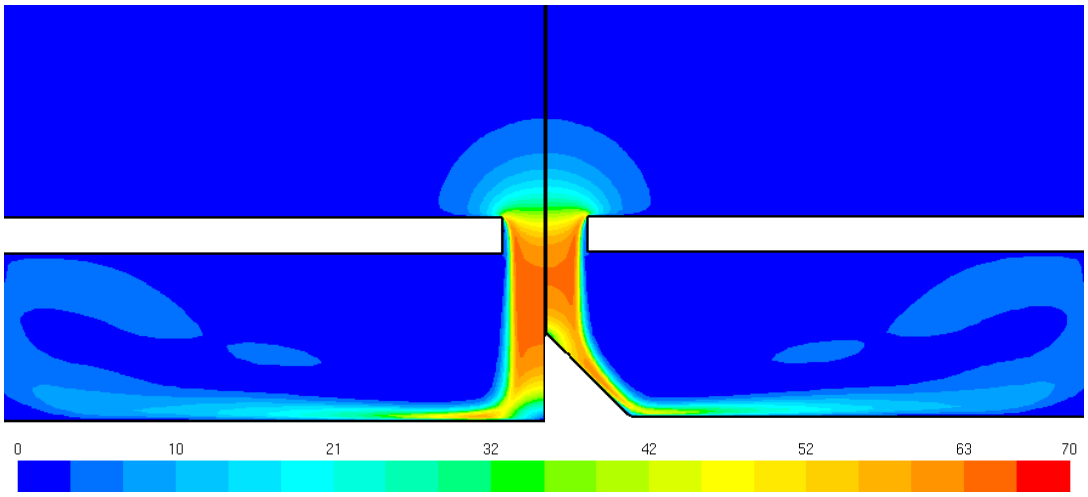

Figure 6.11 – Velocity magnitude contours (m/s) of flow through single axisymmetric impingement hole for (left) baseline geometry and (right) geometry with deposit cone of height $z/d_h = 1$.

Because the flow is nearly identical upstream of the deposit cones, it is expected that particle trajectories will not vary prior to initial impacts. This is confirmed in Figure 6.12, showing particle trajectories from the two cases. The trajectories represent particles of 7 µm diameter corresponding to a Stokes number of 36.7. As expected, the particle trajectories are nearly identical. The aerodynamic focusing of particles is also well represented where particles all cross the axis at nearly the same point. (For these trajectories, turbulent diffusion using the random walk was not employed in order to better compare the two geometries. If the random walk were applied, the trajectories would be more irregular and the particles would be more dispersed through the orifice, but the mean distributions would not change.)

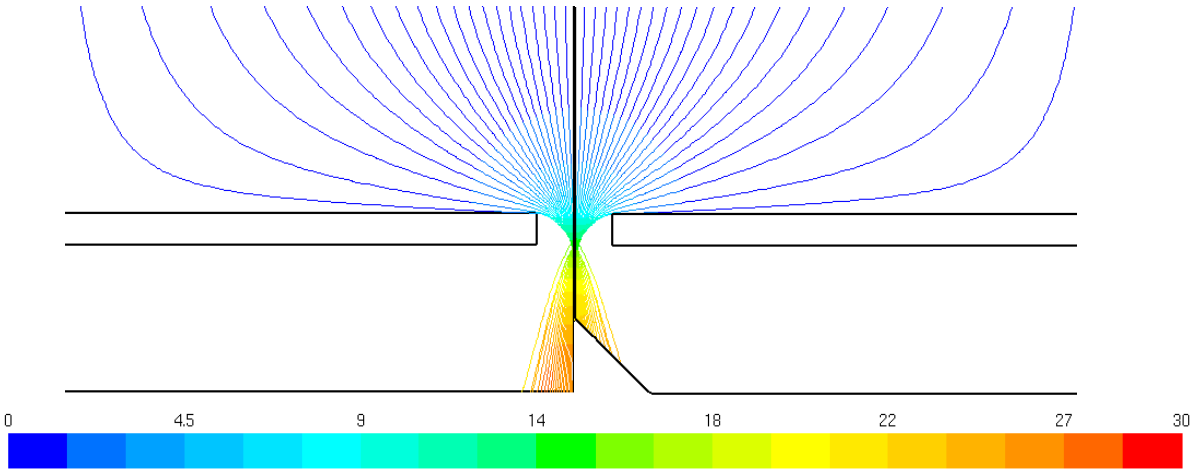

Figure 6.12 – Particle trajectories of 7 μm particles through single axisymmetric impingement hole for (left) baseline geometry and (right) geometry with deposit cone of height $z/d_h = 1$. Contours are particle velocity in m/s.

6.5 Shear-based Sticking Model

Another set of tests were run utilizing a deposit growth technique with a shear-based sticking model on the 2D axisymmetric grid. Instead of tracking particles individually, a distribution function was taken from the statistics of previous computations. Figure 5.3 and Figure 5.4 show the relative particle flux through the impingement jets for various z-planes, ignoring any rebounds, from the hole-array geometry. This mass flux distribution was simplified to a Gaussian distribution. From the particle flux data it is seen that the particulate distribution is focused at the exit of the impingement hole and then disperses in a nearly linear fashion approaching the impact plate. The assumed particle flux through the hole geometry is defined as

$$J = C_J \frac{1}{(\sigma/d_h)^2} e^{-\frac{(r/d_h)^2}{2(\sigma/d_h)^2}} \qquad [\,6.1\,]$$

σ is the distribution standard deviation and is dependent on the surface growth height, defined as

$$\boldsymbol{\sigma = \frac{d_h}{2} - \frac{1}{8}\frac{z}{d_h}} \qquad \textbf{[6.2]}$$

It should be noted that in the Gaussian distribution, the magnitude is inversely proportional to the square of the standard deviation, as the flow is axisymmetric and requires the exponent to maintain constant flux. C_J is an arbitrary constant to define the amount of particulate growth at each time step. Prior computations also revealed that particle trajectories do not differ significantly due to the presence of deposit cones. Particles passing through the orifice holes accelerate to high velocities and therefore have high Stokes numbers, indicating that their subsequent trajectory is ballistic. The pressure and mass flow near the impingement hole is not sensitive to the deposit height unless the cones are taller than 1.8 $d_{h.}$ As the particles in these simulations are tracked in bulk, rebounds and multiple impacts are ignored.

A sticking model was created that assumes that particle sticking is entirely based on wall shear. Two critical values of wall shear are assumed, τ_{min} and τ_{max}. If the wall shear is below τ_{min}, all particles are assumed to stick upon impact, whereas if the wall shear is above τ_{max}, none of the particles are assumed to stick. If the shear falls between, then the amount that sticks is given by the ratio

$$\boldsymbol{Sticking\ Efficiency = \frac{\tau_{wall} - \tau_{min}}{\tau_{max} - \tau_{min}}} \qquad \textbf{[6.3]}$$

This is illustrated in Figure 6.13 using the same wall shear values from a clean surface from the simulations in Figure 6.9.

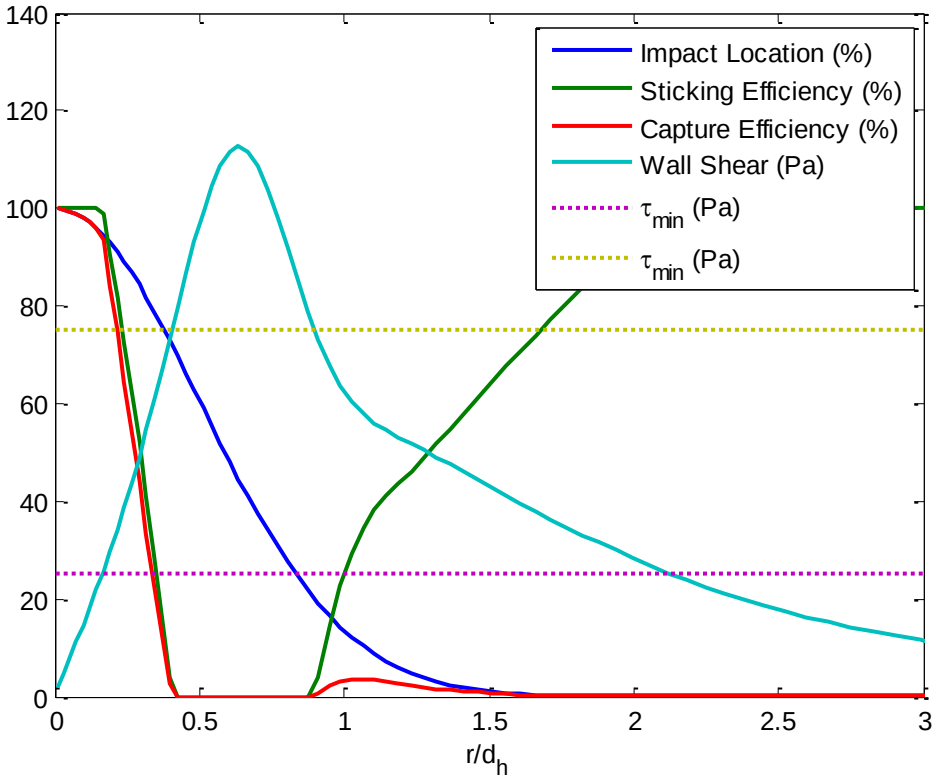

Figure 6.13 – Sticking efficiency based on wall shear

If the particles do not stick, they are assumed to roll along the surface in the direction of the shear. If the shear decreases below a specified value, the particulate is assumed to deposit in that location. For these simulations, the specified value for sticking is assumed to be a linear function of the distance a particle needs to roll to reach that location. In other words, if a particle must roll a long distance before reaching a location of low shear, it is more likely to become re-entrained in the flow and leave the surface. The shear function for reattachment is given as

$$\tau_{reattach\,max} = \tau'_{max} - C_\tau \frac{\Delta r}{d_h} \qquad [\,6.4\,]$$

$$\tau_{reattach\,min} = \tau_{min} - C_\tau \frac{\Delta r}{d_h} \qquad [\,6.5\,]$$

C_τ is an arbitrary slope with an assumed value of $0.5\tau_{max}$.

τ'_{max} is the maximum shear for which particulate has not previously deposited. To illustrate this, consider the following diagram.

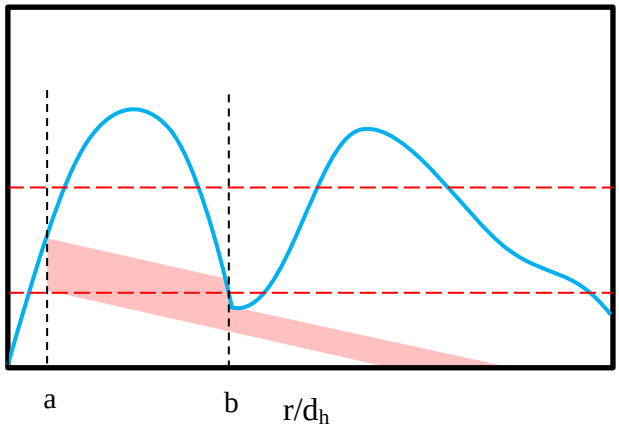

Figure 6.14 – Diagram showing particle reattachment in low shear

In this theoretical scenario, consider the particles impacting at point 'a' with the theoretical wall shear curve given by the blue line, and the wall shear limits given by the dashed red lines. As this point is about halfway between the shear limits, 50% of the particles are assumed to stick. It is assumed that only the "least sticky" roll away in the radial direction due to shear, so a wall shear less than that of the initial impact location is required for these particles to come to rest. The upper and lower bounds of the transparent pink region represent $\tau_{reattach\,max}$ and $\tau_{reattach\,min}$, respectively, with the slope of the region representing C_τ.The value τ'_{max} is the maximum shear value of particles that have not yet stuck, and in this case is halfway between τ_{max} and τ_{min}. For the particles that impact a location where $\tau_{wall} > \tau_{max}$, then $\tau'_{max} = \tau_{max}$.

The particles roll radially until they reach point ‘b’, where the low shear allows about half of the particles (one-fourth of the total) to attach to the surface. (Because the particles move in the radial direction, the potential “thickness” of particulate decreases in order to maintain constant mass) The remainder of the particles continue to roll, and as no regions are encountered with sufficiently low shear, the particles are assumed to escape without sticking.

This method utilized an iterative technique to modify the geometry of the surface to determine changes in wall shear and deposit buildup. Each iteration simulates the injection of 0.003 grams of particulate matter, relative to the particle loading from the experiments. This represents 0.12 milligrams of deposit through an individual impingement hole per iteration. After each iteration, the geometry of the CFD mesh was modified and the wall shear was recalculated. The surface geometry across 60 iterations is shown in Figure 6.15. For this simulation, τ_{max} and τ_{min} are assumed to be 75 Pa and 25 Pa, respectively.

Deposit forms as an isolated cone directly beneath the impingement hole. The cone forms quickly during the initial iterations, indicated by the red lines, but the growth rate decreases and the deposit structure approaches a steady-state curve in Figure 6.15. At this curve, the wall shear stress is nearly equal to τ_{max} for the entire region of particle impacts, as shown in Figure 6.16. Because a majority of the particles impact within $r/d_h <$ 1.0, and the wall shear is near or above τ_{max} , very little growth occurs beyond this point.

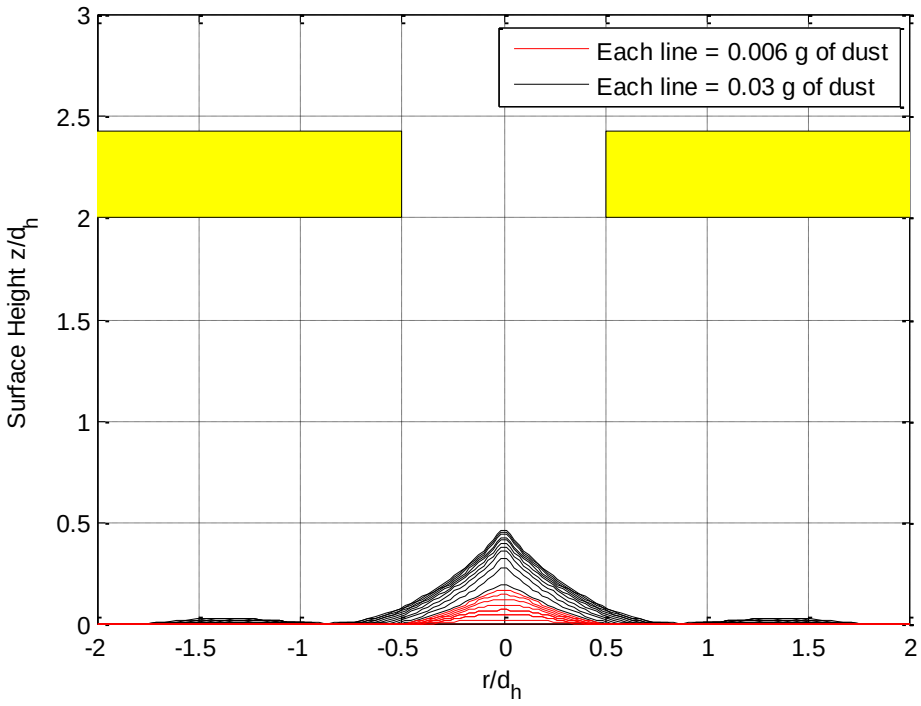

Figure 6.15 – Transient surface growth from shear-based sticking model

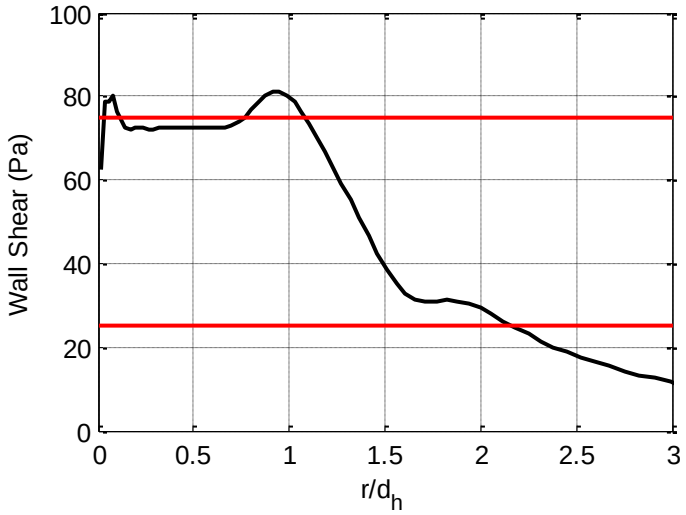

Figure 6.16 – Wall shear for final geometry in deposit growth simulation

While differences certainly exist compared to the experimental tests, this model does predict deposit growth trends not seen in other computational models. First, the deposit cone is initially restricted to low radial positions within $r/d_h < 0.5$, resembling lines 1 and 2 in Figure 4.8. Over time, the cone grows slightly upward and outward. The second similarity is that the cone slope remains relatively unchanged as it grows larger, just as the slopes remain relatively unchanged in lines 2 through 7 in Figure 4.8. This simulation also predicted deposit growth as a sharpened peak at the center, in agreement with experimental observations, whereas prior simulations showed deposit growing as rounded mounds.

Another feature of the deposit growth occurs at locations $1.2 < r/d_h < 1.5$. Very few particles impact at these locations, but buildup is still predicted. This region represents very low wall shear as the radial flow experiences an adverse pressure gradient. Particles that impact at lower radial positions, but don't stick due to high shear, move radially outward and are recaptured.

The values for τ_{max} and τ_{min} were chosen arbitrarily for the previous simulation, which suggested a maximum allowable growth. In order to determine how deposit grows beyond what was previously seen, the simulation was repeated assuming larger values for τ_{max} and τ_{min}. This was done to prevent the deposit structures from reaching a steady-state. The new assumed values were chosen to be 100 Pa and 50 Pa, and the results from 60 iterations are shown in Figure 6.17.

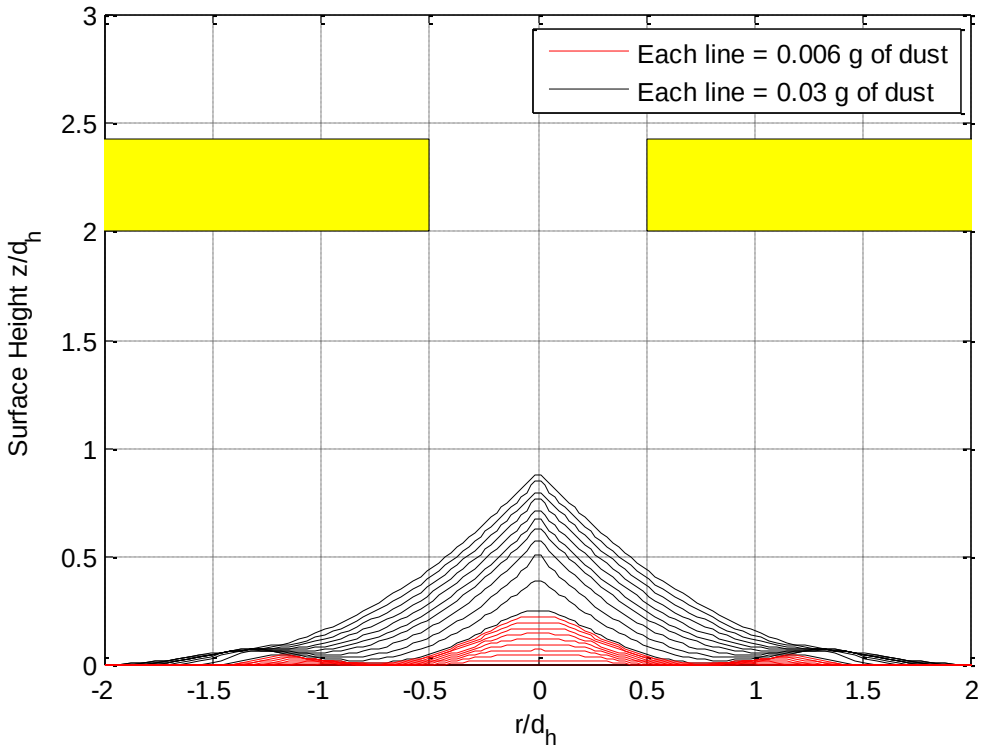

Figure 6.17 – Transient surface growth from shear-based sticking model with modified sticking criteria.

These deposit growth trends more closely match what was seen in the experiments. In addition to the initial growth at radial positions within $r/d_h < 0.5$, it also shows the deposit structure broadening to large radial positions. For this simulation, the base of the cone extends beyond $r/d_h = 1.5$, and would be expected to grow larger if the simulation were extended. It should be noted that this simulation involves the geometry of a single hole, and the experiments represented an array of holes. The holes are spaced about three hole diameters apart, so a radial distance of $r/d_h = 1.5$ would be the midsection of two adjacent deposit structures. For an actual impingement jet array, the wall shear, and consequently the deposit buildup, would be affected by the interaction of

adjacent impingement jets. At the midsection between two jets, the wall shear diminishes to zero, as the flow separates from the wall. It is expected that this area would be susceptible to deposit growth. This was seen in some low-temperature experiments that experienced the "ridge" deposit formations.

6.6 Array Simulations

Another set of computations were performed with the intent to account for the low shear region in between impingement jets. To accomplish this, a boundary condition was manipulated to partially simulate the interaction effects of an impingement array on a 2D axisymmetric mesh. The mesh utilized the same base geometry as the 2D axisymmetric mesh discussed previously. However, the wall shear should approach zero at the midpoint between holes, though this cannot be modeled using an axisymmetric grid, at least not physically.

The new grid (Figure 6.18) contains the same axis as before, but utilizes an outlet boundary at a radial distance of r/d_h = 1.66 (the average distance between holes in all directions on a square-patterned array with s/d_h = 3). The outlet utilizes an "outlet vent" condition as defined by Fluent. The outlet vent acts as a regular static pressure outlet but the pressure at the boundary is influenced by the velocity of the flow passing through it. The pressure is defined as

$$\boldsymbol{P_{out} + \frac{1}{2} k_L \rho_f V_n^2} \qquad \textbf{[6.6]}$$

P_{out} is the outlet pressure, set to ambient. V_n is the normal velocity passing through the boundary and k_L is a user defined loss coefficient. For these studies, k_L was given a value of 200. The effect of this boundary condition and loss coefficient is that the flow moving radially outward experiences a strong adverse pressure gradient near the

wall, causing the flow to separate and jet away from the wall, nearly parallel to the outlet. While this is not the same flow field as experienced by an array of jets, it does provide the low shear region without requiring a 3-dimensional simulation.

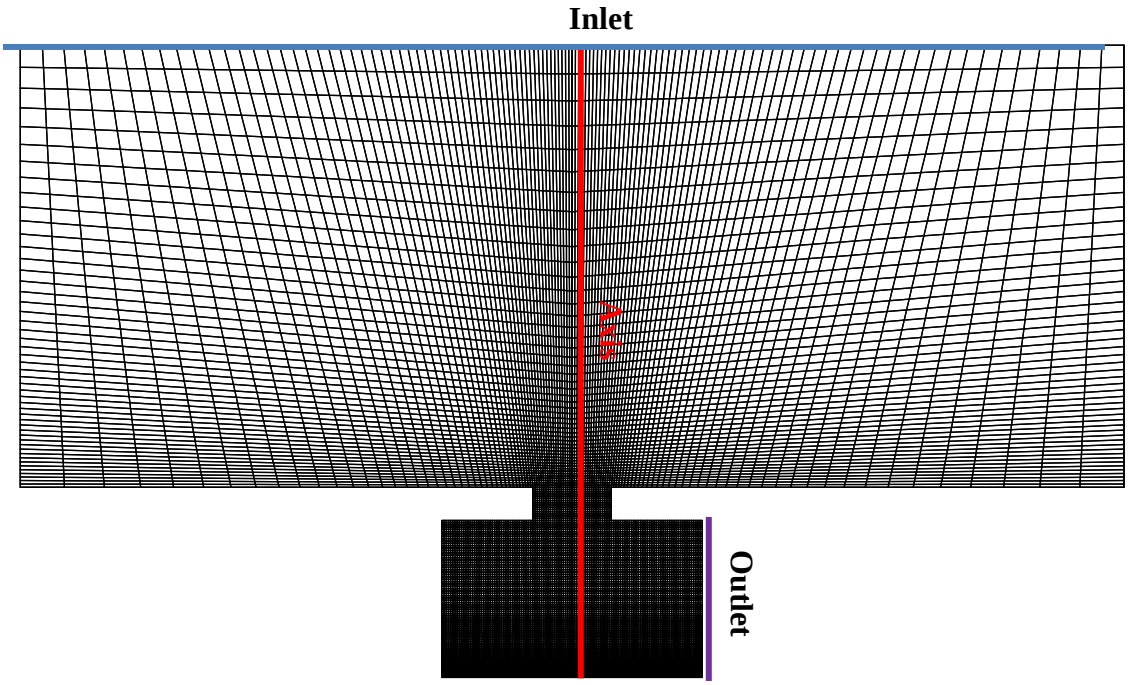

Figure 6.18 – Mesh for 2D axisymmetric impingement hole with outlet "vent" boundary condition

To illustrate how this better matches the flow field, Figure 6.19 shows the velocity comparison of the x-z planes for the 3D geometry at y = 0 and flow velocity for the single hole under identical positions. In both cases, the jet impinges on the surface with nearly equal centerline velocities, and flow moves radially outward from the jet center close to the wall. On the 3D geometry, the flow is diverted upward due to the symmetry plane, and flow then moves out of plane. For the axisymmetric case, the new outlet boundary condition causes the flow to recirculate in a similar fashion. While the

recirculating flows are not identical in form, this does provide a low shear region at the boundary without requiring a three-dimensional geometry.

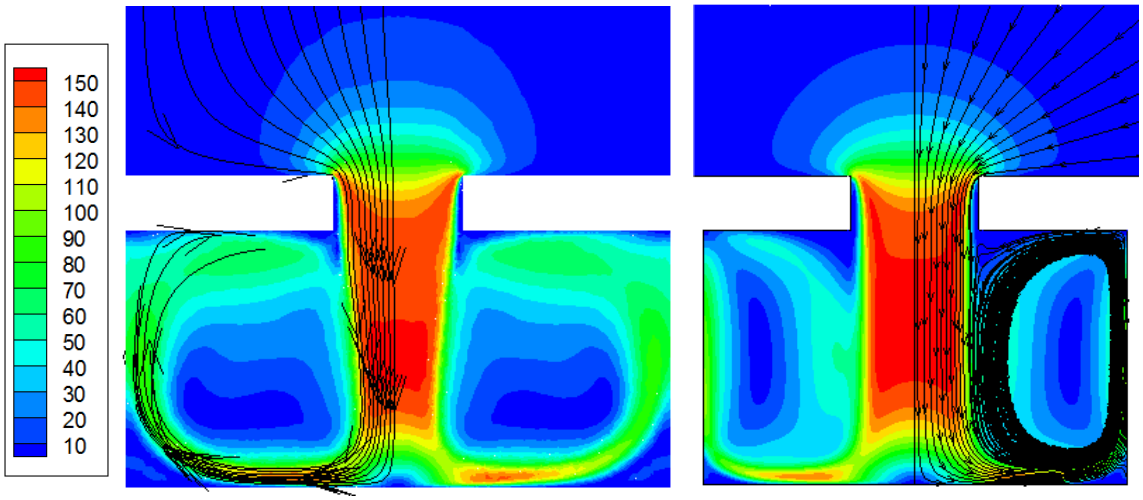

Figure 6.19 – Comparison of x-z planes of flow velocity magnitude (m/s) for (left) 3D geometry and (right) 2D axisymmetric boundary condition with "vent" outlet.

The same sticking method as before was applied to model deposit buildup, with τ_{min} and τ_{max} equal to 50 Pa and 100 Pa, respectively. The results from several iterations are shown below, with each black line representing 0.059 grams of injected dust, relative to the experimental tests. The simulation was run for 110 iterations, simulating the injection of 0.65 grams of particulate in the experimental geometry.

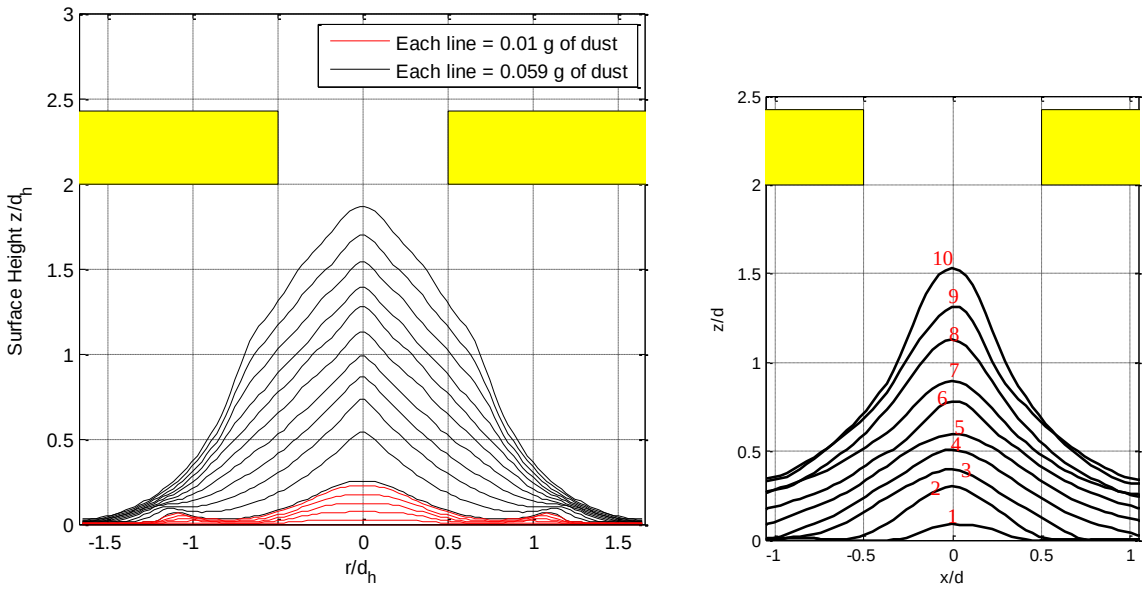

Figure 6.20 – (left) Deposit buildup on 2D axisymmetric grid with outlet boundary conditions that simulate an impingement jet array and (right) experimental deposit growth, recreated from Figure 4.8.

Like the last simulation, growth initiates within $r/d_h < 0.5$. A layer of deposit also forms at $r/d_h = 1.1$. This represents the flow separation region where local wall shear changes signs and flow separates, similar to what is seen in some of the experiments. As the deposit cone grows, the center cone eventually merges with the buildup at the far radial positions. After the deposit structure grows to a height of about $z/d_h = 0.5$, the deposit grows upward at nearly a constant rate and constant cone slope, similar to lines 2 through 7 in Figure 4.8. Unlike prior simulations without the vent outlet, the cone continually grows upward until nearly penetrating the orifice.

Experiments showed that for some deposit structures with high rates of sticking, the growth rate accelerated when the cone height exceeded about $z/d_h = 1.0$. While this simulation did not experience this acceleration to the same degree, the growth rate does accelerate at later time steps. The growth is predominantly within radial positions of r/d_h

< 0.6, and beyond a certain height, it was observed that fluid flow separated from the deposit structure at this radial position and the jet no longer impacts the impact plate. This separation ensured that the cone continued to grow at low radial positions while at the same time prevented accelerated buildup at higher radial positions.

In the experiments, the accelerated growth peaks were restricted to lower radial positions, typically narrower than the orifice hole diameter (see Figure 6.21). While different in size, these simulations suggest that the deposit structures may cause the impingement jet to separate prior to ever reaching the impact plate.

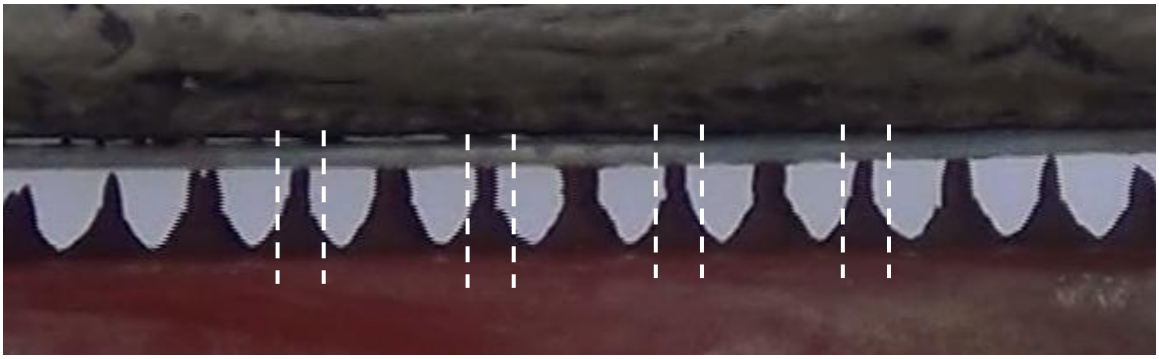

Figure 6.21 – Experimental video image from test 8 (low flow rate, high temperature, with flame heating) at 90 second mark showing accelerated growth peaks. White lines indicate diameter of impingement holes.

6.7 Shear-based Sticking Model Trends

These above simulations were done utilizing a shear-based sticking model, independent of variables like temperature, particle size, impact velocity, or chemical composition. While these simulations show the same evolution of particle buildup seen in the experiments with a shear-based model, it should not be concluded that these other

factors do not have any effect. In the context of a shear-based sticking model, it is expected that factors such as particle size, temperature, and chemical composition all affect the amount of shear that particles are able to withstand and remain attached to a surface. The values τ_{max}, τ_{min} and other values in the sticking model were chosen arbitrarily, albeit within the shear rates observed, but in practice represent a particle's resistance or propensity to stick. It is expected that, as previous models and studies suggest, any of these factors can affect a particle's propensity to stick, causing the values of τ_{max} and τ_{min} to be functions of such factors. These can certainly be modified to be dependent on other variables.

At this point the agreement of the shear-based sticking model and the experiments is qualitative. The experiments showed different forms of deposit growth based on flow rate and temperature. Lower flow, higher temperature tests experienced fast growing, narrower deposit cones. It is beyond the scope of this work to match trends to experimental data, as many more experimental tests would be required. However, it is seen in the experiments of this work, as well as multiple datasets on external deposition, that higher temperatures cause particles to become more likely to stick to solid surfaces. It follows that increased values of τ_{max} and τ_{min} would correspond to higher particle temperatures, and vice versa. Much can be learned by investigating the trends in deposition buildup when τ_{min} and τ_{max} are modified. Two simulations were run with identical flow conditions as the simulation in Figure 6.20. However, the values of τ_{min} and τ_{max} were reduced to 25 and 50 Pa for the first simulation and increased to 75 and 150 Pa for the second. These two tests represent a "less sticky" and a "more sticky" case compared to Figure 6.20, and results from the two tests are shown in Figure 6.22.

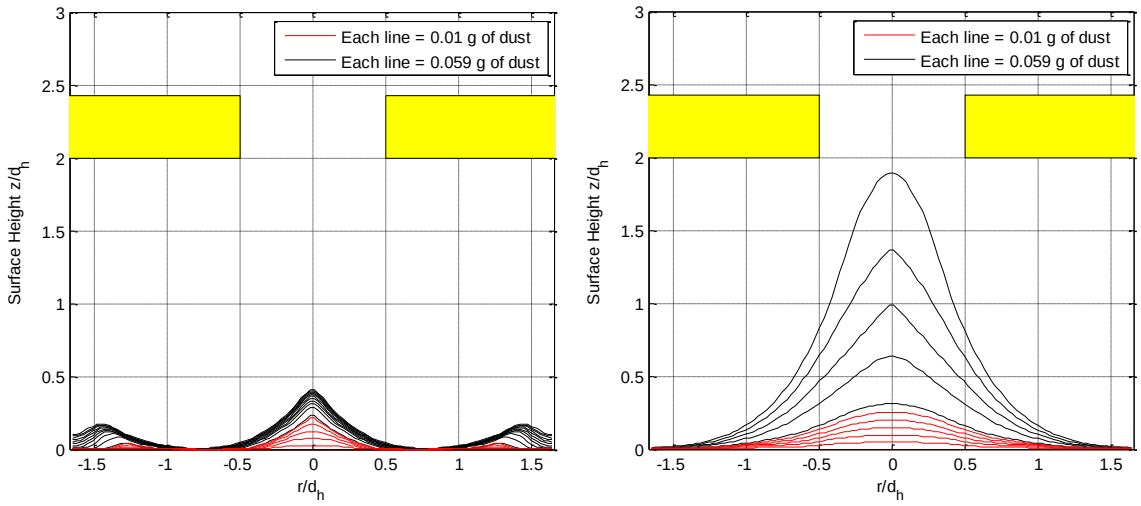

Figure 6.22 – Deposit buildup on 2D axisymmetric grid with particles (left) less and (right) more susceptible to deposition in shear-based sticking model

The first "less sticky" case shows deposit structures similar to low temperature experimental tests (Compare to Figure 4.4 and Figure 4.5). Small cones form at the center relative to the impingement jet but quickly reach a steady state. Because of the reduced sticking criteria, particles that impact the surface are pushed radially outward and accumulate near the outlet boundary, which for this simulation represents the flow separation region between adjacent impingement jets. As few particles stick at low radial positions, the potential for buildup at the separation region is increased.

The second, "more sticky" case saw highly accelerated growth. Like prior simulations, initial growth is largest at low radial positions, but not to the same extent as other simulations. As nearly all particles are expected to stick, the growth pattern resembles a Gaussian distribution as defined by the particle impact function in eqn. 6.1, with accelerated growth at low radial positions as the structure grows upward.

The buildup at higher radial positions is absent in this case as few particles are transported outward by high shear, due to particles already sticking. This simulation also illustrates, like the experiments, the accelerated deposit growth due to the aerodynamic focusing of the particles.

A very similar trend occurs when modifying the flow rates through the orifice. For higher flow rates, the shear is also increased and deposit growth is reduced, and the opposite is true for lower flow rates. Figure 6.23 shows the results of two simulations run with the original sticking coefficients ($\tau_{min} = 50$Pa, $\tau_{max} = 100$Pa) but with flow rates matching the low and high cases from the experimental tests, $\dot{m} = 2.3 \times 10^{-4} kg/s$ and $\dot{m} = 6.9 \times 10^{-4} kg/s$, respectively.

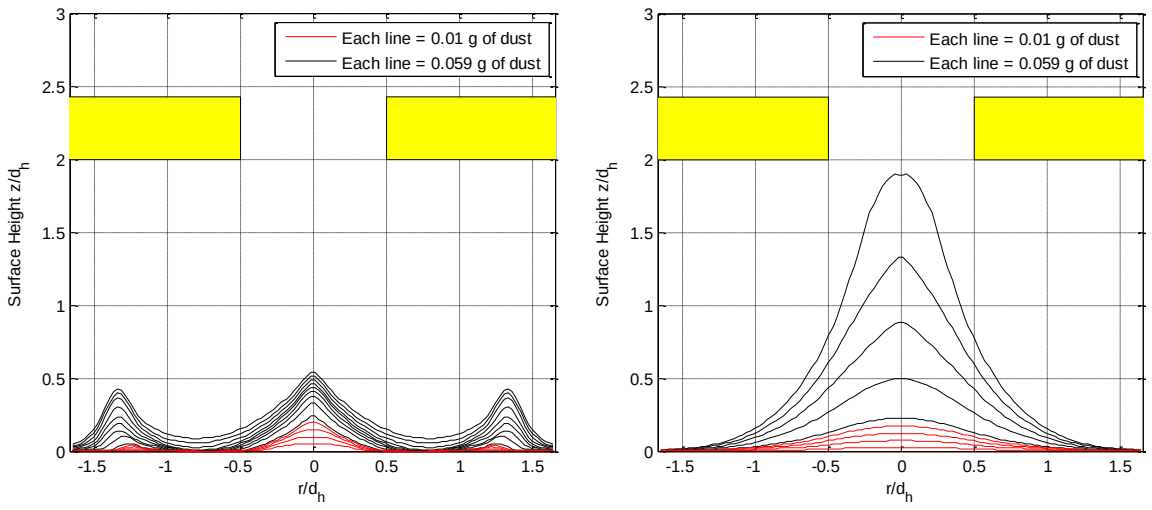

Figure 6.23 – Deposit buildup on 2D axisymmetric grid at (left) high fluid flow rates and (right) low fluid flow rates using shear-based sticking model

The deposit growth trends in Figure 6.23 closely match those seen in Figure 6.22, The high flow and high shear case allows only a minimal amount of deposit growth in the impingement jet region, while also promoting deposit growth at higher radial positions.

Alternatively, the low flow and low shear case has very high capture efficiency rates and the deposit structures grow until spanning the entire gap length. The simulation deposit trends using the shear-based sticking model match those seen for experimental tests regarding flow rates and temperature, which is assumed to be proportional to the stickiness of the individual particles.

In Figure 6.22 and Figure 6.23, the low velocity and increased "stickiness" simulations show deposit growth near the outlet boundary, but deposit thickness at the boundary (r/dh = 1.66) is minimal. As this outlet plane represents the mid-plane between two jets, these simulations are actually predicting two "ridges" of deposit between adjacent impingement jets, as opposed to only a single ridge seen in the experimental tests (Figure 4.4). This is explained by a few factors. The computational outlet boundary is not an exact representation, but only a simplified model of the interface, as the necessarily three-dimensional flow field cannot be precisely represented on the axisymmetric grid. For this reason the wall jets approaching the boundary experience a strong adverse pressure gradient and separate from the wall prior to reaching the boundary. This separation causes a counter-rotating region near the wall and outlet (lower corners of Figure 6.19). At the separation region, the wall shear is zero, and the sticking model collects any shear driven particles at this point. For this reason, little buildup is expected at the actual boundary.

However, this recirculating region is also observed in the three-dimensional geometries, and the shear model would likely predict a double ridge of deposit if applied. It should be noted that the shear-driven particles in this model were not treated as having inertia, but only assumed to stick when the wall shear fell below a particular value.

Applying inertia to these particles would push the region of deposit growth more toward the mid-plane.

Another variable is the transient nature of the wall jet. As the two-dimensional computational model defined the mid-plane as a constrained boundary, and all computational models utilized RANS flow solutions, the wall jet was confined to a single location. In reality, the wall jet may oscillate about an average mid-plane due to fluctuations in the flow, and this would also allow shear driven particles to accumulate as a single ridge along the mid-plane.

The shear-based criteria for sticking show deposit growth trends for multiple types of deposit buildup, not predicted by any other sticking model. The shear-driven particles by this model act to broaden the base of the deposit cones, sharpen the peak, and in the case of high velocity or lower temperature (lower sticking propensity), form the deposit structures at locations between impinging jets.

6.8 Relevance to Former Studies

Unlike the experiments and computations in these studies, the experiments in [36] and [37] only occasionally observed deposit growth as individual cones associated with impingement jets, but rather as deposit ridges that formed between adjacent impacting jets. Figure 1.5 is recreated in Figure 6.24, showing the results of these studies and that deposit formed predominantly between impingement jets instead of at the stagnation region of the jets. In the figure from Cardwell et al., figure (a) represents a test at low temperature (deposit ridges formed, as seen in low sticking from shear-based model) and test (b) represents high temperatures and shows the typical deposit cones. The figure from Land et al. represents tests that were all run at higher flow rates (higher shear) and show

only the deposit ridge formation. These deposits cannot be predicted computationally without accounting for shear in particle sticking, as particles are not expected to impact in these regions through general particle tracking methods. The shear-based sticking model, in conjunction with grid adaptation, therefore provides a justification for different forms of particle buildup.

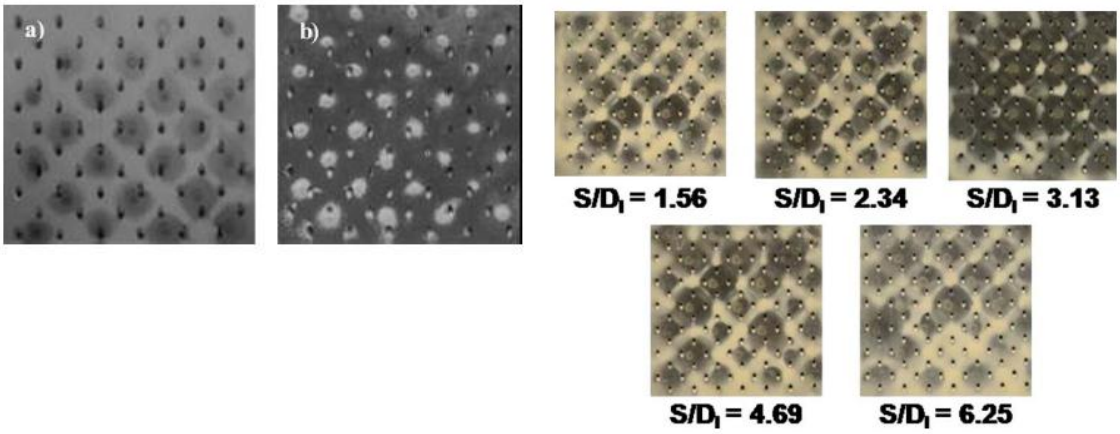

Figure 6.24 – Deposition patterns on upstream film cooling plates from (left) Cardwell et al. [36] and (right) Land et al. [37]

6.9 Relevance to External Deposition

From the previous discussion of wall shear, it is suggested that shear also plays a role in particle sticking at higher external temperatures. In the experiments in this study, particles remain well below the material melting temperature, and it is not expected nor observed that particles fuse or sinter together. The deposit structures that form can be easily ground to dust, nearly identical in form to the pre-test dust. For external deposition, the temperatures are much higher so that the deposit particles experience higher rates of sintering or melting. Particles that impact are more likely to irreversibly fuse into the

agglomerate of deposit. For these reasons, it is expected that higher shear forces would be necessary to influence external deposition rates compared to the internal tests discussed previously.

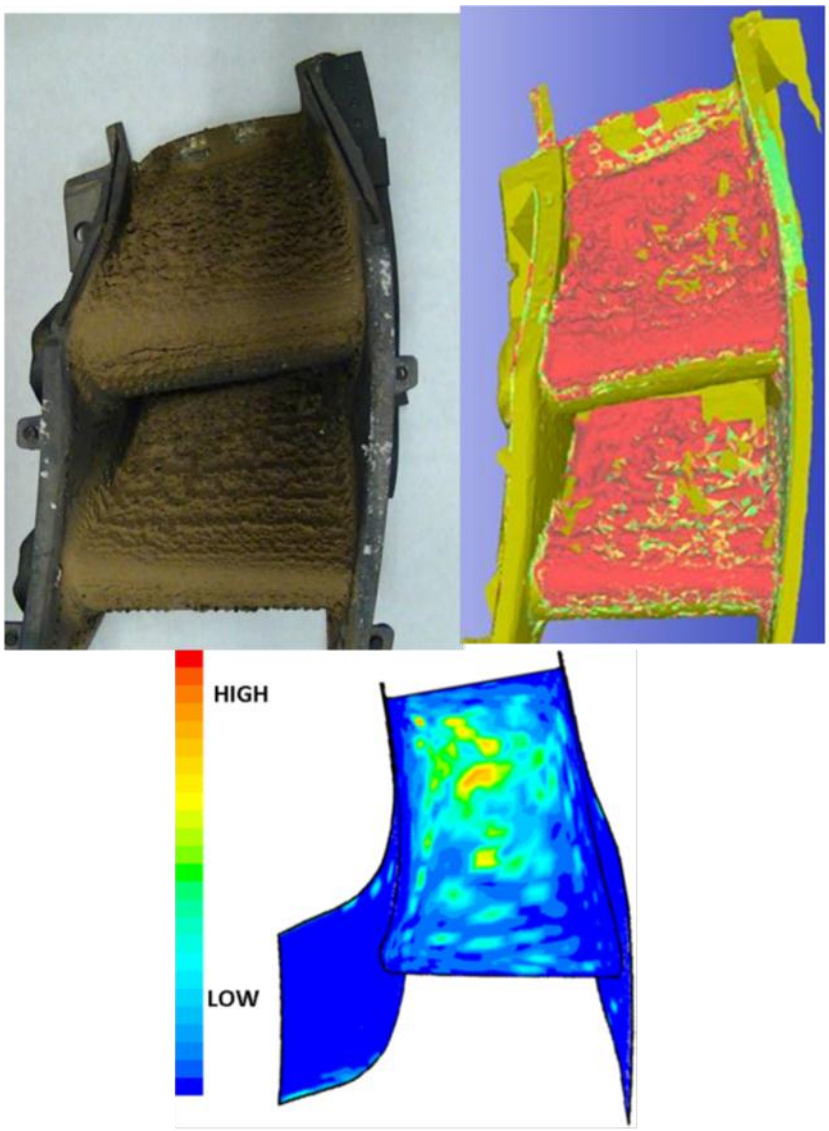

Figure 6.25 – Post-test photograph of external deposition and optical scan from [48]. (bottom) Computational prediction from [38].

Figure 6.25 shows deposition results from one of the tests in [48], with the accompanying computational prediction from [38]. While there were general agreement

with the deposition locations and rates in these studies, two discrepancies were that the computational model under-predicted deposition at the leading edge and over-predicted deposition at the trailing edge of the pressure surface. This discrepancy is also seen in the studies of [51] (Refer to Figure 5.6). While deposition did form experimentally at the trailing edge of the pressure surface, computations consistently over-predicted deposition in this region, potentially by orders of magnitude compared to others regions on the vane.

Figure 6.26 shows the computed wall shear on nozzle guide vanes for conditions identical to the experimental tests of [38] and [48]. The leading edge and much of the pressure surface experience low rates of wall shear, which also correspond to the peaks in deposition from the experimental tests. It is suggested that high shear forces in the trailing edge region of the pressure surface decrease the deposit accumulation rates.

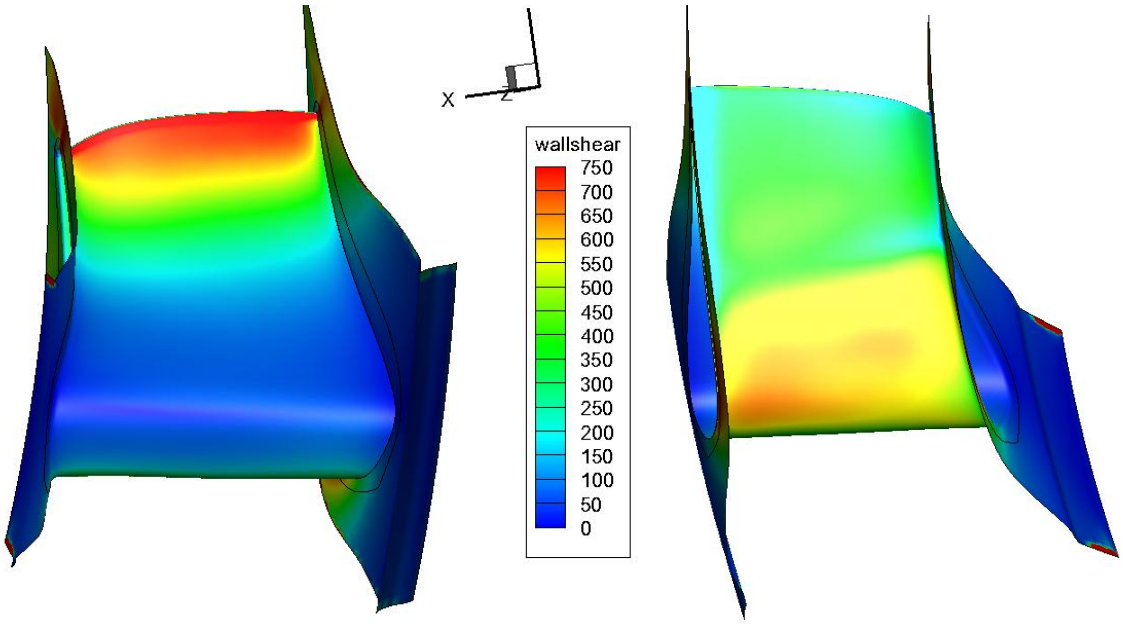

Figure 6.26 – Wall shear magnitudes (Pa) on nozzle guide vanes in TuRFR test using same conditions from [38][48] on (left) Pressure surface; (right) Suction surface.

It has long been observed in external deposition experiments [48]-[51] that no deposition forms on the suction side of the vanes. The justification for this came from the fact that computations predict that particles rarely impact the suction surface, preventing any deposit buildup. While this is true, the actual suction surface has always remained "clean," even more so than other locations that are predicted to experience little or no particle impacts. For the large St_k experimental tests from [48], it is expected that at least some deposit would form on the suction side as illustrated in Figure 6.27. These computations predict that some larger particles impact the suction surface after rebounding from the trailing edge of the adjacent vane. Additionally, some submicron size particles are expected to impact due to turbulent diffusion. Additionally, high shear on the suction surface likely prevents the occasional impacting particles from sticking.

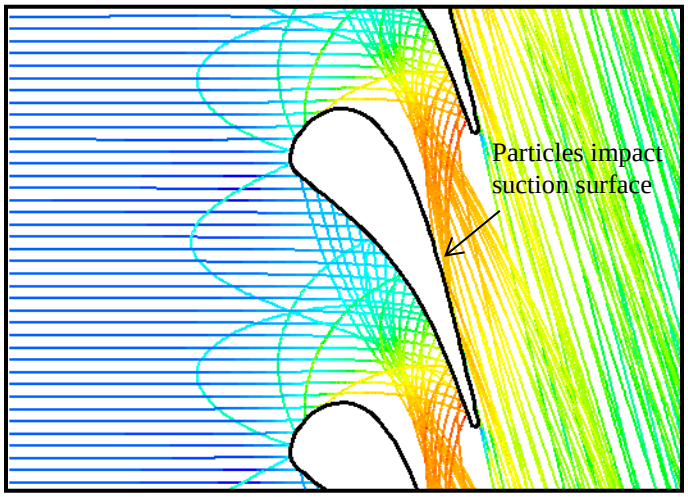

Figure 6.27 – Trajectories of 50 μm (Stk = 25) on 2D turbine vane.

Shear forces on external deposition may also influence growth after particle sticking. At high temperatures, deposit may be slightly viscous, and allowed to flow under high shear rates. This may also account for thin deposit structures at the vane trailing edge where deposit is over-predicted by computations. High flow rates cause the viscous deposit to flow to the trailing edge tip until breaking off.

6.10 Chapter Summary

Figure 6.28 illustrates the progression of the simulations discussed in this chapter, with major conclusions or contributions from each set of simulations. The progression of these simulations shows how shear plays a role in deposition in internal cooling cavities. The experiment and computation involving impinging jets with cross flow show that the increase in local wall shear correlates with a reduction in deposit growth. The two-dimensional, axisymmetric simulations show how initial growth is restricted to areas of low shear. Flow solutions with idealized deposit cones, patterned after the cones seen experimentally, show how regions of low shear change with the presence of growing deposit. Particle tracking also shows the insensitivity of the particle trajectories on deposit growth. This led to the formation of a simple sticking model based on the local wall shear at the location of particle impact.

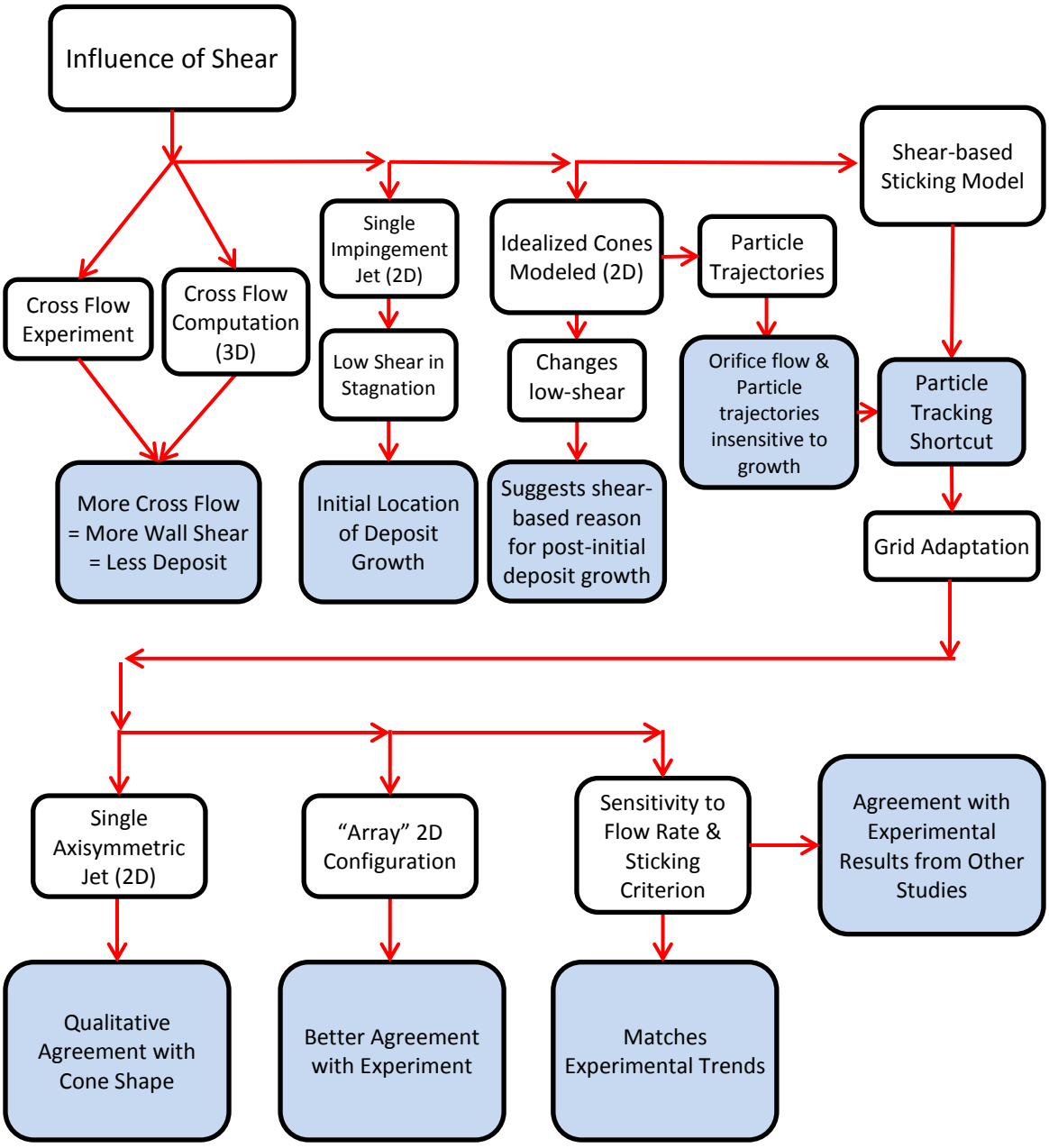

Figure 6.28 – Progression of computational simulations regarding investigations into the influence of shear with principle conclusions.

Applying the shear-based sticking model on a single impinging jet shows qualitative agreement with the experiments regarding deposit growth, even better than the 3D simulations with grid adaptation, and with reduced computational expense. However,

the single impingement jet lacked features present in an impingement jet array. The computational grid was modified to capture some important features of an array while maintaining an axisymmetric mesh. The deposit growth results better matched the experimental results with this modification. The operating conditions and sticking criterion were altered, showing agreement in trends with the experiments under different operating conditions.

Finally, the results from these simulations were compared to prior experiments in both internal and external deposition, and the influence of shear was discussed. These other experiments support the conclusion that increased wall shear results in a reduction of deposit buildup.

Chapter 7. Conclusions and Future Work

7.1 Conclusions

Several conclusions can be made from the experiments and computations in these studies about particle deposition in internal nozzle guide vane cooling cavities.

- Deposition is formed predominantly as individual mounds or cones on the internal vane wall associated with individual impingement jets. These represent locations of concentrated particle impacts.
- For low temperatures or high flow rates, deposit may also form as ridges between impingement holes, or as a combination of ridges and cones.
- Deposition on the internal vane wall is not limited to high fluid or wall temperatures, as deposition occurs even at ambient conditions and is only moderately dependent on temperature.
- Post-test particle analysis indicates that 1000 °F is not hot enough to cause sintering or melting of deposits, and that smaller particles have a higher propensity to deposit.
- A particle tracking method accurately predicted that a majority of particle impacts occur where deposit is seen to occur, on the vane cooling cavity wall downstream of impingement holes.

- Many sticking models were tested but remain inadequate for internal deposition applications, given that they generally fail to improve the deposition prediction beyond what is obtained from determining the location of particle impacts.
- Geometry adaptation, without accounting for shear, accounts for only a small part of the deviation between computations and experiments, widening the cone base by 50% but still not showing the same formations as the experiments. This also comes at an order of magnitude increase in computational expense.
- Experiments and computations show that deposits accumulate in regions of low shear. Computations suggest that shear plays a critical role in preventing deposit buildup as well as transporting particles to locations of low shear where they deposit.
- A shear-based sticking model was developed which was able to match the deposit growth structure of both of the cones and ridges, utilizing geometry adaptation on an axisymmetric grid with an outlet condition that artificially simulates the low shear region in an impingement jet array. These deposit formations are only predicted when both the shear-based sticking model and grid adaptation are utilized together.

7.2 Future Work

A principal conclusion for this work was the dominance of wall shear in particle sticking. It is recommended that this be further investigated by designing experiments or simulations to answer the following questions.

- External deposition modeling consistently under-predicts deposition on the trailing edge of turbine vanes, which are regions of high shear. Can experiments

be modified to isolate wall shear form other contributing factors to determine what effect wall shear has in external deposition.

- At what impingement flow rate or Reynolds number is deposit prevented from sticking?
- Prior studies suggest that chemical composition and surface material have a strong influence on particle deposition. What influence or interaction does this play in particle sticking at relatively low temperatures?
- The shear-based sticking model in this study assumed a sticking probability based on two extremes (τ_{max}, τ_{min}) and a linear function between. In reality, what would be a more realistic calibration curve for shear-based sticking, not only for various factors such as chemical composition, size, and temperature, but how the probability of sticking changes over a range of shear magnitudes for a given particle type? Can this be generalized theoretically based on properties of the particulate matter?

References

[1] Dunn, M.G., "Operation of Gas Turbine Engines in an Environment Contaminated with Volcanic Ash" *J. Turbomachinery,* Vol. 134, 051001 Sept. 2012

[2] Chambers, J. C., "The 1982 Encounter of British Airways 747 with the Mt. Galuggung Eruption Cloud," AIAA paper 85-0097, 1985

[3] Kim, J., Dunn, M.G., Baran, A.J., Wade, D.P., and Tremba, E.L., "Deposition of Volcanic Materials in the Hot Sections of Two Gas Turbine Engines," *J. Engr. Gas Turbines & Power,* Vol. 115, Jul 1993, pp 641-651.

[4] Hamed, A., Tabakoff, W., Wenglarz, R., "Erosion and Deposition in Turbomachinery" *J. Propulsion and Power,* Vol. 22, (2006).

[5] Bons, J.P. "A Review of Surface Roughness Effects in Gas Turbines" *J. Turbomachinery,* Vol. 132, 021004 (2010).

[6] Abuaf, N., Bunker, R.S., Lee, C.P., "Effects of Surface Roughness on Heat Transfer and Aerodynamic Performance of Turbine Airfoils," *J. Turbomachinery,* Vol. 120, July 1998, pp 522-529.

[7] Sundaram, N., Thole, K., "Effects of Surface Deposition, Hole Blockage, and Thermal Barrier Coating Spallation on Vane Endwall Film Cooling," *J. Turbomachinery.* Vol 129, July 2007, pp 599-607.

[8] Bons, J.P., Taylor, R.P., McClain, S.T., and Rivir, R.B., "The Many Faces of Turbine Surface Roughness," *J. Turbomachinery*. Vol. 123, 2001, pp 739-748

[9] Jensen, J.W., Squire, S.W., Bons, J.P., Fletcher, T.H., "Simulated Land-Based Turbine Deposits Generated in an Accelerated Deposition Facility," *J. Turbomachinery*. Vol. 127, July 2005, pp 462-470.

[10] Crosby, J.M., Lewis, S., Bons, J.P, Ai, W., Fletcher, T.H., "Effects of Temperature and Particle Size on high Pressure Turbine Deposition in Land Based Gas Turbines," *J. Engr. Gas Turbines & Power,* Vol. 130, Sept. 2008

[11] Laycock, R.G., Fletcher, T.H., "Time Dependent Deposition Characteristics of Fine Coal Fly Ash in a Laboratory Gas Turbine Environment" *J. Turbomachinery,* Vol. 135, 021003 (2013).

[12] Murphy, R., Nix, A., Lawson, S., Straub, D., Beer, S., "Preliminary Experimental Investigation of the Effects of Particulate Deposition on IGCC Turbine Film Cooling in a High-Pressure Combustion Facility" *Proceedings from 2012 ASME Turbo Expo,* Copenhagen, Denmark (2012)

[13] Murphy, R., Nix, A., Lawson, S., Straub, D., Beer, S., "Investigation of Factors that Contribute to Deposition Formation on Turbine Components in a High-Pressure Combustion Facility" *Proceedings from 2012 ASME Turbo Expo,* San Antonio, Texas (2013) GT2013-94657

[14] Smith, C., Barker, B., Clum, C., Bons, J.P. "Deposition in a Turbine Cascade with Combusting Flow." Presented at the ASME Turbo Expo 2010: Power for Land, Sea, and Air (2010) GT2010-22855

[15] Lawson, S.A., Thole, K., "The Effects of Simulated Particle Deposition on Film Cooling," *J. Turbomachinery,* Vol. 133, (2011)

[16] Lawson, S.A., Lynch S. P., Thole, K., "Simulations of Multi-Phase Particle Deposition on a Non-Axisymmetric Contoured Endwall With Film-Cooling," *J. Turbomachinery,* Vol. 135(3), 031032 (2013)

[17] Albert, J.E., and Bogard, D.G., "Experimental Simulation of Contaminant Deposition on a Film Cooled Turbine Vane Pressure Side With a Trench" *J. Turbomachinery,* Vol. 135(5), 051008 (2013)

[18] Wood E. J., "Simulated Syngas Ash Deposition on the Leading Edge of a Turbine Vane with Film Cooling" *Masters Thesis* Virginia Polytechnic Institute and State University (2010)

[19] Elghobashi, S., "On Predicting Particle-laden Turbulent Flows" *J. Applied Scientific Research*, (1994) Vol. 52 p 309-329

[20] Hossain, A., and Naser, J., "CFD Investigation of Particle Deposition around Bends In a Turbulent Flow." *15th Australasian Fluid Mechanics Conference* (2004).

[21] W. Tabakoff, A. Hamed, and M. Metwally. "Effect of Particle Size Distribution on Particle Dynamics and Blade Erosion in Axial Flow Turbines." *J. Engr. Gas Turbines & Power* (1991) Vol. 113, Issue 4, 607

[22] Brach, R. M., Dunn, P.F., and Li, X., "Experiments and Engineering Models of Microparticle Impact and Deposition" *J. Adhesion* (2000) Vol. 74, 227-282

[23] El-Batsh, H. and Haselbacher, H.,"Numerical Investigation of the Effect of Ash Particle Deposition on the Flow Field through Turbine Cascades," IGTI, Amsterdam, Netherlands, GT-2002-30600 (2002).

[24] Ai, Weiguo. "Deposition of Particulate from Coal-Derived Syngas on Gas Turbine Blades Near Film Cooling Holes." *Dissertation.* Brigham Young University, 2009.

[25] Tafti, Danesh K., and Sreedharan, S.S., "Composition Dependent Model for the Prediction of Syngas Ash Deposition with the Application to a Leading Edge Turbine Vane." *ASME Turbo Expo 2010: Power for Land, Sea, and Air* (2010).

[26] Senior, C.L., and Srinivasachar, S., "Viscosity of Ash Particles in Combustion Systems for Prediction of Particle Sticking." *Energy and Fuels* (1995).

[27] Wenglarz, R.A., "An Approach for Evaluation of Gas Turbine Deposition" *J. Eng. Gas Turbines and Power*, April 1992 Vol 114 pg 230

[28] El Batch "Modeling of Particle Deposition on Compressor and Turbine Blade Surfaces" *Dissertation*, Vienna University of Technology, 2001

[29] Mingione, G., Brandi, V., "Ice Accretion Prediction on Multielement Airfoils," *Journal of Aircraft*, Vol 35 (1998)

[30] Cao, Y., Zhang, Q., Sheridan, J., "Numerical simulation of rime ice accretions on an aerofoil using an Eulerian method," *The Aeronautical Journal*, 243-249 (2008)

[31] Son, C., Oh, S., Yee, K., "Quantitative analysis of a two-dimensional ice accretion on airfoils" Journal of Mechanical Science and Technology 26(4) (2012) 1059-1071

[32] Jung, S.K., Shin, S., Myong, R.S., Cho, T.H., "An efficient CFD-based method for aircraft icing simulation using a reduced order model" Journal of Mechanical Science and Technology 25(3) (2011) 703-711

[33] Gilat, A., Subramaniam, V., "Numerical Methods for Engineers and Scientists" John Wiley & Sons, 2008, pp. 323-328

[34] Zuckerman, N., Lior, N., "Impingement Heat Transfer: Physics, Correlations and Numerical Modeling" *Advances in Heat Transfer* Vol. 39 2006

[35] Lytle, D., Webb, B. W., "Air jet impingement heat transfer at low nozzle-plate spacings" *International Journal of Heat Transfer*, Vol 37, pp. 1687-1697 (1994)

[36] Cardwell, N.D., Thole, K., Burd, S.W., "Investigation of Sand Blocking Within Impingement and Film-Cooling Holes" *J. Turbomachinery*, Vol. 132 Apr. 2010

[37] Land, C.C., Joe, C., Thole, K., "Considerations of a Double-Wall Cooling Design to Reduce Sand Blockage" *J. Turbomachinery*, Vol. 132 Jul. 2010

[38] Barker, B., Casaday, B., Shankara, P., Ameri, A., Bons, J.P. "Coal Ash Deposition on Nozzle Guide Vanes: Part II – Computational Modleing," *J. Turbomachinery*, 135, 011015 (2013)

[39] Casaday, B., Ameri, A., Bons, J.P., "Numerical Investigation of Deposition on Nozzle Guide Vane Endwalls" *J. Engr. Gas Turbines & Power*, 135(3), 032001 (2013)

[40] Menter, F.R., "Two-Equation Eddy-Viscosity Turbulence Models for Engineering Applications" *AIAA Journal* 32(8):1598-1605 (1994)

[41] Martin, H., "Heat and mass transfer between impinging jets and solid surfaces" *Advanced Heat Transfer* Vol. 13, 1-60, (1977)

[42] Morsi, S. A., and Alexander, A. J., "An Investigation of Particle Trajectories in Two-Phase Flow Systems" J. Fluid Mech., 55(2):193-208, September 26 1972.

[43] H. Ounis, G. Ahmadi, and J.B. McLaughlin, "Brownian Diffusion of Submicrometer Particles in the Viscous Sublayer" Journal of Colloid and Interface Science, 143(1):266-277, 1991.

[44] Dehbi, A., "A CFD model for particle dispersion in turbulent boundary layer flows" *Nuclear Engineering and Design* Vol. 238 (2008) 707–715

[45] Saffman, P.G., "The lift on a small sphere in a slow shear flow" *J. Fluid Mechanics,* Vol. 22, 1965, pp. 385-400

[46] Ranz, W.E., and W. R. Marshall, W.R. Jr., "Evaporation from Drops, Part I" Chem. Eng. Prog., 48(3):141-146, March 1952.

[47] Whitaker, S., Reilly D., Bons, J.P., Crafton, J., "A Survey of Particle Impact Characteristics Using High Speed Particle Shadow Velocimetry" *Proceedings from AIAA Fluid Dynamics Conference,* San Diego, California, (2013)

[48] Webb, J., Casaday, B., Barker, B., Bons, J.P., Gledhill, A.D., Padture, N.P., "Coal Ash Deposition on Nozzle Guide Vanes: Part I – Experimental Characteristics of Four Coal Ash Types" *J. Turbomachinery,* 135, 021033 (2013)

[49] Bonilla, C., Webb, J., Clum, C., Casaday, B., Brewer, E., Bons, J.P., "The Effect of Film Cooling and Particle Size on Nozzle Guide Vane Deposition" *J. Engr. Gas Turbines & Power,* 134, 101901 (2012)

[50] Bonilla, C., Clum, C., Lawrence, M., Casaday, B., Bons, J.P., "The Effect of Film Cooling on Nozzle Guide Vane Deposition" *Proceedings from 2013 Turbo Expo,* San Antonio, Texas (2013) GT2013-95081

[51] Casaday, B., Prenter, R., Bonilla, C., Lawrence, M., Clum, C., Ameri, A., Bons, J.P., "Deposition with Hot Streaks in an Uncooled Turbine Vane Passage" *Proceedings from 2013 Turbo Expo,* San Antonio, Texas (2013) GT2013-95018

[52] Abd-Elhady, M.S., Rindt, C.C.M., Wijers, J.G., van Steenhove, A.A., "Particulate fouling in waste incinerators as influenced by the critical sticking velocity and layer porosity" *Energy*, 30 (2005) 1469-1479

[53] Clum, Carey, "The Effects of Particle Size, Chemical Composition, and Temperature on Deposition in an Impingement Cooling Scheme" *Thesis,* The Ohio State University, 2013

[54] Rao, N.P., Navascues, J., Fernandez de la Mora, J., "Aerodynamic focusing of particles in viscous jets" *Journal of Aerosol Science,* Vol. 24 (1993) 879-892

[55] Casaday, B., Ameri, A., Bons, J.P., "Effect of Hot Streaks on Ash Deposition in an Uncooled Turbine Vane Passage" *Proceedings from Aerospace Sciences Meeting* Nashville, Tennessee (2012)

[56] Webb, Josh, "The Effect of Particle Size and Film Cooling on Nozzle Guide Vane Deposition" *Thesis*, The Ohio State University, 2011

Appendix A: Computational Simulation Conditions

All flow solutions were acquired using Fluent software v.12.0. In all cases, a pressure-based solver was applied and steady-state solutions acquired.

3D Simulations (Chapter 5)

Turbulence model: kω-SST with compressibility effects and viscous heating

Turbulence model constants:

$$\alpha_{\infty}^{*} = 1, \alpha_{\infty} = 0.52, \alpha_{o} = 0.11111, \beta_{\infty}^{*} = 0.09, R_{\beta} = 8, R_{k} = 6, R_{\omega} = 2.95,$$

$$\zeta^{*} = 1.5, M_{t0} = 0.25, a_{1} = 0.31, \beta_{i(in)} = 0.075, B_{i(out)} = 0.0828, \sigma_{k(in)} = 1.176,$$

$$\sigma_{k(out)} = 1.0, \sigma_{\omega(in)} = 2.0, \sigma_{\omega(out)} = 1.168, \text{Wall Pr} = 0.85$$

Boundary Conditions

- Inlet: Constant velocity = 4.155 m/s (calculated to match flow rate)
    - Turbulence intensity = 10%
    - Hydraulic diameter = 0.02 m
    - Temperature = 811°K
- Outlet: Gauge pressure = 0 Pa (Operating Pressure = 1 atm)
    - Backflow direction specification = “From neighboring cell”
    - Turbulence intensity = 10%
    - Hydraulic diameter = 0.003 m
    - Backflow temperature = 811°K
- Backside of impact plate temperature condition = Convection

- Heat transfer coefficient = 1000
- Free Stream temperature = 1089°K

- Wall thermal conditions
  - Conjugate for internal walls (interface with fluid)
  - Adiabatic for all other walls

Material conditions

- Air:
  - Density: ideal gas
  - Specific heat: polynomial fit

$$C_P[\text{J/kg°K}] = 870.82 + 0.3.52 \times T[\text{°K}] - 8.213 \times 10^{-5} \times T^2$$

  - Thermal conductivity: polynomial fit

$$k_f[\text{W/m°K}] = 0.011866 + 6.4491 \times 10^{-5} \times T - 8.9471 \times 10^{-9} \times T^2$$

  - Viscosity: Sutherland Law

$$\text{Reference Viscosity} = 1.716 \times 10^{-5}, \text{Reference Temperature} = 273.11, \text{Effective Temperature} = 110.56$$

  - Molecular Weight = 28.966
- Particulate matter
  - Density = 2650 kg/m^3
  - Specific heat = 984 J/kg°K
  - Thermal conductivity = 0.5 W/m°K
  - Thermophoretic coefficient: Talbot-diffusion coefficient
- Stainless steel
  - Density = 8000 kg/m^3

    - Specific heat = 500 J/kg°K
    - Thermal conductivity = 21.5 $W/m°K$
- Inconel
    - Density = 8400 kg/m^3
    - Specific heat = 536 J/kg°K
    - Thermal conductivity = 17.5 $W/m°K$
- Particulate Deposit
    - Density = 1325 kg/m^3
    - Specific heat = 984 J/kg°K
    - Thermal conductivity = 0.25 $W/m°K$

Solution Methods: SIMPLE scheme

- Spatial Discretization
    - Gradient: Least Squares Cell Based
    - Pressure: Second Order
    - Density: Second Order Upwind
    - Momentum: Second Order Upwind
    - Turbulent Kinetic Energy: First Order Upwind
    - Specific Dissipation Rate: First Order Upwind
    - Energy: Second Order Upwind

Discreet Phase Options

- Maximum number of steps = 50,000
- Length scale = 0.0001
- Other numeric use default

Cross Flow Simulations (Section 6.1)

Same as prior 3D simulations with exception of

Boundary Conditions

- Inlet: Pressure Inlet- Gauge Pressure = 2500 Pa
    - Turbulence intensity = 10%
    - Hydraulic diameter = 0.02 m
- Outlet: Outlet pressure adjusted to target flow rate of 0.000236 kg/s
    - Backflow direction specification = “From neighboring cell”
    - Turbulence intensity = 10%
    - Hydraulic diameter = 0.003 m

Material conditions

- Air:
    - Density = 1.225 kg/m^3
    - Viscosity = 1.7894×10^{-5} kg/m-s

No solid material modeled

Energy equation not applied

2D Simulations of single impingement jet (Section 6.2-6.5)

Turbulence model: kω-SST without compressibility effects and viscous heating

Boundary Conditions

- Inlet: Pressure Inlet- Gauge pressure = 2500 Pa
    - Turbulence intensity = 10%

    - Hydraulic diameter = 0.02 m
- Outlet: Gauge pressure = 0 Pa (Operating Pressure = 1 atm)
    - Backflow direction specification = “From neighboring cell”
    - Turbulence intensity = 10%
    - Hydraulic diameter = 0.003 m

Material conditions

- Air:
    - Density = 1.225 kg/m^3
    - Viscosity = 1.7894×10^{-5} kg/m-s

No solid material modeled

Energy equation not applied

Solution Methods: SIMPLE scheme

- Spatial Discretization
    - Gradient: Least Squares Cell Based
    - Pressure: Second Order
    - Momentum: Second Order Upwind

<u>2D Simulations of single impingement jet (Section 6.6-6.8)</u>

Turbulence model: kω-SST without compressibility effects and viscous heating

Boundary Conditions

- Inlet: Pressure Inlet- Gauge pressure = 2500 Pa
    - Turbulence intensity = 10%
    - Hydraulic diameter = 0.02 m

    - For high flow rate: Inlet gauge pressure = 5625 Pa
    - For low flow rate: Inlet gauge pressure = 1250 Pa
- Outlet: Gauge pressure = 0 Pa (Operating Pressure = 1 atm)
    - Backflow direction specification = “From neighboring cell”
    - Turbulence intensity = 10%
    - Hydraulic diameter = 0.003 m

Material conditions

- Air:
    - Density = 1.225 kg/m^3
    - Viscosity = 1.7894×10^{-5} kg/m-s

No solid material modeled

Energy equation not applied

Solution Methods: SIMPLE scheme

- Spatial Discretization
    - Gradient: Least Squares Cell Based
    - Pressure: Second Order
    - Momentum: Second Order Upwind